DOCTOR OF PHILOSOPHY

Compact Femtosecond Lasers for Multiphoton Imaging

Mirkhanov, Shamil

Award date:
2018

THE UNIVERSITY OF DUNDEE

SCHOOL OF ELECTRONIC ENGINEERING, PHYSICS AND MATHEMATICS

Compact Femtosecond Lasers for Multiphoton Imaging

by

Shamil Mirkhanov

Thesis for the degree of Doctor of Philosophy

University of Dundee

March 2018

THE UNIVERSITY OF DUNDEE

School of Electronic Engineering, Physics and Mathematics

Doctor of Philosophy

Abstract

Compact Femtosecond Lasers for Multiphoton Imaging

by Shamil Mirkhanov

Multiphoton imaging currently is one of the main development directions in Laser Scanning Microscopy. A simplified way to assess suitability of a given laser for MPI applications is a figure of merit (FOM) approach based on peak power and average power of the particular excitation laser used. The first systematic studies of FOM for two-photon imaging within 336fs – 3.5 ps pulse duration range and repetition rate from 2.85 MHz to 90 MHz at 1 micron using a Yb fiber laser have been done in the first part of this thesis.

Vertical External Cavity Surface Emitting Lasers (VECSELs), also called Semiconductor Disc Lasers (SDL) are nowadays capable of producing sub-100-fs pulses, multi-kW peak powers, and mode-locking has been demonstrated for wavelength range from 675nm to >2 microns. These flexible, low cost lasers have the potential to allow multi-source multiphoton microscopy system design. One of the most challenging aspects of VECSELs is the deposition of heat into the active region, leading to strong temperature – dependent performance. In contrast, recently introduced Distributed Bragg Reflector (DBR) free technology helps to address these challenges. The second part of this thesis describes the development of 1μm DBR free VECSEL - Membrane External Cavity Surface Emitting Laser (MECSEL), that demonstrated the record CW output power for these lasers reported so far.

Finally, a new concept of DBR-free semiconductor saturable absorber based on the membrane technology was suggested. For the first time a membrane saturable absorber structure grown using MOVPE and processed via lateral etching is realized. This membrane saturable absorber was used to mode-lock a 1μm VECSEL for the first time.

Acknowledgements

I would like to thank all those people who provided me support, help, advise and contributed in many ways to this work.

I would like to especially thank my supervisor Dr. Keith G. Wilcox, for his constant support, insightful guidance, constant help, kindness, open-minded approach, sharing his passion to Science, and hard work in the proof-reading of this work and all the others as well. I learned from you a lot. I would like to thank my second supervisor, Dr. Samuel Swift, for his help throughout the project, useful advises, jokes, motivation and optimism. I would like to thank Dr. Adrian H. Quarterman for the great amount of his help, useful discussions and curiosity and Conor J. C. P. Smyth for great time, jokes and discussions. I would like to generally thank all the members of VECSEL group at IHFG, University of Stuttgart, including, but not limited to: Professor Peter Michler, Dr. Michael Jetter, Roman Bek, Dr. Hermann Kahle, Raffael Peccoroni. Without their help, guidance and support, work done on IR MECSEL will not be possible. I am generally grateful to Marie Curie ITN PHOQUS for giving me a great opportunity to do research and enjoy it. I would like also to sincerely thank all of my teachers at Lyceum №180 «Poliforum» of Ekaterinburg, and at Kazan Federal University for providing me with a good basis for PhD studies.

I would like to acknowledge all the University of Dundee support and technical staff, without whom this work will be much harder to do, if possible at all. Thanks to all the electrical and mechanical workshop staff. Many thanks to all the other members of the University of Dundee and University of Stuttgart for support and help.

Finally, I am very grateful to all my family and friends in Ekaterinburg, Kazan and Dundee for their love and support.

Declaration of Authorship

I, Shamil N. Mirkhanov, hereby declare that this thesis entitled *Compact Femtosecond Lasers for Multiphoton Imaging* as well as the work presented are both written and done by me and has not been submitted any time before in any application for higher degree. I was admitted as a candidate for the degree of Doctor of Philosophy and as a Marie Curie ESR in August 2014. The higher study for which this is a record was carried out at the University of Dundee between 2014 and 2017. I declare and confirm that:

- This work was done mainly while in candidature for a research degree at The University of Dundee.
- If any part of this thesis has been previously submitted for any other qualification at The University of Dundee or any other institution, this has been stated clearly.
- Where I have consulted the published work of others, this has been clearly stated
- Where I have quoted from the others work, source is always provided
- All main sources of help have been acknowledged
- Where the thesis is based on work done by myself jointly with the others, work done by me and by the others clearly described
- Parts of this work have been published as in my list of publications.

Date 18.05.2018

Signature [redacted]

I hereby certify that the candidate has fulfilled the conditions of the Resolution and Regulations appropriate for the degree of Doctor of Philosophy at the University of Dundee and also that the candidate is qualified to submit this thesis in application for that degree.

Date 18.05.2018

Signature of supervisor [redacted]

List of Figures

Abbreviations

FOM – Figure of Merit

VECSEL - Vertical External Cavity Surface Emitting Laser

SDL – Semiconductor Disc Laser

DBR - Distributed Bragg Reflector

MECSEL - Membrane External Cavity Surface Emitting Laser

IR MECSEL – Infrared Membrane External Cavity Surface Emitting Laser

SESAM - Semiconductor Saturable Absorber Mirror

SESAME - Semiconductor Saturable Absorber Membrane

MOVPE – Metalorganic Vapour Phase Epitaxy

MPI – Multi Photon Imaging

BRF - Birefringent Filter

MIXSEL – Mode-locked Integrated External-Cavity Surface-Emitting Laser

CW – Continuous Wave

NA – Numerical Apperture

FLIM - Fluorescence Lifetime Imaging

QW- Quantum Well

QD – Quantum Dot

LCF - Longitudinal Confinement Factor

GDD – Group Delay Dispersion

PL - Photoluminescence

CPM - Colliding Pulse Mode-locking

KLM – Kerr Lens Mode-lockimg

TCE – Trichloroethylene

Contents

To Daria Belous

1. Introduction

1.1 Introduction

Multiphoton imaging [1] currently is a main development direction in advanced Microscopy. It provides an efficient method to study both fixed tissue and in-vivo samples, allowing deep tissue imaging with great selectivity, imaging only the sample area located at the focal plane. It helps to address problems arising in conventional confocal imaging, since due to the nature of multiphoton signal, photodamage and photobleaching can be avoided more efficiently [2]. MPI uses pulsed laser sources with pulse durations ranging from a few picoseconds to tens of femtoseconds at a wavelength range from visible to mid-infrared. Therefore, it is useful to have a simple way to estimate a validity of a given laser for MPI applications. Theoretical treatments of two photon imaging have shown that the key laser parameter for two photon signal is the product of peak power and average power [3]. The parameters of individual laser sources for MPI have been extensively discussed in literature before, for example in [4-6], and a simplified way to assess suitability of a given laser for MPI applications was suggested by introducing the figure of merit (FOM) approach based on peak power and average power of the particular excitation laser used. However, so far there was no systematic study of the validity of the FOM over a large parameter space of repetition rate and pulse duration. The first systematic studies of FOM over the large parameter space for two-photon imaging at 1 micron using Yb fiber laser have been done in the chapter 2 of this thesis.

Vertical External Cavity Surface Emitting Lasers (VECSELs), also called Semiconductor Disc Lasers (SDL) [7] are nowadays capable of producing sub-100-fs pulses [8], multi-kW peak powers [9], and mode-locking has been demonstrated for wavelength range from 675nm to >2 microns [10]. These flexible, low cost lasers have the potential to allow multi-source multiphoton microscopy system design, similar to those in confocal microscopy, where imaging systems typically employ several different laser sources to reach a set of required wavelengths.

The temperature sensitivity of the semiconductor gain material, which strongly affects laser performance, leads to thermal management being an important element in high power VECSELs [11]. The recently introduced Distributed Bragg Reflector (DBR) free technology is one approach which could address this challenge [12]. Chapter 3 of this thesis introduces VECSELs and describes the development of 1μm DBR free

VECSEL - Membrane External Cavity Surface Emitting Laser (MECSEL) that demonstrated the record CW output power for these lasers reported so far. Chapter 4 starts with introducing Semiconductor Saturable Absorber Mirrors (SESAM). There, a new concept of membrane Semiconductor Saturable Absorber Membrane (SESAME) was suggested. For the first time a SESAME structure grown using MOVPE and processed via lateral etching was successfully realized. This was led to mode-locking of a 1µm VECSEL gain sample using SESAME for the first time.

This thesis concludes with chapter 5, where all obtained results are summarized and future work related to MECSEL and SESAME is suggested.

1.2 Multiphoton imaging: state of the art

Multiphoton imaging (MPI) is a powerful fluorescence laser scanning microscopy technique allowing high resolution deep tissue imaging due to the 3-D localization of the fluorophore excitation through a two (or more) photon process. Since a longer wavelength in contrast to one photon excitation is used it results in less scattering in tissue and less photodamage. MPI is a type of laser-scanning microscopy that employs localized nonlinear excitation, where fluorescence is excited only within scanned focal volume. The theoretical possibility for multi-photon molecular excitation occurring within a single quantum event was first suggested by Maria Göppert-Mayer in 1930 [13] in her PhD thesis, but experimentally two-photon excitation has been demonstrated in 1961 [14], when lasers became available. After almost 30 years, multiphoton imaging using mode-locked femtosecond laser and high numerical aperture objective experimentally realized.

From the time when multiphoton microscopy technique was introduced, it started to attract significant attention due to its capability of tissue imaging [15, 16] and cell imaging [17, 18], also allowing deep tissue imaging [19, 20] with significantly less photodamage caused [21], in compare to single-photon confocal microscopy [22]. Over the last 15 years MPI has been intensively and successfully employed for a wide range of life sciences-related applications including neuroscience [23], in-vivo imaging [24] with record imaging depth of 1.6 mm attained in vivo in the mouse brain cortical tissue [25], single molecule detection in solution [26] and multiphoton imaging of unstained samples using excitation of intrinsically fluorescent molecules within the specimens of interest [27]. Multiphoton excitation has been successfully combined with other imaging and analysis techniques – for example, with UV - mediated Focal Uncaging [28], Second Harmonic Generation (SHG) [29, 30], Fluorescence Lifetime Imaging (FLIM) [31, 32], Coherent anti-Stokes Raman spectroscopy (CARS) [33, 34] and 4π confocal fluorescence microscopy [35].

While multiphoton imaging has mostly been used for biological and medical - related applications this microscopy technique also shown potential in fields like molecular photodynamics [36] and optical data storage [37, 38].

The progress in the field of MPI is driven on the one hand by advancing MPI setups [39], together with increased availability of suitable pulsed excitation lasers covering a broad range of wavelength, and on another hand by synthesis of novel fluorophores

suitable for multiphoton excitation. Since one-photon and two-photon excitation have different quantum mechanical selection rules, dyes that are an optimal choice for one photon excitation might be not for two photon excitation.

The development and synthesis of new fluorophores with optimal two photon absorption properties has played an important role in reduction of the required laser excitation intensity and therefore reduction of photodamage caused to a specimen during imaging [40]. The two photon absorption process has a cross section of $\sim 10^{-50}$ cm^4 s = 1 GM (Göppert-Mayer), therefore to generate absorption efficiently the sample should be exposed by a high density photon flux, that could be generated by ultrafast lasers. However, two-photon fluorescence microscopy using continuous wave excitation from the 647 nm Ar:Kr laser has also been demonstrated [41].

The Ti:Sapphire laser, with typically 80 MHz repetition rate and <150 fs pulse duration is the dominant workhorse laser of the MPI market despite its high cost, largely due to its proven track record and the large wavelength range that it can offer.

However, other pulsed laser types such as for example Yb fiber laser, Er fiber laser [42], and gain-switched laser diode [43] have also been employed for multiphoton imaging. The increased availability of relatively low cost femtosecond fiber lasers around 780-790 nm and 1030-1080 nm provides a realistic alternative for light sources for multi-photon imaging (MPI) [44]. One typical feature of femtosecond fiber lasers is the chirped pulse master oscillator power amplifier approach often employed. This makes varying the repetition rate straightforward, thanks to the integration of a low power fiber-coupled pulse picker between the master oscillator and power amplifier. Additionally, as a pulse compressor is typically needed after the power amplifier, it is possible to make the laser have variable pulse duration if the chirped nature of the longer pulses can be tolerated. Other laser types, such as the semiconductor disk laser (SDL) also offer promise as low cost lasers for multi-photon imaging [45, 46].

1.3 VECSELs: state of the art

Vertical external cavity surface-emitting lasers (VECSELs) also called Semiconductor disc lasers (SDLs) are first realized in their current form in 1997 while the concept of optically-pumped semiconductor laser with radiating mirror could be backdated to 1966 [47].

VECSELs have attracted significant attention over the last ~20 years due to the fact that they provide high output power levels while preserving good beam quality with M^2~1 [48] and, due to semiconductor design flexibility, could be fabricated for a wide wavelength interval, currently covering a range from ~393 nm [49] to ~ 5000 nm [50]. To cover such a broad wavelength range, many semiconductor material systems combinations have been used, such as for example InGaN for ~400 nm [51, 52], InGaP/AlGaInP and InP/AlGaInP for 640-750 nm [53-57], GaAs/AlGaAs for 850-870 nm [58-60], InGaAs/GaAs for 900 – 1180 nm [61-63], GaInNAs/GaAs for 1160-1320 nm [64-67], InGaAsP for 1550 nm [68, 69], GaInAsSb/AlGaAsSb for 2000-2800 nm [70-74] and PbTe for ~5000 nm [75].

Semiconductor device fabrication processes used for VECSEL production allow a large number of lasers to be produced from just one grown wafer. VECSELs have been successfully commercialized by *Coherent Inc.,* and *M Squared lasers*. The semiconductor gain structure of VECSELs can be fabricated according to the requirements of the resulting laser applications with actual layer structure designed to provide high average output power [76-80], with current continuous-wave output power record from VECSEL exceeding 100 W [81], or for ultrashort pulses generation [82-85]. The VECSEL structure could also be designed and optimized using a microscopic modeling approach [86, 87]. While most commonly VECSELs use quantum well-based gain media, quantum dot based VECSELs have also been developed [88-90] since quantum dots allow longer wavelength emission by employing lower bandgap alloys with higher lattice mismatch.

The VECSEL external cavity geometry allows the introduction of additional optical components into a cavity such as birefringent filter (BRF) for wavelength tuning [91], second harmonic generation crystals [92], or semiconductor saturable absorber mirrors (SESAM) for mode-locking [93, 94]. Active mode-locking of VECSEL using low-loss vertical cavity modulator was demonstrated [95]. However, active mode-locking becomes ineffective for very short pulses, and limits the attainable pulse width. The first

passively mode-locked VECSEL was demonstrated in 2000 [96]. Also, the shortest pulses reached by VECSELs so far were obtained using passive mode-locking with SESAM. VECSELs now are capable of producing sub-100-fs pulses, multi-kW peak powers, and mode-locking has been demonstrated across a wavelength range from 675nm to >2 microns. Mode-locking in VECSELs was demonstrated also for example using quantum dot based SESAM [97], single-walled carbon nanotube saturable absorber [98] and single-layer graphene saturable absorber [99]. Recently, colliding pulse mode-locking with VECSELs [*100*] has been demonstrated providing output power of 2.2W, with repetition rate of 1GHz and pulse duration of 1.16ps. Also, SESAM free mode-locking in VECSELs has been reported [101, 102]. While the saturable absorber in mode-locked VECSELs is usually a separate intra-cavity element, an approach based on monolithic integration of saturable absorber and the gain medium in a single structure was developed [103] and called the mode-locked integrated external-cavity surface-emitting laser (MIXSEL). MIXSELs have reached 6.4 W [104] of output power with 28-ps pulses at 2.5-GHz repetition rate, and a 10 GHz repetition rate MIXSEL providing 2.4 W of average power and 17 ps of pulse duration has been demonstrated [105]. The first femtosecond MEXSEL providing 620 fs pulses at 4.8 GHz and average power of 101 mW has been reported by [106]. For MIXSEL, the repetition rate tune-ability in a range 5-100 GHz has been demonstrated [107]. Recently, a dual-comb MIXSEL was applied for dual-comb spectroscopy of water vapor [108].

Due to high temperature sensitivity of semiconductor gain medium and poor thermal conductivity of the relatively thick substrate and DBR layers, VECSELs require effective thermal management. There are two general approaches to thermal management in VECSEL: the first approach based on using intra-cavity crystalline heat-spreaders [109, 110], and the second includes substrate removal [111], which allows the resulting thin gain chip to be soldered to a heatspreader.

The DBR-free VECSEL has been reported [112, 113] with the concept theoretically studied in [114]. Broad-wavelength tuning using this laser was also demonstrated. Using the possible approaches for thermal management of such suggested DBR-free VECSELs, the semiconductor membrane external-cavity surface-emitting laser (MECSEL) consisting of a diamond heat spreader sandwiched AlGaInP-based active region design without a monolithically integrated DBR was successfully realized recently. Studies done in this thesis describe the development of 1μm DBR-free VECSEL have led to a record 10.1 W of CW output power using a SiC heatspreader.

This thesis also introduces semiconductor saturable absorber membrane (SESAME) technology with the first realized SESAME and describes experiments demonstrating first mode-locking results of a 1μm VECSEL gain sample using this SESAME.

All the above described advantages of VECSELs resulted at many applications of these lasers demonstrated so far – VECSELs to date being used, for example, in THz generation and imaging [115], multiple components hydrocarbon gas sensing [116], supercontinuum generation [117], as a pump source for other lasers such as Cr^{2+}: ZnSe [118]. VECSEL gain samples have been also designed for solar pumping [119]. Another field, where VECSELs could be used, is Laser Scanning Microscopy, and in particular multiphoton imaging where these high-flexibility low cost lasers have the potential to enable multi-source multiphoton microscopy system architectures equivalent to those used in confocal microscopy, where microscopes are often supplied with a number of sources at different wavelengths depending on which fluorophores the user wishes to study.

1.4 VECSELs as alternative lasers for MPI

Multiphoton imaging is a commonly used microscopy method in the biological sciences. MPI technology largerly depends on availability of ultrafast laser sources covering broad wavelength range. With the increased commercial availability of highly flexible alternatives to traditional Ti:Sapphire lasers it is important to understand the optimum laser parameters for multiphoton imaging.

Theoretical treatments of two photon imaging have shown that the key laser parameter for two photon signal is the product of peak power and average power. This has been simplified into a figure of merit or FOM, which presents the product of peak and average power as a simple parameter, removing dependencies such as fluorophore lifetime and local biological environment. To date, the widely-used FOM approach has not been validated and systematically tested over a large parameter space.

VECSELs offer promise as low cost lasers for multi-photon imaging and the potential of these lasers for MPI is already being examined and demonstrated by several groups. However, one of the central problems limiting VECSEL performance is thermal management which limits average power. Recently introduced DBR-free VECSEL technology allows better thermal management of the gain medium, also high slope efficiency has been demonstrated alongside with 80 nm wavelength tuning and 6 W of CW output power [112]. In addition, the same membrane concept could be adopted for SESAM to produce SESAME with improved thermal stability. An additional advantage of the absence of a DBR within the VECSEL is that there are no limitations related to necessity of lattice matching the DBR to the substrate, or DBR to active region, therefore there is additional potential for the growth of structures with the new designs. Therefore, these flexible, low cost DBR-free VECSEL technology have the potential to allow multi-source multiphoton microscopy system design similar to those in confocal microscopy, where imaging systems employ several different laser sources to reach a set of required wavelengths. For example, a set of three mode-locked DBR-free VECSELs covering wavelength of 800 nm, 1000 nm and 1200 nm respectively, embedded in a single laser box would allow multiphoton excitation of a wide range of fluorophores commonly used for MPI of living and fixed tissue samples.

All the above mentioned features combined with wavelength versatility make DBR-free mode-locked VECSELs favorable candidates for MPI applications.

2. Studies of MPI over large parameters space

2.1 Introduction and background

Multiphoton imaging nowadays provides efficient and powerful fluorescence microscopy tool that helps to address many arising challenges in Life Sciences applications. Multiphoton imaging has many advantages over conventional confocal technique including greater penetration depth in fixed tissues and cells, less photodamage and photobleaching.

Progress in this field is, to date, driven by high quality optical systems for imaging as well as availability of efficient fluorophores for wide wavelength range on one hand, and dedicated pulsed laser sources covering large spectral area on the other hand. MPI usually employs Ti:Sapphire lasers as excitation sources, with a repetition rate of 80 MHz, <150 fs pulse duration and with a tunable near infrared wavelength. However, these lasers are expensive and bulky and the increased availability of relatively low cost femtosecond fiber lasers around 780-790 nm and 1030-1080 nm provides alternative excitation sources for multi-photon imaging. A set of fixed-wavelength mode-locked VECSELs can potentially be as beneficial for MPI as CW VECSELs for confocal microscopy.

Understanding the impact of laser source parameters on multiphoton image quality is crucial for optimizing these flexible types of laser for multiphoton imaging. Theoretical treatments of two photon imaging have shown that the key laser parameter for two photon signal is the product of peak power and average power. As described before, this has been simplified into a figure of merit (FOM), which presents the product of peak and average power as a simple parameter, removing dependencies such as fluorophore lifetime and local biological environment. To date, the widely-used FOM approach has not been systematically validated and tested over a large parameter space. This chapter of the thesis will introduce basics of MPI, alongside with typical laser sources and fluorophores for MPI, describe general setup used for MPI and conclude with the first systematic studies of FOM over the large parameters space for two-photon imaging around at 1 micron using Yb fiber laser.

2.1.1 Basics of MPI

The theoretical possibility for multi-photon molecular excitation occurring within a single quantum event was first suggested by Maria Goppert-Mayer in 1930 in her PhD thesis, but experimentally two-photon excitation has been demonstrated only in 1961, when lasers became available. In the case of one-photon excitation (Figure 1 a), ultraviolet or visible light excites a molecule from its ground state. When the energy of the absorbed photon is equal to the energy gap between ground state and excited state, transition to higher energy level (higher energy molecular orbital) occurs. On the other hand, two photon excitation (Figure 1 b) is based on the almost simultaneous (~10^{-16} s) absorption of two photons with less energy. Each photon in case of two-photon excitation has about half the energy necessary to excite the molecule in the one-photon process. The transition to the excited state in the two-photon case occurred via an intermediate virtual state. The molecule absorbs one photon and just before transition back to ground state occurs, it absorbs another photon elevating the molecule to the excited state. Molecules that undergo one photon excitation and two photon excitation are following identical decay processes, and therefore emit the identical fluorescence signal.

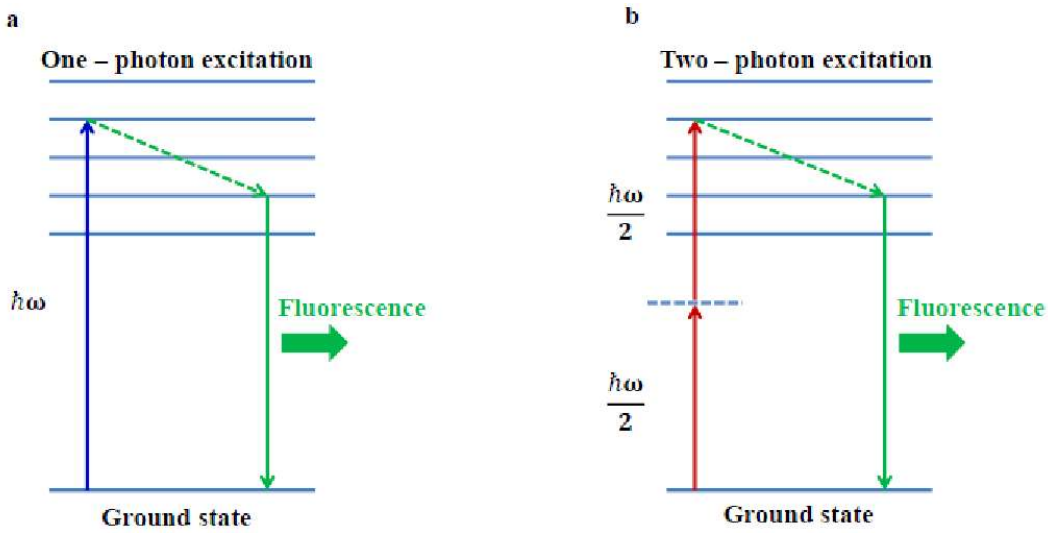

Fig. 1. Jablonski diagram for one photon excitation process (a) compared to two-photon excitation process (b).

The probability of two-photon excitation process is much less than the probability of one-photon excitation, therefore two-photon excitation occurs generally in regions with high spatial and temporal photon concentration that could be achieved using objectives

with high numerical aperture (NA) and by employing pulsed laser sources providing high peak power levels.

One general advantage of using two-photon excitation for microscopy applications is that in the one photon case (Figure 2 a), out-of focal plane excitation is quite high, whereas in two-photon case most of fluorescence signal comes from very thin (~1μm) region (Figure 2 b).

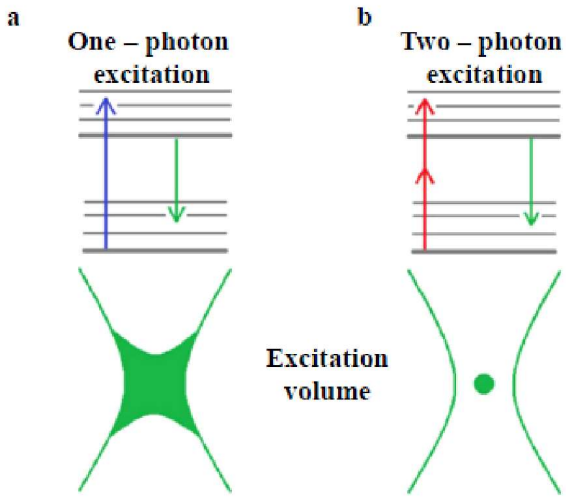

Fig. 2. Excitation volume profile shown for one-photon excitation (a) and two-photon excitation (b).

The two photon absorption process has a cross section of $\sigma_2 \sim 10^{-50}$ cm^4 s photon^{-1} = 1 GM (Göppert-Mayer), with two photon absorption rate W_2 given by:

$$W_2 = \frac{1}{2}\sigma_2 I^2 , \qquad (1)$$

Where I denotes the light intensity. The fluorescence quantum yield, Φ_{2pe} , in the case of two photon excitation can be expressed as:

$$\Phi_{2pe} = \frac{N_e}{N_a} , \qquad (2)$$

Here, N_e and N_a denote the number of emitted fluorescence photons and the number of absorbed photon pairs, respectively. Given that, the two-photon fluorescence cross-section σ_{2pf} could be written as:

$$\sigma_{2pf} = \Phi_{2pe}\sigma_2 \qquad (3)$$

The possibility for localized excitation in the two-photon case allows effective deep tissue imaging and sectioning, and also results in better contrast and less photobleaching. The natural sectioning possibility provided by two photon excitation was successfully combined with laser scanning microscopy, and multiphoton imaging using mode-locked femtosecond laser and high numerical aperture objective has been experimentally realized. The longer wavelength excitation length used for multiphoton imaging undergoes less scattering in biological tissues, resulting at additional advantage of MPI for biomedical applications. The development and synthesis of new fluorophores with optimal two photon absorption properties plays an important role in reduction of required laser excitation intensity and therefore reduction of photodamage caused to specimen during imaging. Some fluorophores could undergo two-photon excitation by irradiating them with doubled wavelength of their absorption maximum. However, taking into account that one photon absorption and two photon absorption have different quantum mechanical selection rules, two-photon excitation spectrum scaled using this method not guaranteed to be an equivalent to its one photon excitation spectrum.

Multiphoton imaging is based on high-order optical processes, and the probability of exciting two-photon transition is very low in comparison to one photon excitation. Therefore, to allow efficient two photon excitation it is critical to illuminate the sample with photons that have high temporal and spatial density. High spatial photon density in multiphoton imaging is achieved by high NA objective lenses, while ultrafast lasers are used to obtain high temporal photon density. In the first report on two-photon laser scanning fluorescence microscopy, authors used a femtosecond colliding pulse modelocked dye laser. However, at the moment most popular laser used in multiphoton imaging is Ti:Sapphire laser that can generally provide pulses in the range of 80–200 fs at a repetition rate in a range 50-100 MHz. An alternative excitation source to dye and Ti:Sapphire laser could be the Cr:Forsterite laser [120], however in this case wavelength range is limited to 1150-1300 nm. Many other pulsed laser sources such as for example Yb fiber laser, Er fiber laser, and gain-switched laser diode were also employed for multiphoton imaging. The MPI microscope systems are generally very expensive, and they are also normally equipped with expensive and bulky excitation lasers, such Ti: Sapphire lasers that in addition require professional maintenance. That limits the availability of MPI systems. The increased availability of relatively low cost femtosecond fiber lasers around 780-790 nm and 1030-1080 nm also provides a realistic

alternative for light sources for multi-photon imaging (MPI). An alternative option to all above mentioned lasers could be VECSELs. A possibility of multiphoton imaging employing VECSELs as excitation source have already been successfully demonstrated.

2.1.2 Theory of MPI

Maria Göppert-Mayer developed the Dirac formulation of the second-order time-dependent perturbation theory for two-photon absorption and emission in her PhD dissertation. As a result, this theory could be applied in order to calculate transition probability for two photon absorption, and two photon absorption cross – section. The following calculations of one and two photon excitation probability are based on [121]. The probability of transition for two-photon from ground state *n* to excited state *m* via an intermedite state *k* could be written as:

$$P_m^{(2)}(t) = \frac{2\pi t}{\hbar^3}\left|\sum_k \frac{\left|\langle\psi_n|\vec{\mu}\hat{\xi}|\psi_k\rangle\right|\left|\langle\psi_k|\,\vec{\mu}\,\hat{\xi}|\psi_m\rangle\right|\xi^2}{\omega_{kn}-\omega/2}\right|^2 \rho\left(\frac{\omega}{2}=\omega_{mn}\right) \quad (4)$$

Here, sum is over the intermediate virtual states *k*, $\hat{\xi}$ denotes unit vector, ρ is the density of the excited states, ω is angular frequency,$\omega_{mn} = (E_m^{(0)} - E_n^{(0)})/\hbar$ is Bohr frequency Transition rate $r_{n\to m}^{(2)}$ in case of two-photon excitation could be calculated as:

$$r_{n\to m}^{(2)} = \frac{\partial}{\partial t}\left(P_m^{(2)}(t)\right) = \frac{2\pi}{\hbar^3}\left|\sum_k \frac{|\vec{\mu}_{nk}||\vec{\mu}_{km}|\left|\vec{E}\right|^2}{\omega_{kn}-\omega/2}\right|^2 \rho\left(\frac{\omega}{2}=\omega_{mn}\right) \quad (5)$$

$$\vec{\mu}_{nm} = \sum_j \int \psi_n^* \,\overline{\mu}_j \psi_m d^3\vec{r} \quad (6)$$

Finally, for two photon absorption process the transition rate is given by:

$$r_{n\to m}^{(2)} = \sigma_{n\to m}^{(2)}(\omega) I^2 \quad (7)$$

Where $\sigma_{n\to m}^{(2)}$ denotes two-photon absorption cross-section that could be calculated as:

$$\sigma_{n\to m}^{(2)} = \frac{2\pi}{\hbar^3}\left|\sum_k \frac{|\vec{\mu}_{nk}||\vec{\mu}_{km}|}{\omega_{kn}-\omega/2}\right|^2 \rho\left(\frac{\omega}{2}=\omega_{mn}\right) \quad (8)$$

The two-photon absorption process is a multiple step process, where photons are absorbed near simultaneously (~10^{-16} s), transition occurs from the ground state to the excited state via intermediate virtual state and absorption of both photons occurs within a single quantum event. Also, the two photon absorption transition rate is proportional

to the squared intensity of the excitation light, and that enables the excitation to be highly spatial-limited, allowing effective scanning possibility.

In addition, two photon and one photon excitation have different selection rules. In case of one photon excitation, transition probability is given by:

$$P_{i\to f} = \left|\langle\psi_f|\vec{\mu}\hat{\xi}|\psi_i\rangle\right|^2 = \left|\langle\psi_f|e\vec{r}\hat{\xi}|\psi_i\rangle\right|^2 \quad (9)$$

Whereas for two photon process, transition probability is:

$$P_{i\to f} \propto \left|\langle\psi_f|e\vec{r}\hat{\xi}|\psi_k\rangle\langle\psi_k|e\vec{r}\hat{\xi}|\psi_i\rangle\right|^2 \quad (10)$$

From (9) and (10), it could be seen that two dipole terms in case of two photon excitation allow also transition between two states of the same parity, that are forbidden in one photon excitation process. Therefore, the states that could not be accessed by one photon excitation could be accessed by two photon excitation. High spatial and temporal photon density is needed to allow efficient practical realization of multiphoton excitation in order to compensate the low probability of multiphoton absorption event. This was achieved using high NA objectives, and ultrafast lasers combined with efficient two-photon excited fluorophores and biomarkers. In practice, many parameters need to be taken into account for efficient MPI, such as laser characteristics, NA of used objectives, type of the sample used, the lifetime of fluorophore used, etc. Theoretical treatments of two photon imaging have shown that the key laser parameter for two photon signal is the product of peak power and average power. This has been simplified into a figure of merit (FOM) [122], which presents the product of peak and average power as a simple parameter, removing dependencies such as fluorophore lifetime and local biological environment. The FOM is shown in equation (11), where P_{ave} is the average power, F_{rep} is the pulse repetition rate and τ_{pulse} is the pulse duration.

$$FOM = \frac{P_{ave}}{F_{rep}\tau_{pulse}} P_{ave} \quad (11)$$

The quality of multiphoton images has been assessed at a number of discreet operating points, using a range of different lasers on a range of different MPI microscopes and samples. The resulting FOM figure from [123] is shown on a Figure 3.

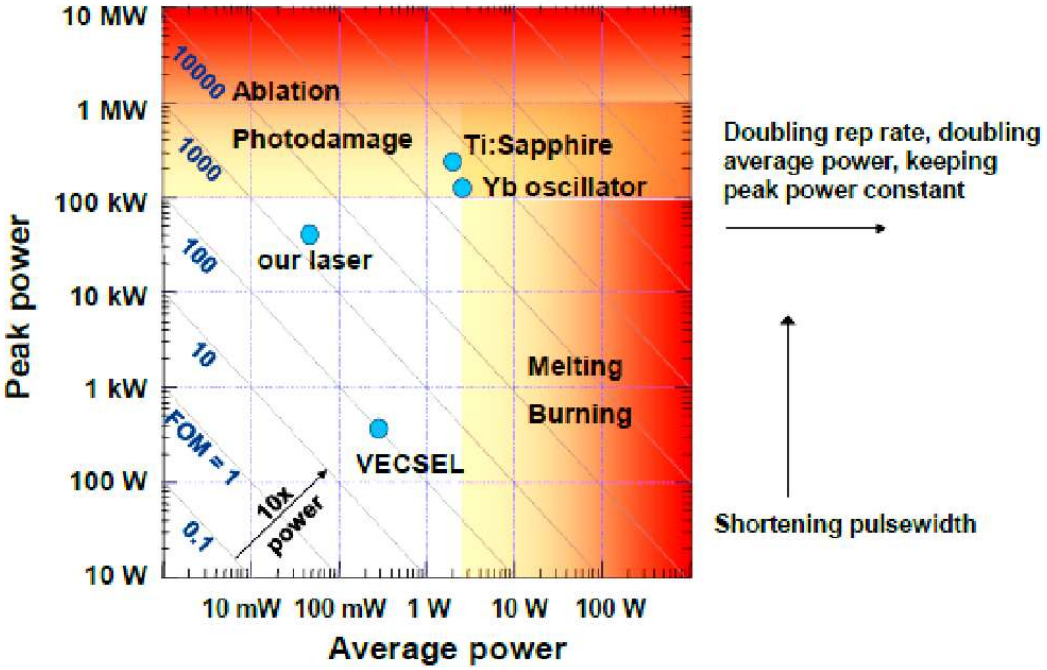

Fig. 3. FOM of VECSEL, Yb oscillator, and typical Ti:Sapphire laser as given in [123]. Red regions represent areas not suitable for MPI due to photobleaching / photodamaging / ablation

To date there has been no systematic experimental study of the validity of the FOM for large parameter space. Therefore, it is important to validate FOM over range of parameters space using common widely-available samples and fluorophores. It will allow to asses a potential of a given laser for MPI application and potentially lead to compact and low cost MPI systems.

2.1.3 Typical MPI: experiment implementation

In laser scanning microscopy, images are acquired using point-by-point scanning of the sample with a focused laser beam. In 1990 Denk, Strickler and Webb demonstrated multiphoton imaging using mode-locked femtosecond laser and high numerical aperture objective. Typical multiphoton imaging system includes pulsed laser source, galvanometer – driven scanner, scanning lens, high numerical aperture (NA) objective and photon sensor as shown on a Figure 4.

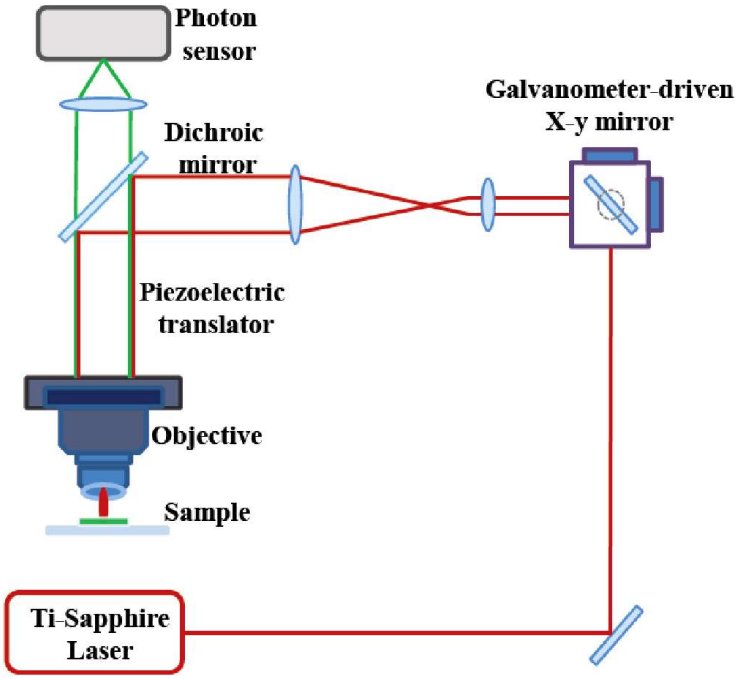

Fig. 4. Typical multiphoton-imaging setup including scanning fluorescence microscope, pulsed excitation laser and detection system. Excitation beam path labeled red and detection path labeled green. (modified from [124]).

Images are formed by raster scanning using x-y mirrors in a galvanometer driven scanner. A dichroic mirror reflects the excitation light from beam expander to the high NA objective that maximizes the excitation efficiency, and transmits fluorescence emission, forwarding it to photon sensor. Photomultiplier tubes are the most common detectors used in multiphoton imaging at the moment, providing relatively good sensitivity over the active area. Other detection systems that are in use for MPI applications are charge-coupled device cameras, avalanche photodiodes and micro-channel plates. As an alternative to the galvanometer-based scanners, acousto-optic deflector scanners could be implemented. These scanners are based on the acousto-optical effect and therefore they benefit from less inertia, also scanning of variable

regions of interest became available. The main disadvantage of acousto-optic deflectors is that they largely rely on dispersive properties of the crystals used. Another alternative offering high scanning speed is polygonal mirror scanners but in this case overall complexity of resulting experimental setup significantly increases.

2.2 Experimental introduction

Critical to the development of any MPI system is a clear understanding of the impact of laser source parameters on multiphoton image quality. Theoretical treatments of two photon imaging have shown that the key laser parameter for two photon signal is the product of peak power and average power. This has been simplified into a figure of merit or FOM, which presents the product of peak and average power as a simple parameter, removing dependencies such as fluorophore lifetime and local biological environment. The quality of multiphoton images has been assessed at a number of discreet operating points, using a range of different lasers on a range of different MPI microscopes and samples. The optimal laser parameters for particular cases of MPI was extensively studied in relevant literature before [125], but to date there has been no systematic study of the validity of the FOM over the large parameters space.

Here I experimentally study the effect of repetition rate and pulse duration on two photon signal using commercial multi-photon microscope Nikon Eclipse TE 2000-U and an EKSPLA FF3000 femtosecond fiber laser, within 336fs – 3.5 ps pulse duration range and repletion rate from 2.85 MHz to 90 MHz. The SYTOX Green-labeled mouse intestine and fluorescein labeled 1μm beads were used as samples.

2.2.1 Methods and setup

To study the effect of repetition rate and pulse duration on two photon signal a commercial multi-photon microscope and fiber laser were used. The fiber laser was an EKSPLA FF3000, with average power of 2.65 W, pulse duration of 336 fs and selectable repetition rate from 45 MHz to 2.85 MHz in fractional steps through an integrated pulse picker between the master oscillator and power amplifier. As shown in Figure 5 a) the output of the laser was passed through a motorised half wave plate followed by a polarizer to control the power at the sample plane in the microscope, and a telescope to match the collimation and beam diameter to the microscope's input requirements. The microscope was a Nikon Eclipse TE 2000-U and the objective used was a ×20 Nikon Plan Fluor oil-immersion. Imaging was done using Laser Sharp 2000 software which allowed control of PMT gain, scan speed and image averaging. In all cases no image averaging was used and a constant scan speed was used throughout. The PMT gains were selected to maximize the parameter range that could be accessed for a given setting, enabling quantitative comparisons to be made.

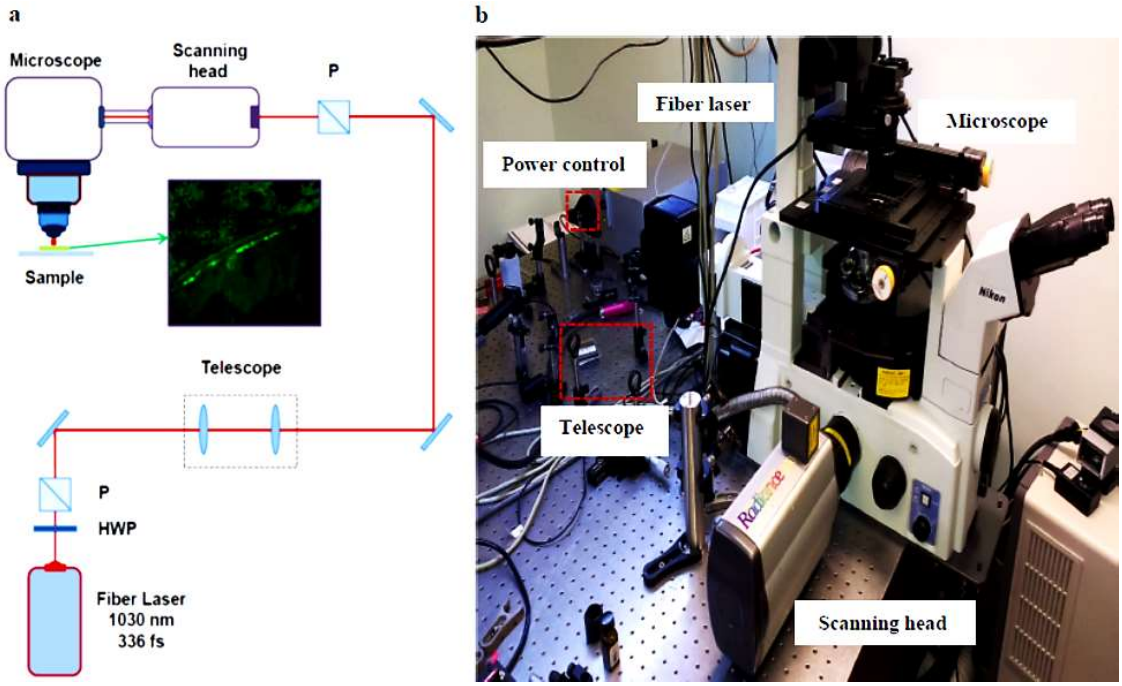

Fig. 5. (a) Schematic of the experimental system used to deliver the output of the fiber laser to the microscope. (b) Photo of the system being used. Excitation laser, scanning head and microscope used for image acquisition are shown.

This imaging system was tested using various samples including convolaria, SYTOX Green-labeled mouse intestine and mouse gut sections, 1 micron Fluorescein-labeled beads and bovine epithelia cells. Some examples of images obtained are shown below on Figures 6-8. All the images where acquired using one particular PMT channel, therefore actual colors of the images are false colors used for convenience.

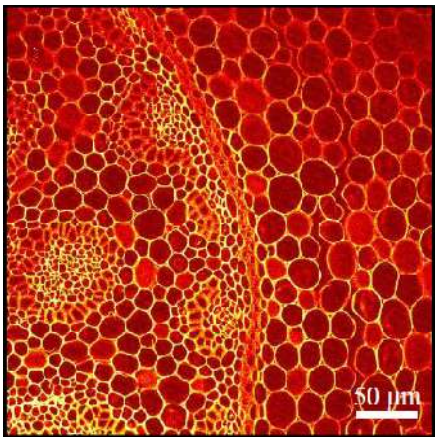

Fig. 6. Two photon image of convollaria, 23 mW on a sample plane using 336 fs pulses at 2.85 MHz

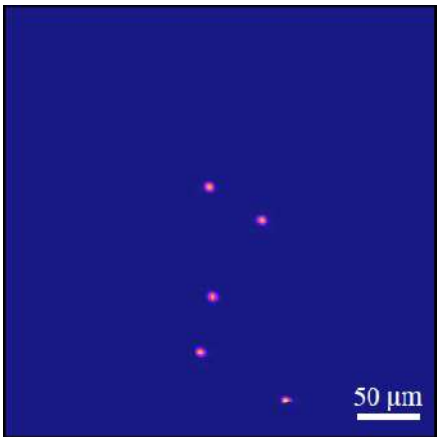

Fig. 7. Two photon image of Fluorescein-labeled 1 micron beads.

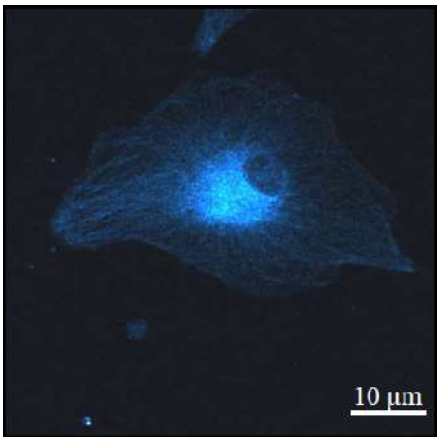

Fig.8. Two photon image of BPAE cells labeled with DAPI, BODIPY and Texas Red. Average power on a sample is 40 mW, repetition rate 2.85 MHz, pulse duration 336 fs.

Setups to vary the repetition rate or pulse duration are shown in Figure 9 (b) and (c), and could be inserted at the point indicated in Figure 9 (a). Repetition rates from 2.85 MHz to 45 MHz could be achieved directly from the fiber laser, but in order to reach a repetition rate close to that of typical Ti: Sapphire laser systems the arrangement shown in Figure 5(b) was used. The system splits the 45 MHz pulse train in two using a polarizing beam splitter and delays one output with respect to the other with an additional path length of 3.33m, before recombining the beams using a non-polarising beam splitter. This reduced our maximum average power for the 90 MHz case to 50% of the other repetition rates. To vary the pulse duration a grating stretcher was built. By controlling the grating spacing the pulse duration could be varied between 336 fs and 3.5 ps. A schematic of this setup is shown in Figure 2(c). The grating compressor had an efficiency of 85% and the pulses were characterized both before the microscope and at the image plane using a commercial Mesa Photonics FROGScan, which uses the frequency resolved optical gating technique.

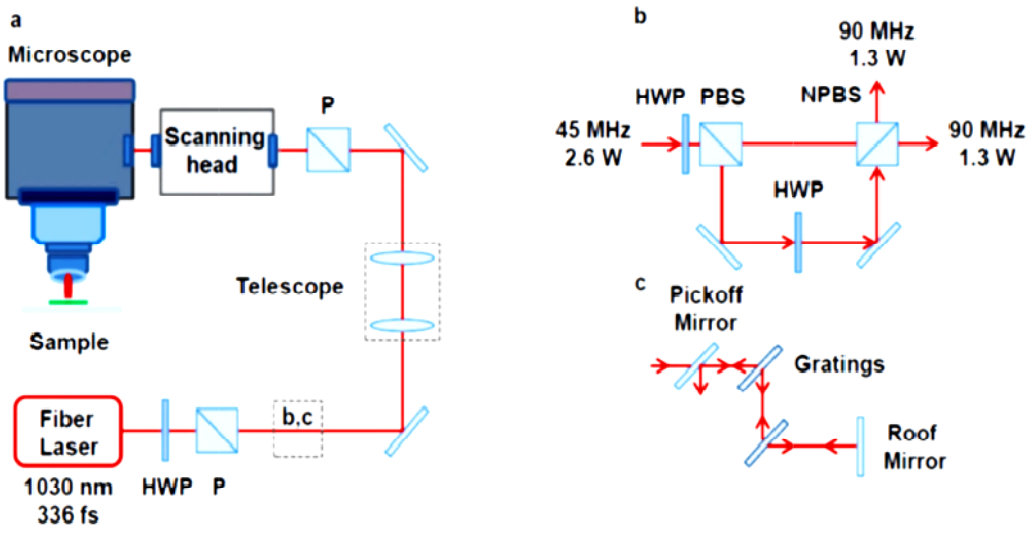

Fig. 9 (a) Schematic of the experimental system used to deliver the output of the fiber laser to the microscope. (b) To reach 90 MHz repetition rate, a pulse interleaving scheme was implemented to be installed just after power adjustment unit. (c) The pulse duration was controlled using a grating compressor, which was added for experiments where pulse duration was varied. (HWP - half-wave plate, P – polarizer, PBS and NPBS – polarizing and non-polarizing beam splitters).

Two samples were studied. One consisted of commercially available 1 micron beads labeled with Fluorescein, which were dispersed on a microscope slide such that individual beads could be imaged. Due to variability we selected beads which produced a two photon signal within a 10% range under low power excitation at 45 MHz for all experiments. Furthermore, for each excitation parameter combination we imaged three beads, providing us with both an average signal and uncertainty. Individual beads were only used for a single measurement of one parameter combination to ensure that photo damage could not affect subsequent measurements. The full experiment for either repetition rate or pulse duration was performed on a single day to minimize and impact from ageing. The second sample consisted of a section of mouse intestine labeled with SYTOX Green. Representative images of both samples are shown in Figure 10.

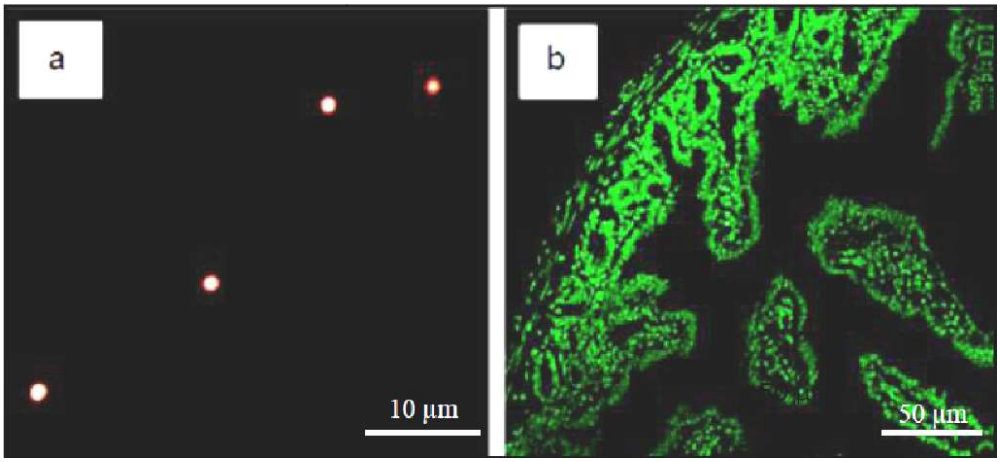

Fig. 10. Two photon images of Fluorescein-labeled 1 micron beads
(a), and SYTOX Green labeled mouse intestine section (b).

This was prepared using standard techniques and the sample was checked for uniformity of fluorophore distribution before imaging was done. Images were taken on a single area as no signs of photo damage were observed across the parameter range we accessed. In the case of beads we extract the maximum signal from the image of each bead using ImageJ - an open source image processing program designed for scientific multidimensional images, and in the case of the intestine sample we use the average image intensity, also found using ImageJ. Microscope resolution was ~0.5 µm. The resolution of acquired images was 512x512 pixels, with a pixel size of ~0.69 µm. The laser spot size on a sample plane was ~1.7 µm.

2.2.2 Results and discussions

Figure 11 show the region of FOM that have studied in this thesis, along with a representative range of points previously reported in the literature using several source laser types: VECSEL, Laser diode, Ti:Sapphire, Er fiber laser, Yb fiber laser.

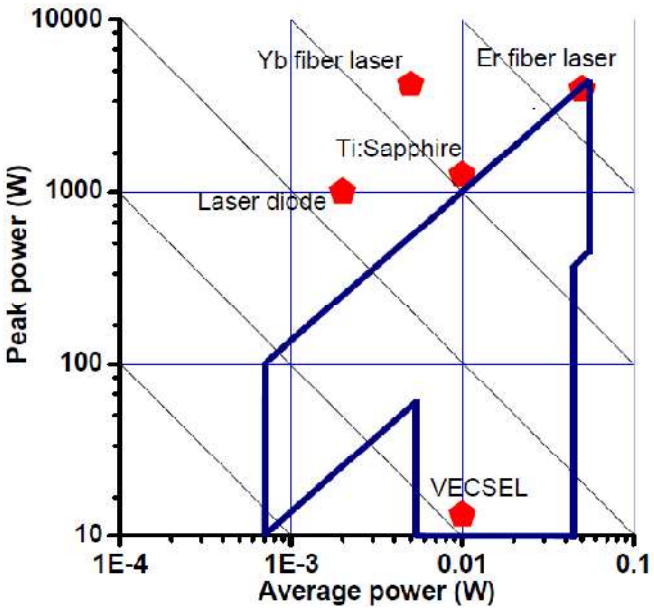

Fig. 11. Figure of merit shown as a function of peak power and average power on the sample. The area inside the line is the parameter space that we study here and pentagons are associated references for some representative reports of two photon microscopy in terms of FOM for a range of different laser sources. The diagonal lines representing lines with the same FOM, but varying peak power and average power.

The two-photon signal in samples of both Fluorescein-labeled beads and SYTOX Green labeled mouse intestine, excited at a wavelength of 1030 nm using a commercial femtosecond fiber laser, was measured. Two photon signal as a function of repetition rate between 2.85 and 90 MHz with average power at the sample up to 60 mW and a pulse duration of 336 fs, and as a function of pulse duration between 336 fs and 3.5 ps with average power at the sample up to 110 mW at a repetition rate of 45 MHz was measured. It was found that the pulse length wasn't important within the range that has been tested. It also been found that for repetition rate there is an optimum, which depends on the fluorophore lifetime and average power; for long lifetime fluorophores or if only minimal average power can be tolerated, a lower repetition rate is advantageous, whereas for short lifetime fluorophores a higher repetition rate can be used with no disadvantages.

Figure 12 shows the measured maximum signal averaged over three beads for average powers on the sample between 0.2 and 60 mW, and repetition rates between 2.85 and 90 MHz for the Fluorescein labeled beads. The data is plotted as both maximum signal versus average power on the sample plane in Figure 12(a), (b) and (c), and as maximum signal versus figure of merit in Figure 12 (d), (e) and (f), which are also shown on log-log scales for clarity. It was checked that applying a single PMT gain value for the whole interval of the average powers on the sample between 0.2 and 60 mW leads either to lack of the signal for lower average power values or too fast saturation for higher values. These factors combined with PMT gain nonlinearity lead to data splitting over three PMT gain settings due to the large dynamic range studied with the beads, since normalizing of the curves over the whole dynamic range for direct comparison without splitting was not possible in this case. At low average powers (Figure 12(a)) it can be seen that from 45 MHz down to 7.6 MHz lower repetition rates lead to higher maximum signals as would be expected due to the higher peak power. When plotted as a function of figure of merit, as in Figure 12(d), it is clear that over this repetition rate range the maximum signal is constant for a given figure of merit. However, it is also clear that there is a lower limit to the increase in signal, as can be seen with the 2.85 MHz repetition rate, which has lower signal than the 7.6 MHz repetition rate in Figure 12(a), and therefore lower gradient in Figure 12(d). This is most likely due to fluorophore excitation saturation, as damage does not seem to be the dominant process at these low average powers. The same broad trend can be seen at mid-and high powers in Figure 12(e) and (f). At high repetition rates the maximum signal is determined by FOM alone irrespective of repetition rate, but at lower repetition rates the signal is lower than would be expected given the value of FOM. Indeed, in Figure 12(f) it can be seen that the gradient of both the 2.85 and 7.6 MHz repetition rate data has levelled off, showing saturation of maximum signal, and in many cases photo damage was observed. Here the low repetition rates have pushed the peak power beyond the damage limit for this sample.

Overall it is clear that there is an optimum in terms of repetition rate, where using a lower repetition rate allows signal to be maximized for a given average power, but below a certain lower limit it leads to photo bleaching and damage. An additional consideration is the ratio of the repetition rate to the dye lifetime. The fluorescence lifetime of Fluorescein is ~4.1 ns [126], and a 90 MHz repetition rate corresponds to 2.7 times the fluorescence lifetime, meaning that the dye may not have entirely recovered

between pulses. It is not clear from data presented here, that this has had an impact, but clearly this should be taken into account when using fluorophores with longer lifetimes or higher repetition rate lasers. Finally, while the relationship between signal and figure of merit is not perfectly linear, it is clear that the assertion that MPI signal is proportional to the figure of merit is broadly correct over a wide parameter range provided that parameters are chosen where damage and saturation are avoided.

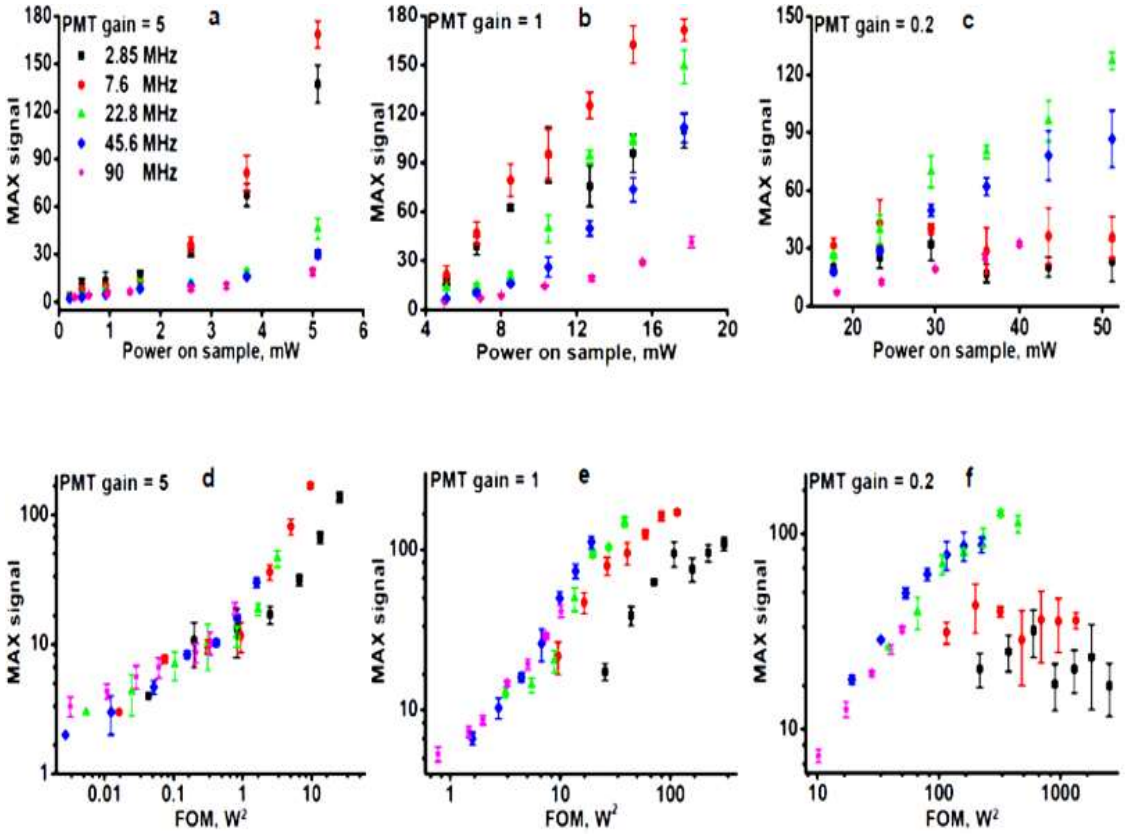

Fig. 12. Maximum signal as a function of average power on the Fluorescein-labeled beads for repetition rates 2.85 90 MHz, for PMT gain = 5 (a), PMT gain = 1 (b), PMT gain = 0.2 (c). The same data is shown in terms of figure of merit in (d), (e), and (f), where log-log scales have also been used for clarity.

Figure 13 shows the corresponding experimental data recorded for the mouse intestine sample labeled with SYTOX Green. We use a single PMT gain range, which restricts our average power range between 5 and 20 mW at the sample. Below a figure of merit of ~7 W^2 we see the noise floor of our detection, but above this point a similar trend is demonstrated as in the case of the beads, where lower repetition rate leads to higher signal, but where equivalent FOMs lead to equivalent maximum signals.

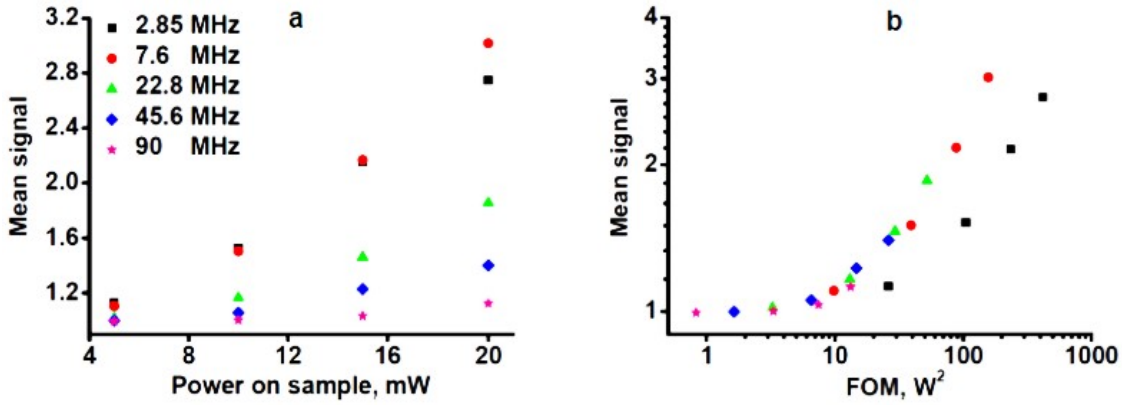

Fig. 13 (a) Mean signal versus average power on the sample for a range of repetition rates for the SYTOX Green-labeled mouse intestine. (b) The corresponding figure of average signal versus FOM

Again we start to see a lower repetition rate limit with the 2.85 MHz repetition rate which deviated from this trend. The reduction in signal at 90 MHz is not observed in this case, which would be expected due to the shorter fluorescence lifetime of SYTOX Green. This is used as a fluorophore for FLIM type imaging techniques, so the fluorescence lifetime is sensitive to environment, but is typically in the range of ~2 ns [127]. Fluorescence lifetime is sensitive to various factors defined by the fluorophore structure and external factors such as temperature, polarity, and the presence of fluorescence quenchers. Therefore, for such fluorophores the repetition rate tunability allows to find an appropriate repetition rate value to allow complete recovery of the fluorophore between excitation pulses.

By inserting the pulse stretcher between the fiber laser and the microscope it was possible to examine the effect of varying the pulse duration. The average signal versus average power on the sample for a range of pulse durations between 336 fs and 3.5 ps, along with the corresponding figure of mean signal versus FOM for the SYTOX Green-labeled mouse intestine sample is shown if Figure 14 (a) and (b) respectively. Here, a single PMT gain and a repetition rate of 45 MHz was used throughout. The pulse duration was measured at the sample plane. Figure. 14 (a) clearly shows the average signal increases with decreasing pulse duration, due to the increased peak power on the sample for a given average power. When viewed in terms of figure of merit (Figure 13(b)) the curves overlap for all pulse durations. It is therefore clear that it is possible to use longer pulses than the ~150 fs usually used so long as correspondingly higher average powers can be tolerated by the sample with no detrimental effects.

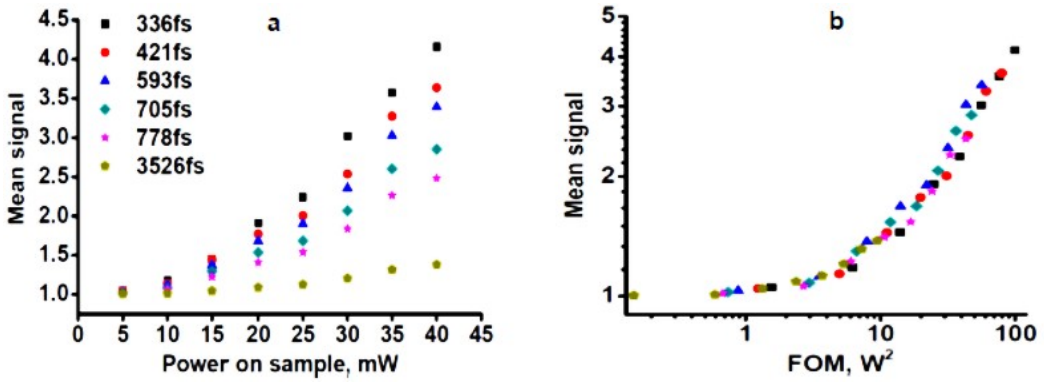

Fig. 14 (a) Mean signal as a function of average power on the SYTOX Green-labeled mouse intestine sample for a range of pulse durations between 336 fs and 3.5 ps. (b) Mean signal versus FOM for the same range of pulse durations. Signal is not affected by pulse duration provided that the average power is adjusted to keep the FOM constant.

Figure 15 shows the measurements of maximum signal from Fluorescein-labeled beads for three different pulse durations and average powers up to 110 mW. The same independence of the signal on pulse duration is found in the bead samples as was observed in the mouse intestine sample. The power range was limited by the power of the laser in the case of 336 fs pulses, and by the power of the laser and efficiency of the pulse compressor in the case of the longer pulse durations. Only with the shortest pulses can damage start to be seen, which seem to be predominantly peak power driven.

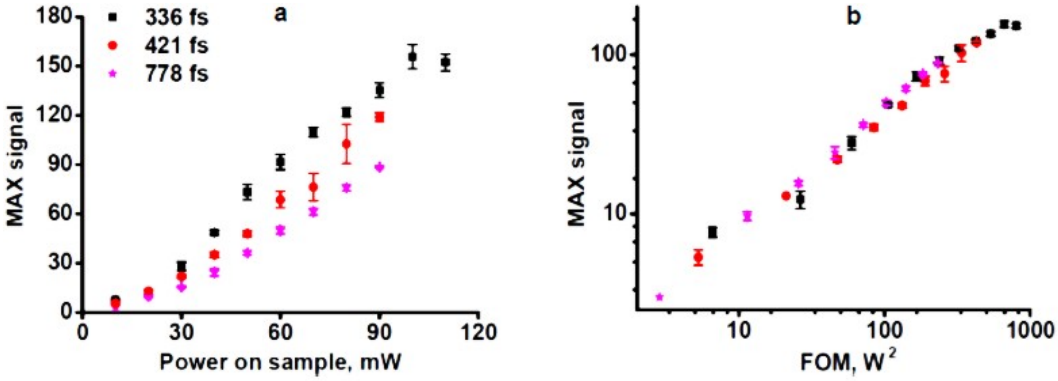

Fig. 15 (a) Average signal versus power on the Fluorescein-labeled bead sample pulse durations between 336 fs and 778 fs. (b) Average signal versus FOM for the same range of pulse durations. It can be seen that they all follow the same trend within experimental variation.

2.3 Conclusions

With the increased commercial availability of highly flexible alternatives to traditional Ti:Sapphire lasers it is important to understand the optimum laser parameters for multiphoton imaging. Here the widely-used FOM approach has been for the first time validated and tested over a large parameter space. The effect of repetition rate and pulse duration on two photon signal level in two samples, Fluorescein-labeled 1 micron beads, and SYTOX Green-labeled mouse intestine using a commercial femtosecond pulse fiber laser has been experimentally studied. It was shown that there is an optimal repetition rate for a given sample and average power, with excessively low repetition rates leading to lower than predicted signal levels due to bleaching and/or damage, and excessively high repetition rates leading to lower than expected signal levels due to incomplete recovery of the fluorophore between excitations. In performed experiments using a 336 fs pulse at 1030 nm, a lower repetition rate, between 20 and 40 MHz appears to be the best compromise on maximum signal at low average powers, and the ability to use higher power excitation if required. Fiber lasers can easily be made to operate in this pulse repetition rate range, and can also be made to have variable repetition rates with the integration of a relatively low cost pulse picker between the master oscillator and power amplifier, potentially allowing their output to be matched to the optimum repetition rate for a given sample and fluorophore. More surprisingly, it was observed that pulse duration has little effect on multiphoton signal provided that the average power can be adjusted to keep the figure of merit constant. This is interesting as typically the difference in complexity and cost of a 100 fs pulse laser and a 1 ps pulse laser can be significant. Additionally, if longer pulse durations can be used, less focus needs to be placed on dispersion in the microscope and sample, where pre-chirping of the shortest pulses is often required before delivery to the microscope. This has the potential for significantly lower cost microscopes, or the straightforward application of advanced adaptive imaging techniques, potentially allowing for deeper tissue imaging or techniques such as imaging through multi-mode fiber [128, 129], where dispersion can be a major limitation. Alternatively, the ability to use longer pulses opens up the possibility of multi-photon microscope systems which use several low cost, fixed wavelength, longer pulse duration laser sources such as picosecond fiber lasers or sub-picosecond optically pumped semiconductor lasers instead of single sources with high cost and complexity.

3. High power 1µm MECSEL development

3.1. Introduction and background

Vertical External Cavity Surface Emitting Lasers (VECSELs), also called Semiconductor Disc Lasers (SDL) are nowadays capable of producing sub-100-fs pulses, multi-kW peak powers, and mode-locking has been demonstrated for wavelength range from 675nm to >2 microns. These flexible, low cost lasers have the potential to allow multi-source multiphoton microscopy system design, similar to those in confocal microscopy, where imaging systems employing several different laser sources to reach a set of required wavelengths. One of the most challenging aspects of VECSELs is the deposition of heat into the active region, leading to strong temperature-dependent performance.

Thermal conductivity of the DBR-forming layers is much worse than thermal conductivity of materials used as heatsink in VECSELs. In addition, a several hundred micron thick substrate on a back side of VECSEL chip also reduces heat transfer rate and efficiency. In contrast recently introduced Distributed Bragg Reflector (DBR) free technology helps to address these challenges. There are two general approaches to cooling VECSELs : first approach based on using crystalline heat-spreaders, and the second includes substrate removal, which allows soldering resulting thin gain chip directly to heatsink. In addition, VECSELs also could be cooled actively and could be made to operate at cryogenic temperatures with the gain chip cooled down to 83 K [130].

The DBR-free VECSEL has been reported, and possibility for the broad-wavelength tuning using this laser was demonstrated. Using the possible approaches for thermal management of such DBR-free VECSELs, the semiconductor membrane external-cavity surface-emitting laser (MECSEL) consisting of a diamond heat spreader sandwiched AlGaInP-based active region design without a monolithically integrated DBR was successfully realized recently [113]. This thesis chapter introduces VECSELS, and describes the successful development of 1µm DBR free VECSEL - Membrane External Cavity Surface Emitting Laser (MECSEL) that demonstrated the record 10.1 W of CW output power for these lasers.

3.1.1 Semiconductor properties, Quantum Wells and Quantum Dots

Modern semiconductor lasers are based on advanced semiconductor multilayer structures grown by epitaxial and chemical vapor deposition methods. Semiconductor materials are grown according to various designs and materials composition, allowing electron bandgap engineering and quantum confinement controlling. Figure 16 shows the energy-band diagram for silicon and gallium arsenide.

The energy-band diagram in different directions is varying since the lattice periodicity is also different in various directions. GaAs belongs to a family of direct semiconductors, meaning that for an electron transition from the valence to conduction band, no change of momentum needed. In case of Si, a change of momentum is required during a transition and Si is therefore referred to as indirect semiconductor.

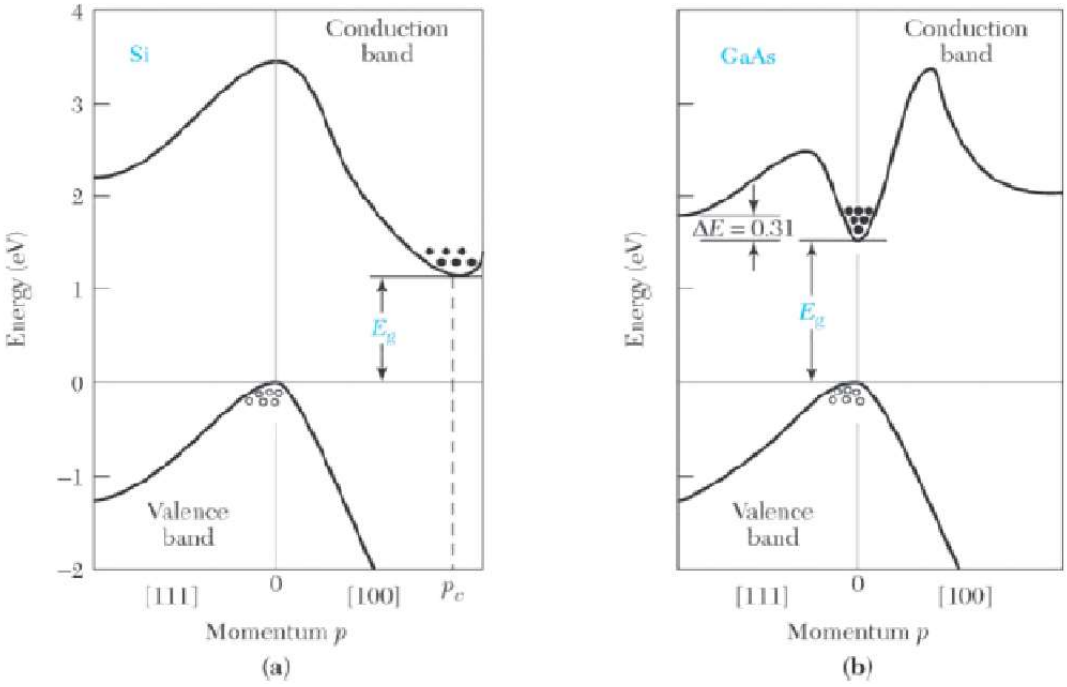

Fig.16. Energy band structures of Si a) and GaAs b) [131]

The difference between direct and indirect semiconductors is crucial for semiconductor lasers, where direct semiconductors are normally used to allow efficient photon generation due to high radiative-transition probability, with most extrema occur at the edges or a centre of Brillouin zone where k=0. According to the momentum conservation, the difference between the initial and final electronic state must be equal to the momentum of the photon involved. For example, the momentum difference in case of GaAs, k $\approx 2.5\times10^{7}$ m^{-1}, and the edge of Brillouin zone is at k $\approx 10^{10}$ m^{-1}.

Therefore, only states close to k=0 will lead to contribution to the optical transitions and conduction bands in this case could be approximated with parabolic function.

The lattice constant-bandgap relation for a set of common binary semiconductor materials is shown on a Figure 17. One layer of semiconductor material can be grown on top of another whilst avoiding strain creation only in the case of the crystal structure and lattice constant of these materials matching.

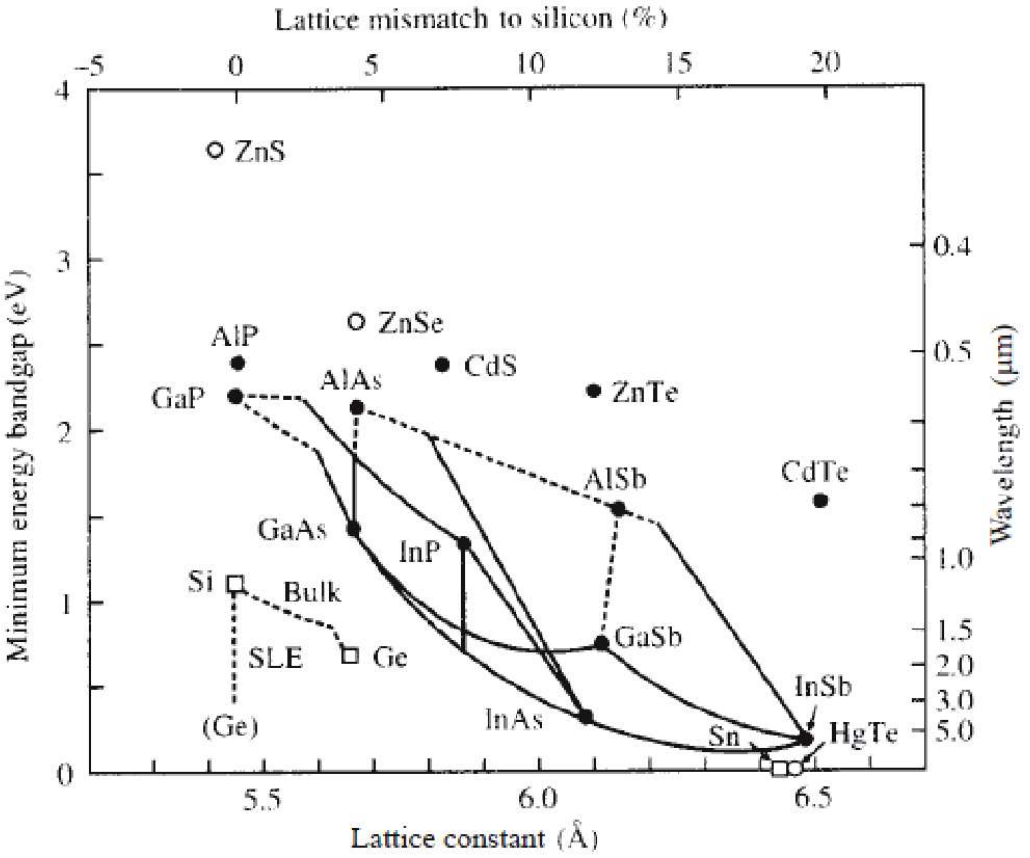

Fig. 17. Band gap Vs Lattice constant of common semiconductors. Curves connecting compounds that have one common constituent. Solid lines corresponds to direct band gaps and dashed lines show indirect band gaps [132].

The strain induced by lattice mismatch cause dislocations that causes reduced lifetime and efficiency of resulting device. For some particular material combinations, a layer of material could be grown with defined thickness on top of another material, relaxing the strain before dislocation is formed. It is possible also to efficiently combine layers of different materials using combination of ternary alloys, so this connecting two binary compounds that have common constituent. That gives resulting structure same lattice constant but with different band gaps. The IR MECSEL structure used in this thesis has an active region with ten $In_{0.13}GaAs$ quantum wells that are embedded in strain

compensating $GaAsP_{0.06}$ barrier layers. GaAs spacer layers are used to position the single quantum wells in the antinodes of the electric field.

Semiconductor laser threshold can be reduced by controlling the dimensions of gain medium. When the de Broglie wavelength of the electron becomes comparable with the size of the region where the electron motion appear, quantum properties of the electron become important. Quantum wells and quantum dot based structures allowed significant increase in efficiency of semiconductor lasers.

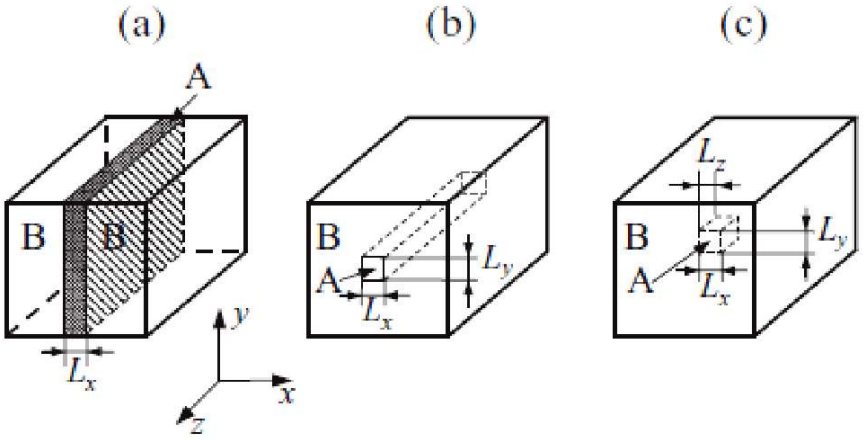

Fig. 18. Types of nanostructures: a) quantum well, b) quantum wire, c) quantum dot [135]

The effective de Broglie wavelength of an electron in crystalline material could act as a space quantization criterion:

$$\lambda = \frac{h}{p} = \frac{2\pi\hbar}{mv} = \frac{2\pi\hbar}{\sqrt{3mk_BT}} \qquad (12)$$

In the case when the condition $L_x \leq \lambda$ is satisfied, it corresponds to free motion of the electron in two directions, and the resulting structure is known as quantum well (Figure 18 a). If electron motion is restricted in two dimensions: $\{L_x \leq \lambda \; ; \; L_y \leq \lambda \}$, then structure is called quantum wire (Figure 18 b) . Finally, if conditions $\{L_x \leq \lambda \; ; \; L_y \leq \lambda \; ; \; L_z \leq \lambda \}$ are applied, the energy spectrum of the resulting structure is completely quantized, with the final structure called quantum dot (Figure 18 c).

Quantum wells (QWs) represent the simplest nanostructure with quantum confinement applied along only one direction. Structures with quantum wells and barriers have many applications in modern photonics and nanoelectronics. It is possible to combine multiple quantum wells with narrow barriers within one periodic structure

forming a superlattice [133]. In quantum well-based structures, strain could be avoided by sandwiching the quantum well between strain compensating layers.

3.1.2 VECSEL design and growth

Vertical External Cavity Surface Emitting Laser (VECSEL), or Semiconductor Disk Laser (SDL) is a optically pumped semiconductor laser containing a surface-emitting semiconductor gain chip and a laser resonator.

Typical components of the VECSEL are the gain chip mounted on a heat spreader for effective heat removal, a pump laser (usually, diode laser), pump focusing optics, and external output coupling mirror (Figure 19). The laser cavity is formed by a DBR integrated into the gain chip as one mirror, and an external output coupling mirror at the second end of the cavity.

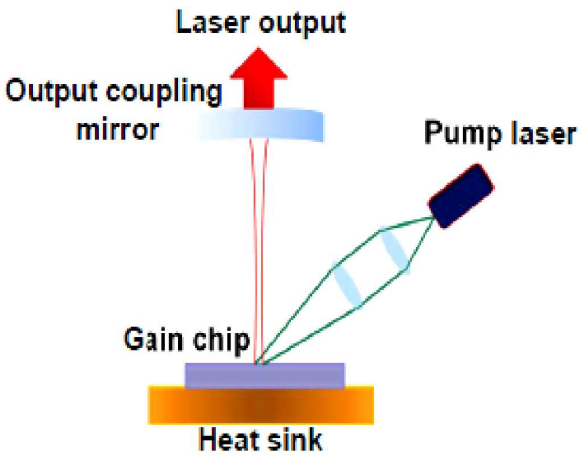

Fig.19. Typical components of the VECSEL

The semiconductor gain region provides gain in a direction perpendicular to the gain chip surface. The actual cavity is formed by the DBR, integrated into the gain chip as one end of the cavity, and the external mirror that act as output coupler and also defines the laser mode as second part of the cavity. Optical pumping makes it possible to obtain power scaling by uniform pumping of a large surface area of the gain chip, and high output beam quality may be obtained by controlling the optical transverse mode using the external cavity. The high output beam quality with M^2 ~1, combined with the possibility to fabricate VECSELs over the wide wavelength range are a few of the many advantages of these lasers.

The VECSELs are normally epitaxially grown either by Molecular Beam Epitaxy or Metal Organic Vapour Phase Epitaxy (MOVPE). The total thickness of a VECSEL gain chip is in a range of a few micrometers without the substrate thickness. A typical

VECSEL chip layer structure is shown in Figure 20. The top cap layer acts as protective layer against oxidation, the active layer is formed by quantum wells or quantum dots, followed by the DBR.

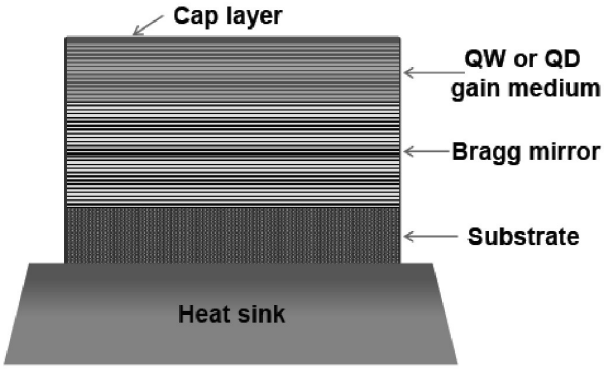

Fig. 20. Typical VECSEL layer structure.

The function of each VECSEL layer could be illustrated using the simplified diagram shown in Figure 21. The VECSEL structure is monolithically grown ensuring lattice-matching to the substrate. The substrate itself could be removed afterwards using various etching methods to improve thermal management. The DBR layer is formed by alternating transparent quarter-wavelength layers with high and low refractive index materials. By gradually increasing the layer quantity, a higher reflectivity can be obtained.

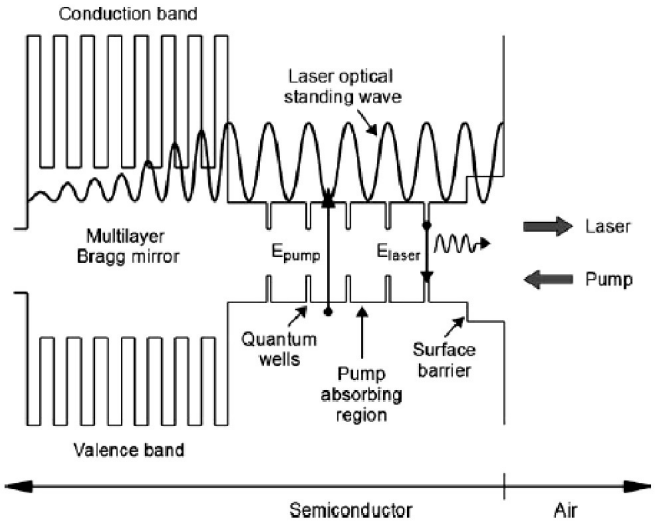

Fig. 21. Layer structure diagram of the typical VECSEL gain sample (from [134])

The active region provides laser gain and includes pump absorbing layers. Excited electrons and holes are generated by high energy pump photons absorbed into the quantum well barriers. Then, the excited electrons and holes diffuse into the smaller

bandgap quantum wells, where they become localized creating population inversion, and undergo spontaneous carrier recombination producing photons. The active region thickness is chosen to allow absorption of most pump light. In order to provide maximum gain, quantum wells are placed at the antinodes of the E-field standing wave, with resulting gain structure arrangement called resonant periodic gain arrangement. Following [134], the semiconductor quantum well gain g could be written as:

$$g = g_o \ln\left(\frac{N}{N_o}\right) \qquad (13)$$

where g_0 – gain parameter of the semiconductor material, N – quantum well carrier density, N_0 – transparency carrier density. According to VECSEL laser threshold conditions:

$$R_1 R_2 T_{loss} \mathrm{e}^{(2\Gamma g_{th} \mathrm{N_W L_W})} = 1 \qquad (14)$$

where T_{loss} – transmission factor due to round-trip cavity loss, R_1 and R_2 – cavity mirror reflectivities, L_w – quantum well thickness, and N_w – the number of quantum wells in the gain medium. Here, Γ denotes longitudinal confinement factor that characterizes the overlap between quantum wells inside the active region and the intracavity optical standing wave.

The carrier density N below threshold can be calculated using incident pump power:

$$N = \frac{\eta_{abs} P_p}{h\nu_p \left(N_w L_w A_p\right)} \tau(N) \qquad (15)$$

In the equation (15), A_p defines the pump spot area, $h\nu_p$ – pump photon energy, η_{abs} – pump absorption efficiency. Carrier lifetime τ can be calculated from:

$$\frac{1}{\tau(N)} = A + BN + CN^2 \qquad (16)$$

where coefficients A, B and C are define the monomolecular, bimolecular and Auger recombination coefficients, respectively.

Resonant periodic gain arrangement provides high electric field on the quantum wells resulting on higher gain and is therefore beneficial for high power CW VECSELs.

In contrast, antiresonant structures have lower gain but better dispersive characteristics and larger gain bandwidth. Figure 22 illustrates the differences of resonant and antiresonant VECSEL structures. The y-axis of the bottom two graphs on a Figure 22 are normalised to 4, since the intensity rather than the E-field is considered in this case. Since $E_{left} + E_{right} = 2E$ and $I = 4E^2$, then with E normalised to 1 this results at axis normalised to 4.

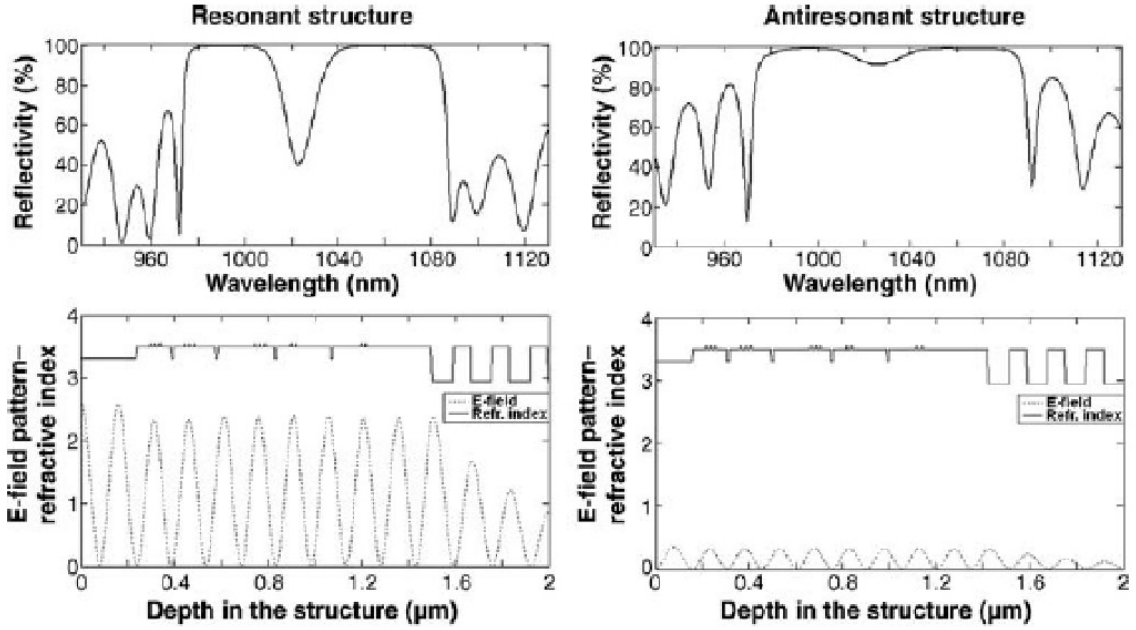

Fig. 22. Resonant and antiresonant VECSEL structures characteristics (from [134]).

Resonant structures are more beneficial in frequency-doubled VECSELs due to additional wavelength-selection, whereas antiresonant structures are preferable for widely-tunable VECSELs. The effective chip gain, following [135], could be calculated as:

$$G_{chip}(\lambda) = \frac{(\sqrt{R_i} - \sqrt{R_{DBR}}g_s)^2 + 4\sqrt{R_i R_{DBR}}g_s sin^2(2\pi L_c/\lambda)}{(1 - \sqrt{R_i R_{DBR}}g_s)^2 + 4\sqrt{R_i R_{DBR}}g_s sin^2(2\pi L_c/\lambda)} \qquad (17)$$

Where g_s – single-pass gain of the structure, R_i and R_{DBR} – air-semiconductor interface and DBR reflectivities, L_c – cavity length.

The confinement window on top of the VECSEL prevents pump-generated carriers from the non-radiative recombination. The final top cap layer is used to prevent the oxidation. As a measure of overlap between the electric field and quantum wells, a longitudinal confinement factor Γ_z was used.

For a sample containing n quantum wells it could be written as:

$$\Gamma_z = \frac{\sum_n |E(z_n)|^2}{|E_0|^2} \qquad (18)$$

Here, E_0 denotes the electric field outside the sample and E (z_n) is electric field at the quantum wells. Longitudinal confinement factor and group delay dispersion in case of resonant and antiresonant samples are shown on Figure 23.

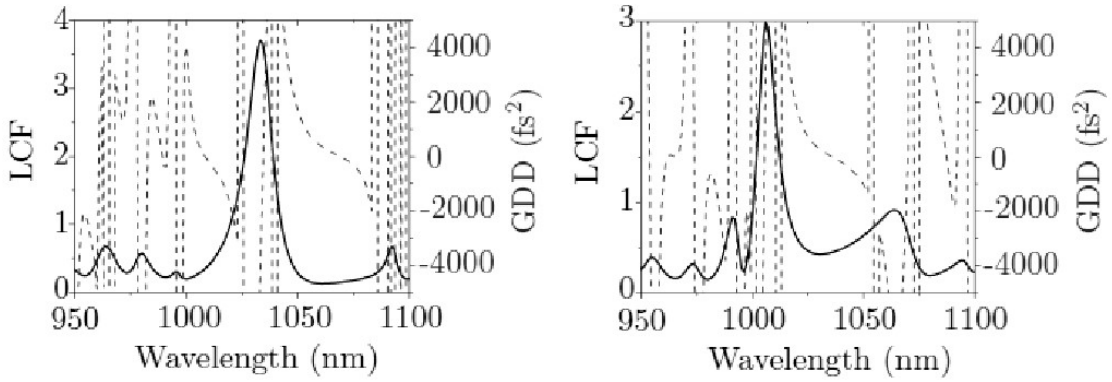

Fig. 23. Longitudinal confinement factor (solid line) and group delay dispersion (dashed line) plotted as a function of wavelength plotted for resonant (left) and antiresonant (right) case for 1035 nm [136].

As could be seen from Figure 22, resonant design is beneficial for high power CW operation due to Longitudinal Confinement Factor (LCF) having high values for the designed wavelength resulting in higher gain. However, GDD in case of resonant design limits its suitability for mode-locking operation due to higher order dispersion. Lower GDD values and broader bandwidth typically make antiresonant design more suitable for mode-locking.

The external cavity of VECSEL allows use different cavity geometries for CW and pulsed operation including common straight cavity, z and v-shaped cavity. However, many other cavity designs also could be employed such as T-cavity containing two VECSEL gain chips used for high-power tunable two-wavelength generation [137] or ring cavity used for colliding pulse mode-locking.

3.1.3 Thermal management and processing

The higher pump photon energy compared to the emitted laser photons is the quantum defect, which is effectively the energy difference between pump and laser photons energies. Heating caused by high quantum defect limits carrier confinement and results in strong temperature dependence of VECSEL characteristics during operation. A lack of efficient cooling will lead to rising active region temperature and thermal escape of excited carriers from quantum wells into barriers resulting at thermal rollover. Another limiting factor is that the thermal conductivity of the relatively thick substrate and DBR layers is very poor. All these factors are highlighting importance of cooling strategies for efficient VECSEL operation and minimization of gain chip temperature rise per unit pump power. To allow heat extraction, a VECSEL gain chip could be directly attached to a heat sink that is cooled by water or a Peltier element. However, in this case the DBR and substrate are limiting heat extraction efficiency due to poor thermal conductivity.

There are two general approaches to cooling VECSELs : the first approach based on using crystalline heat-spreaders bonded to top surface of gain chip, the second includes substrate removal, which allows the resulting thin gain chip to be soldered directly to the heatsink. In addition, VECSELs also could be cooled actively and could be made to operate at cryogenic temperatures with the gain chip cooled down to 83 K.

3.1.4 CW operation, sample characterization and wavelength tuning

A VECSEL gain chip can be characterized using reflectivity measurements in order to characterize the DBR, and by taking photoluminescence (PL) spectra to assess quantum well performance and active region length. Once the VECSEL gain chip is mounted on the heat spreader and introduced in a laser cavity, the output power in CW mode could be measured an laser spectrum taken to further examine the structure properties. Figure 24 shows reflectivity spectra for wafer structure and measured PL spectra of VECSEL wafer.

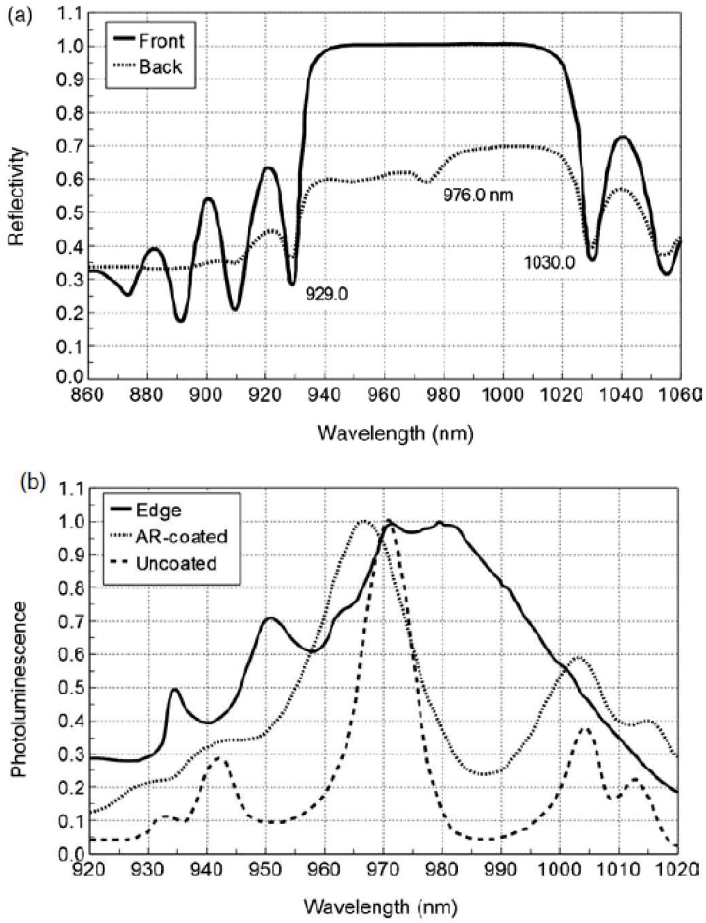

Fig. 24. Reflectivity spectra of the OPS semiconductor wafers – front and back surface reflectivities are shown (a). Normalized PL spectra of the OPS chips. [134]

A combination of PL and reflectivity spectra helps to determine laser material gain spectral locations and resonance peaks that localize laser emission. In the case when strained quantum wells are studied, PL could act as indicator of dark line defects that appear when thickness of the strained quantum wells exceed the critical thickness. PL

emitted by quantum wells in all possible angles, and both edge and top PL could be measured. After PL and reflectivity measurements are performed, the gain sample could be characterized via CW lasing and taking laser spectrum. These measurements helps to further assess laser performance and obtain information on laser threshold, slope efficiency, maximum output power, signs of thermal roll over and laser operating wavelength.

Figure 25 shows representative pump power – output power measurements for CW IR MECSEL studied in this thesis. The structure and performance of this laser will be described in the further chapters of this thesis. Laser threshold was 0.88 W, with maximum output power of 5.34W, slope efficiency was 18%. Measurements were taken at a heat sink temperature of 15 ^{o}C.

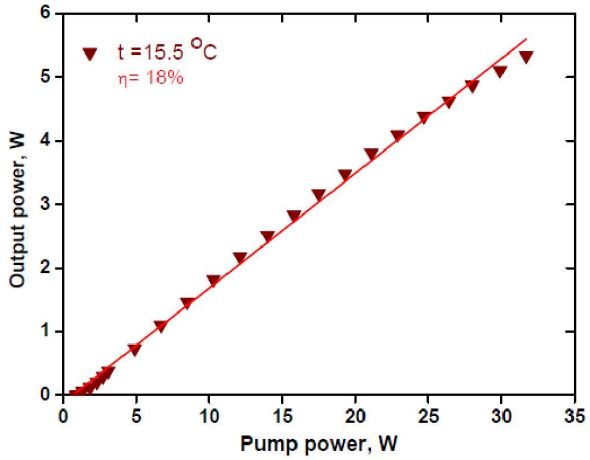

Fig. 25. Pump power Vs output power curve taken at 15 °C for IR MECSEL

Figure 26 shows the laser spectrum of IR MECSEL taken at 15 °C and at 4.9 W of pump power. The operating laser wavelength was ~1007 nm.

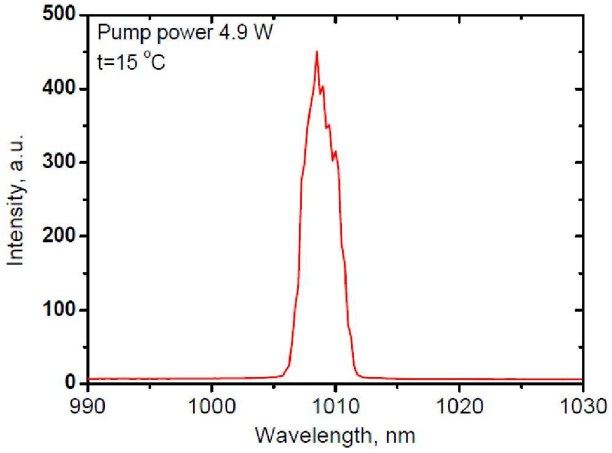

Fig. 26. Spectrum of IR MECSEL taken at 15 °C

VECSEL wavelength can be tuned by introducing a birefringent filter into the laser cavity at Brewster's angle. The filter itself is a thin plate of birefringent material, usually crystalline quartz. When a birefringent plate is placed inside the resonator, it effectively acts as equivalent of an off-axis birefringent plate between the parallel polarizers. Rotation of the filter within the cavity varies the wavelength that experiences zero transmission loses at the second polarizer.

3.1.5 Advanced VECSEL: frequency conversion, mode-locking, single frequency operation

The external cavity geometry and high intra-cavity field intensity combined with use of low transmission output couplers makes VECSELs favorable lasers for higher harmonic generation. Higher harmonic generation has been realized in VECSELs to access new wavelength ranges that otherwise are difficult to achieve. Frequency doubling in VECSELs was used for example to obtain lasing at 325-332 nm and 615 nm. Noncritical phase matching configurations required for frequency doubling could be allowed by a range of nonlinear crystals, such BBO, $LiNbO_3$ and LBO.

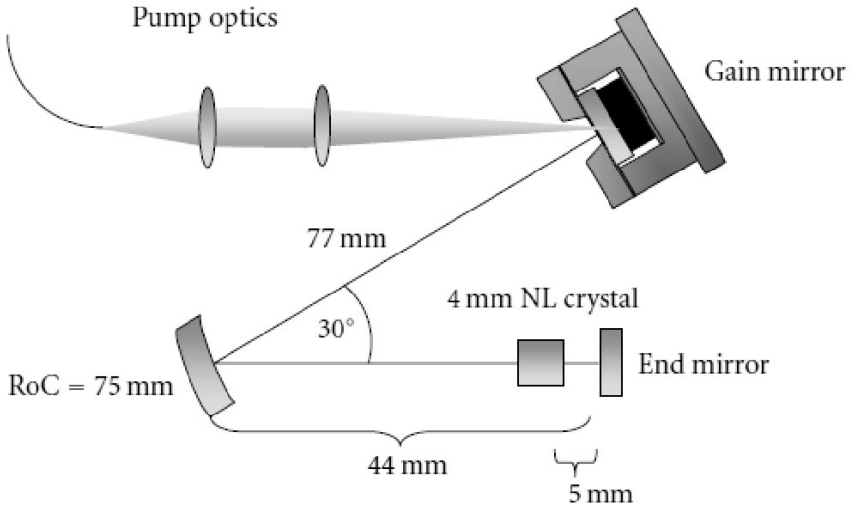

Fig. 27. VECSEL setup for yellow second harmonic generation in free running mode. Modified from [138].

Figure 27 demonstrate yellow-orange radiation generation using V-shaped cavity in a free-running mode and folding mirror that transmits visible light but reflects infrared. Frequency conversion in that experiment was achieved using BBO crystal.

VECSELs also allow single-frequency operation due to compact standing wave cavity geometry that could be relatively easily isolated from acoustic noise. In single-frequency operating lasers, quasi monochromatic output exhibits low noise and has narrow linewidth, which makes these lasers good candidates for a range of applications including spectroscopy, metrology and laser cooling. Single frequency operation in VECSELs was first realized two years after first VECSEL was reported by Kuznetsov. Figure 28 represents a scheme to achieve active VECSEL stabilization using laser

frequency locking to reference cavity via electronic feedback loop. The reference cavity output was measured using a photodiode.

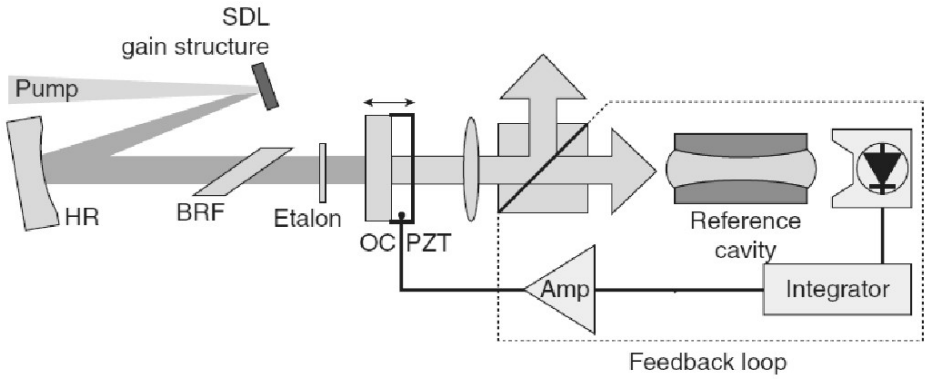

Fig. 28. Activlely stabilized VECSEL [151]

A record to date single frequency output power from VECSEL of 23.6 W at 1013 nm was achieved by [139].

Mode-locking is the process of locking the pulse between longitudinal modes of the laser. Active mode-locking could be obtained by periodic modulation of the resonator losses or of the round-trip phase change using for example electro-optic and acousto-optic modulators. In active mode-locking, the modulator acts as periodic shutter that opens once per round-trip time of the pulse. Active mode-locking of a VECSEL using a low-loss vertical cavity modulator was demonstrated by [134]. However, active mode-locking becomes ineffective for very short pulses, and
this limits the attainable pulse width. The shortest pulses reached so far were obtained using passive mode-locking. Passive mode-locking in VECSELS could be achived by using a SESAM. The absorption of the SESAM varies due to saturation effects induced by the laser intracavity field. A SESAM consist of DBR with incorporated saturable absorber based on quantum wells or quantum dots (Figure 29).

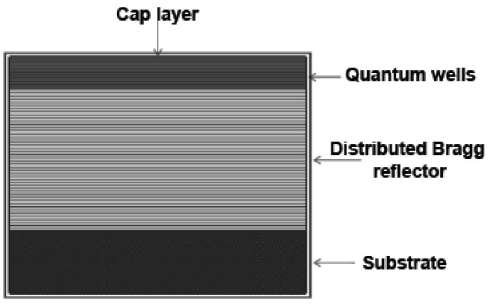

Fig.29. Layer structure of the SESAM

A semiconductor absorbs light if the photon energy is high enough to excite carriers from the valence band to the conduction band. Under conditions of strong excitation, the absorption is saturated because possible initial states of the pump transition are depleted while the final states are partially occupied. On a time scale between a few picoseconds and a few nanoseconds the carriers will be removed by recombination and trapping. The longer time constant results in a reduced saturation intensity for a part of the absorption, which facilitates self-starting mode-locking, whereas the faster time constant is more effective in shaping sub-picosecond pulses. Therefore, SESAM allows reach self-starting mode-locking. To allow power density on the SESAM to be higher than on the VECSEL gain chip, different cavity designs with incorporated SESAM could be used. An example of such a cavity is shown on a Figure 30.

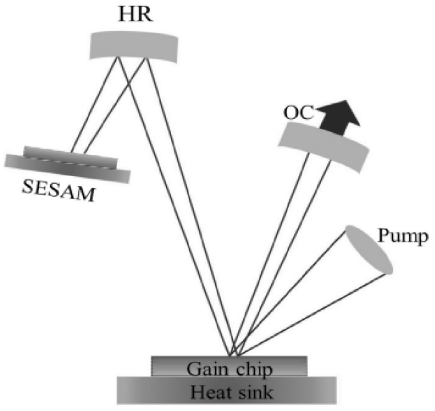

Fig. 30. Z-shaped VECSEL cavity for SESAM modelocking.

3.1.6 MECSELs vs VECSELs

The DBR in VECSELs adds significant effort to the growth time and complexity and in addition limits the thermal performance, due to the material thickness and the many semiconductor interfaces, introducing high thermal resistance. In contrast, recently introduced DBR-free SDL technology offers a potential solution to these limitations. DBR- free SDLs on diamond, emitting 6W CW output power at 1055 nm have been demonstrated. There, a 2.4 μm thick active region was used, consisting of 8 InGaAs quantum wells emitting at 1160 nm and forming a resonant periodic gain structure inside the strain compensation GaAsP barrier with InGaP window layers (Figure 31).

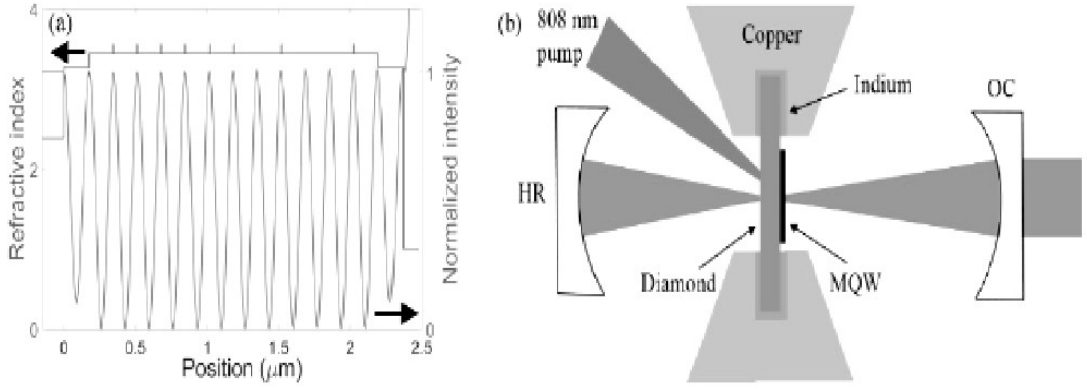

Fig. 31. Sample design and diagram of laser cavity geometry (modified from [112]).

Also, that study reported 78 nm tuning range at 10.5 W pump power using 0.5 mm thick quartz birefringent filter. Using thermal modeling results, authors there suggested that thermal management in double-diamond transmission geometry could be very advantageous in comparison to thermal management strategies used for VECSELs so far. This sandwiched DBR-free active region design using AlGaInP system was successfully experimentally realized, and output power of 595 mW at wavelength of 657 nm was demonstrated. The semiconductor membrane external-cavity surface-emitting laser being realized was called MECSEL. There, gain membrane was MOVPE grown on GaAs substrate followed by 200 nm AlAs substrate acting as sacrificial layer for further etching process. The etching process there contain two steps – etching using ammonium hydroxide solution $NH_4OH:H_2O_2$ in a relative concentration of 1:3 in order to etch away the GaAs substrate, followed by AlAs layer removing by dipping the sample into hydrofluoric acid - $HF:H_2O$ in relative concentration of 1: 9. The gain region there consisted of 20 compressively strained GaInP quantum wells with

thicknesses of 5 nm and distances of 4 nm arranged in five packages with each package being placed at the antinode of the simulated electrical standing wave to depict the typical resonant periodic gain structure (Figure 32).

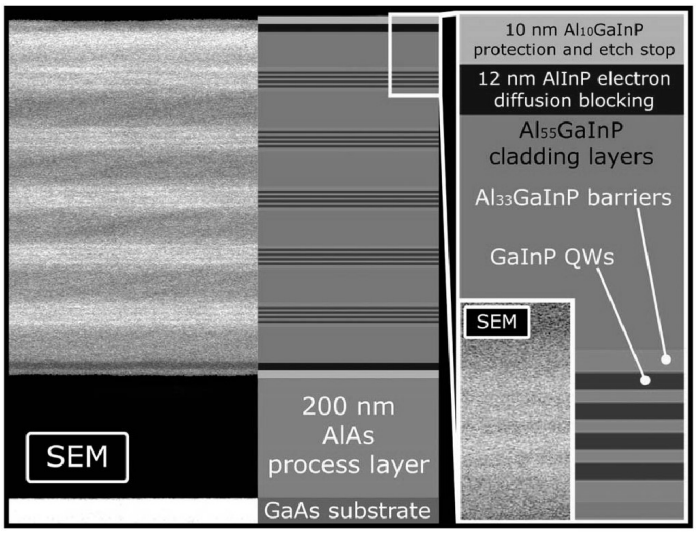

Fig. 32 (modified from [113]) Left part of this figure shows a SEM picture with enhanced contrast settings of the unprocessed membrane sample alongside the corresponding scheme. A magnified cutout of the outer layers and a quantum-well package is plotted on the right-hand side with a SEM picture of one quantum-well package.

The characterization of gain membrane there was performed using SEM and optical microscope. Wavelength tuning around 660 nm with tuning range of 23.7 nm was also demonstrated.

3.1.7. Introduction summary

VECSELs nowadays attract significant attention due to ability to provide high output power with a good beam quality over a range of wavelength from visible to mid-infrared and capability of producing sub-100-fs pulses, multi-kW peak powers, with demonstrated mode-locking for wavelength range from 675nm to >2 μm. One of the most challenging aspects of VECSELs is the incorporation of heat into the active region, leading to strong temperature-dependent performance. In contrast recently introduced Distributed Bragg Reflector (DBR) free technology helps to address these challenges. DBR free VECSEL geometry allows employing efficient thermal management strategies and direct cooling of active region avoiding thick DBR layers with poor thermal conductivity. In addition, DBR free geometry allows to employ larger range of semiconductor structures, removing DBR to substrate and gain medium to DBR lattice-matching requirement.

3.2 IR MECSEL

3.2.1 MECSEL design and growth

The IR membrane VECSEL structure used in this thesis was jointly designed by VECSEL group at the University of Dundee and University of Stuttgart while being MOVPE grown at the University of Stuttgart, IHFG. The first experiments designed to test this InGaAS-based MECSEL were performed during 3 month secondment at University of Stuttgart and continued afterwards at University of Dundee.

The DBR-free semiconductor gain membrane sample that has been used further to produce gain membrane via chemical etching is fabricated by metal-organic vapor-phase epitaxy (MOVPE) in a 3×2" close coupled showerhead reactor. On a GaAs substrate misoriented 6° toward the $[111]_A$ direction, a 200 nm AlAs sacrificial layer was deposited before starting the growth of the actual gain membrane. This active region with a thickness of 1574 nm includes ×10 $In_{0.13}GaAs$ quantum wells that are embedded in strain compensating $GaAsP_{0.06}$ barrier layers. GaAs spacer layers are used to position the single quantum wells in the antinodes of the electric field, resulting in a resonant periodic gain structure. On both sides of this active region, GaInP cladding layers are deposited to prevent oxidation and also act as stop layers for the selective etching process of the AlAs sacrificial layer. A scheme illustrating layer structure of this gain membrane is shown on Figure 33.

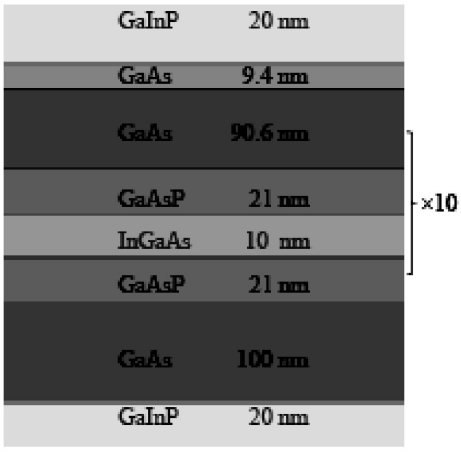

Fig. 33. Layer structure of MOVPE grown InGaAS-based DBR-free IR VECSEL gain membrane

3.2.2 Etching

The etching mechanisms could be separated on two types: physical etching, also called as sputter etch since it based on particles that are hitting and eroding the surface, and wet or dry chemical etching. Etching could occur in both horizontal and vertical directions depending on etching materials and methods used. The rate of material removal is described by etching rate. Physical dry etching uses high kinetic energy (ion, electron, or photon) beams to etch off the substrate atoms, while wet etching removes material using liquid chemicals or etchants. Most of the etchants contain oxidizing agent, solvent and agent for dissolving the oxides forming during the etching process. Typical oxidizing agents in this case are for example H_2O_2 and HNO_3, with water acting as a solvent and various acids for dissolving the oxides, such as HF, HCL, NH_4OH and citric acid.

Etching used in this thesis was performed using wet chemical etching processes for both MECSEL (continually stirring the sample in an ammonium hydroxide solution at a ratio of $NH_4OH:H_2O_2$, 1 : 2 for the GaAs substrate removal) and membrane SESAM (lateral etching using HF).

The etching process that will be described below is based on the successful etching of the red MECSEL [125]. For the etching process it is critical that the surface becomes smooth on sub-micron scale in order to achieve further a good bonding to the heat spreaders such as Si carbide or diamonds. This therefore requires a highly selective etching process. In a process described below, H_2O_2 acts as an oxidizing agent and NH_4OH then dissolve the oxidized layer. The latter is then being removed from the sample surface by rotating liquid, that washing away a dissolving layer mechanically.

In order to prepare samples for etching, roughly 5×5 mm^2 pieces where cleaved out of the wafer and slicked to a silicon carrier wafer using Crystalbond. The whole preparation and further etching process could be described as follows:

1) Both sides of unprocessed IR MECSEL pieces were at first cleaned with acetone and then isopropanol, and let dry.

2) Small amount of crystalbond was placed on surface of cleaned Si piece, that was used for holding unprocessed IR MECSEL, then Si part was heated up to 90-100 ^oC. When crystalbond melts, unprocessed IR MECSEL piece was placed on Si piece (substrate side up), directly on melted crystal bound droplet using tweezers, then by

circular motion of the tweezers, melted crystalbond was uniformly distributed over the Si surface, exceeding a bit area of IR MECSEL piece. If too much crystal bound used, it normally took significantly longer time to release membrane in acetone after processing and also could result on non-uniform etching of the sides of the sample.

3) Sample was left for few minutes to ensure crystalbond solidification and cooling down of the Si piece with embedded IR MECSEL chip to room temperature.

4) Preparing of etching solution: etching solution being used was NH_4OH (25%) and H_2O_2 (30%) in ratio of 1:2. A 20 ml of NH_4OH (25%) and 40 ml of H_2O_2 (30%) were mixed directly into one glass beaker. Beaker was cleaned before with acetone and propanol and dried, avoiding any dust or dirt as much as possible. Beaker with solution was placed on magnetic stirrer, where it was mixed continuously at room temperature using magnetic stirrer for 1-2 minutes.

5) Metallic holding clamps were used to fix Si with mounted IR MECSEL chip and deep IR MECSEL chip in steering solution. Chip was placed perpendicular to the flow in solution (Figure 34). It was possible to observe removal of the oxidized layers during etching. IR MECSEL chip therefore was moved within steering solution with respect to the flow to improve layers removing.

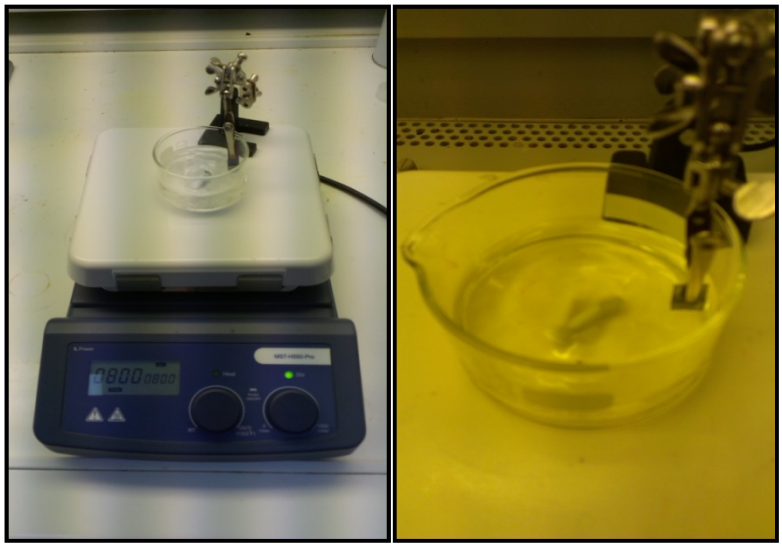

Fig. 34. Etching of IR MECSEL gain membrane in a rotating NH_4OH-H_2O_2 solution. Way to hold sample within etching solution also shown.

6) For the particular chosen IR MECSEL sample size, solution, and concentration it usually took about 50 minutes to remove all the substrate layers. After last layers of substrate etched away, sample gets metallic silver shine, and sample was removed from solution immediately. It was found out that by heating the solution up to 40 C, etching time will decrease from 50 min. to about 35 min, but surface quality remains the same. However, most of etching done was at room temperature. For few of the samples, an additional step was done: after about 40 minutes in 1:2 solution, the solution was replaced with 1:30 solution (same NH_4OH (25%) and H_2O_2 (30%) were used, this concentration effectively acts as a final polishing step since in this concentration the etching rate decreases by about three orders of magnitude, as reported in [140] and etched further for 20 min. This sometimes results in better surface quality observed by SEM. However, some samples after just 1:2 concentration demonstrated similar surface quality. This etching solution etched AlAs sacrificial layer as well as GaAs substrate completely and stops selectively on following GaInP layer.

Once etching was completed, the IR MECSEL chip was washed with distilled water and then dried for a few minutes.

8) The etched sample then was placed into acetone to release the gain membrane from crystalbond. It normally takes 30 minutes to few hours to dissolve crystalbond and release the membrane.

9) After membrane release, Si piece removed from acetone, and then acetone replaced with isopropanol.

10) Membrane was «fished» from the solution on cleaned round-shaped 8 mm diameter, 350 μm thick SiC heat spreader, with another SiC was placed on top. This sandwiched gain membrane was further placed into the specially designed sampleholder and then to laser cavity. The described etching procedure could potentially be translated to manufacturing, allowing to produce hundred to thousand membranes within one etching step. However, to do it with high reproducibility and reliability, the concentration of the etching solution compounds should be precisely controlled, as well as etching time, rotation speed, sample size and its position within the etching solution. The design of the sample holder used for first experiments with IR MECSEL was done

at IHFG, University of Stuttgart. The designs of sampleholders used and laser characterization will be described at following chapters of this thesis.

To characterize the surface quality of the obtained IR MECSEL membrane, both optical microscopy for the previously sandwiched gain membrane in a sample holder, and SEM for characterization of thickness and surface quality of the sample were used.

An example of SEM image of the typical gain membrane surface obtained is shown on a Figure 35.

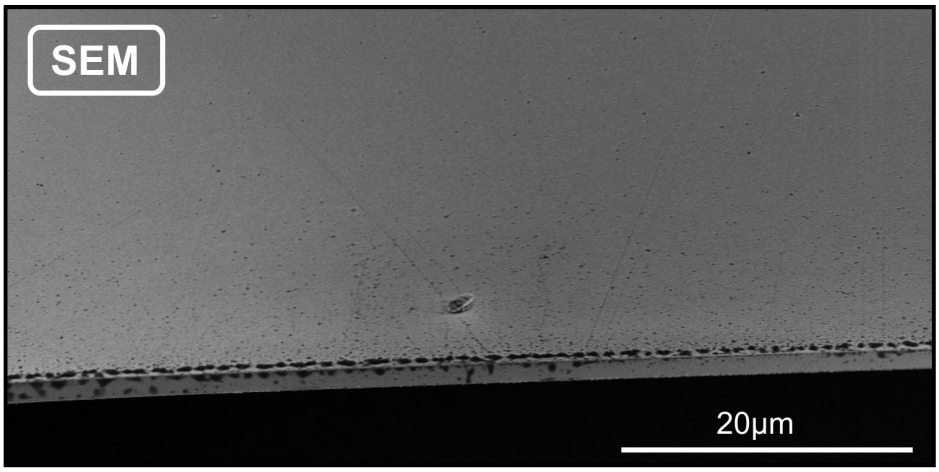

Fig. 35. SEM image: processed surface of IR MECSEL gain membrane. (University of Stuttgart, IHFG)

A final thickness check of the gain membrane after etching was performed, also being done using SEM. SEM images of the final structure are shown in Figure 36.

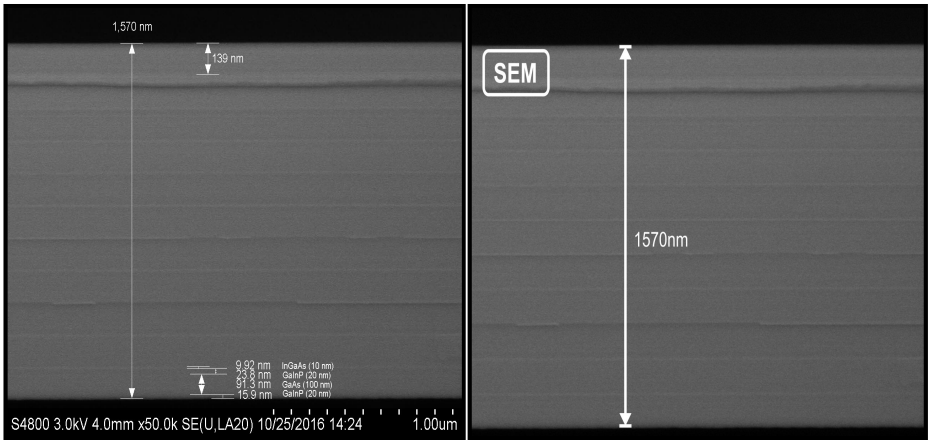

Fig. 36. SEM image of IR MECSEL gain membrane, demonstrating total structure thickness of 1570 nm. Quantum wells could be observed as appearing lighter stripes on structure (University of Stuttgart).

The quantum wells could be seen (lighter stripes on a structure). The total thickness of the IR gain membrane is measured to be 1570 nm. The surface quality of some other etched IR MECSEL membranes was also checked using SEM. An etching protocol that includes NH_4OH (25%) : H_2O_2 (30%) etching in ratio 1:2 as a first step and final polishing step of the same etching reagents in various concentrations from 1:20 to 1:100 and etching time from 10 to about 30 minutes generally provides sufficient surface quality to allow uniform bonding of the gain membrane to SiC or diamond heat spreaders provided that the heat spreaders are polished and surface of the membrane is not curved or damaged. A typical SEM image of IR MECSEL gain membrane after NH_4OH (25%) : H_2O_2 (30%) etching in ratio 1:2 followed by 1:100 polishing finalizing etching is shown on a Figure 37.

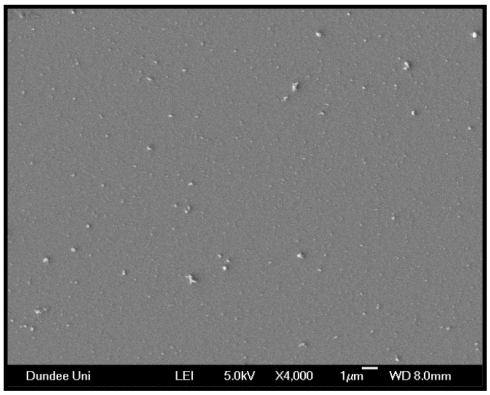

Fig. 37. Representative SEM image of IR MECSEL gain membrane at ×4000 magnification after being etched and bonded to SiC heat spreader. Beads of ither dust or AlAs sacrificial layer could be seen. (University of Dundee).

A first set of experiments aimed at testing IR MECSEL membrane in laser cavity was done using gain membrane sandwiched between SiC heat spreaders and placed into specially designed brass mount (design and fabrication of this mount was done at IHFG, University of Stuttgart). When the membrane was sandwiched and mounted, it was checked using conventional optical microscope. It allows to localize areas with not uniform bonding of the membrane to one or both SiC surfaces and also to check whether or not the membrane was damaged during sandwiching and placing onto the mount. Examples of such microscope images are presented in Figure 38.

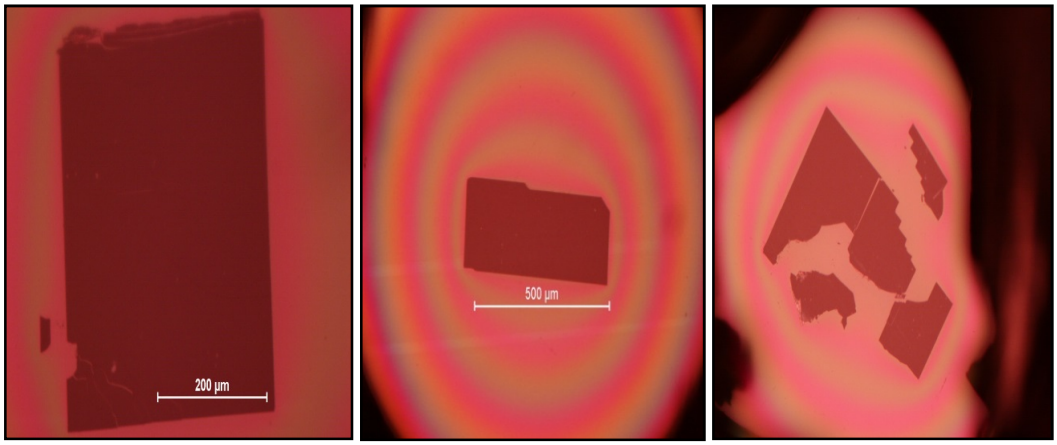

Fig. 38. Representative optical microscope images of IR MECSEL gain membranes sandwiched between two SiC discs and mounted to brass mount. First two membranes from left to right were used for experiments, while third case shows typical damage of membrane caused by relative tilt of SiC disc heat spreaders during the mounting and sandwiching process.

In order to avoid cracking of the membrane during sandwiching, released gain membrane piece was fished from isopropanol using one SiC disc, and then second SiC disc placed on top of the gain membrane just before isopropanol dry completely from the membrane and SiC surface. Brass mount has specially designed guiding pins to avoid shifts and tilts of SiC discs with respect to each other during mounting process.

3.2.3 Mounting, handling and thermal management: route to higher power

After etching of the gain membrane was completed, and the IR MECSEL membrane released in acetone, a small piece of the membrane (typical size is ~1 mm^2) was caught with a silicon carbide 8 mm heat spreader disc. The second heat spreader is placed on top and the whole package is mechanically squeezed into a brass mount. Due to the applied pressure the contact between the membrane and the heat spreaders is improved.

The experiment aimed at testing laser performance is performed in a linear concentric resonator (Figure 39) with resonator mirrors that can be adjusted in all degrees of freedom. In addition, the sample holder can be shifted and tilted in two axes.

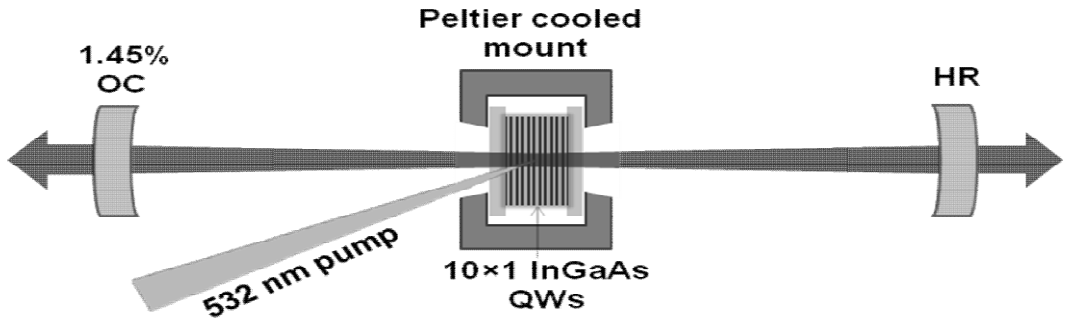

Fig. 39. IR MECSEL laser setup with gain membrane sandwiched between two SiC discs mounted on peltier cooled brass mount.

The gain membrane was pumped by a 532 nm 5W-Finesse pump diode laser under an angle of 15° to the gain membrane surface. For the output power measurements an output coupling mirror with reflectivity of R = 98.55% and a radius of curvature 50mm and a high reflector mirror (r =100 mm) where used. The cavity length was aligned to be 149,6mm that corresponds to a mode diameter of 45 μm at the beam waist where the brass mount containing the membrane has been situated. The diameter of pump spot on the gain membrane was ~75 μm. The temperature of heat sink was set to 10 °C. A photo illustrating a described setup and operating IR MECSEL is shown on a Figure 40.

Fig. 40. A photo showing IR MECSEL operating in linear concentric cavity at 990 nm while pumped by 532 nm diode laser. (University of Stuttgart)

For the sandwiched IR MECSEL gain membrane, reflectivity and transmission measurements done using a 532 nm pump diode, recorded at 23.1% of power being reflected and 0.2% of pump power transmitted through gain membrane mounted between two 350µm thick SiC heat spreaders. A graph illustrating these measurements is shown on Figure 41.

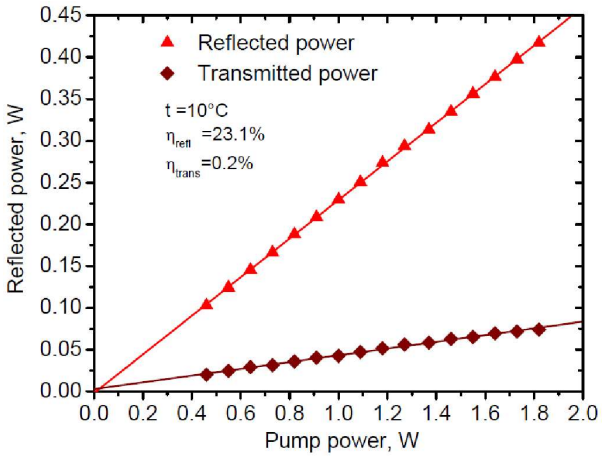

Fig. 41. Transmission and reflectivity measurements for IR MECSEL gain membrane sandwiched between two SiC heat spreaders, mounted in brass mount and pumped by 532 nm pump diode.

Keeping heat sink temperature at 10° and using 1.45% output coupling mirror, the output power measurements for the operating laser in a concentric resonator were done. (Figure 42).

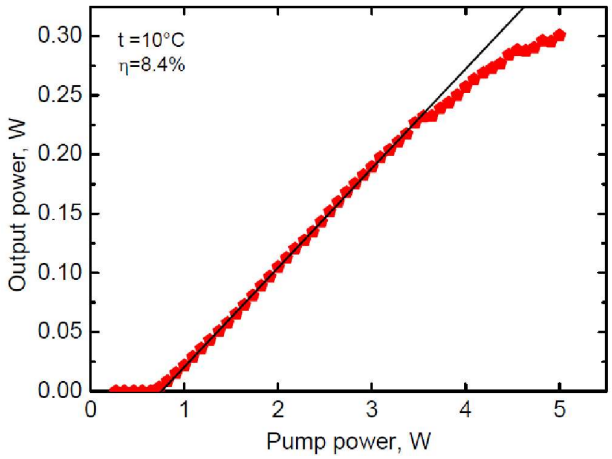

Fig. 42. Power characteristics of the IR MECSEL at a heatsink temperature set to 10°.

Over a wide a range of input power a linear behavior with a slope efficiency of 8.4% has been observed. The laser threshold was at 0.75 W. Above 3.5W of input power the parameters deviate from the linear behavior due to the observed thermal rollover. The maximum output power that has been obtained was measured to be ~0.3W.

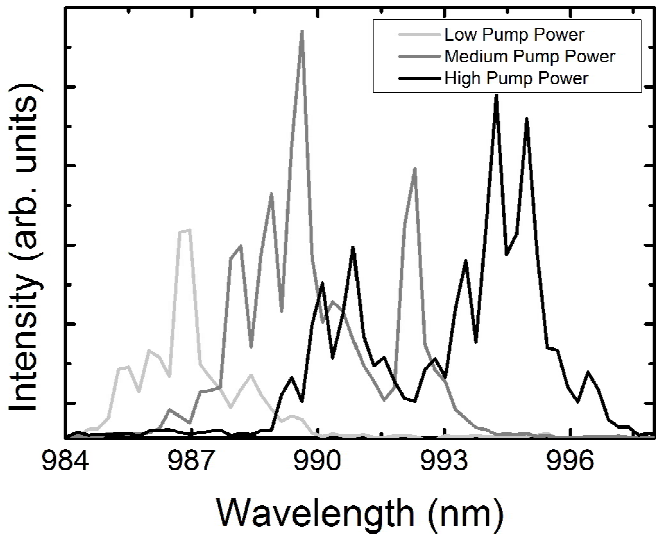

Fig. 43. Spectra of free-running IR MECSEL laser emission for different pump power (1.3W, 2.9W, 4.9 W) revealing a shift towards longer wavelengths due to heat incorporation.

The laser wavelength is ~990 nm and has a full width half maximum spectral width of approximately 1 nm at low pump power, which broadens with increasing pump power to ~6 nm at high pump power which is hown on Figure 43. With increasing of incident power the laser emission shifts roughly 6 nm towards longer wavelengths. This could happen due to the heat flow out of the system that is hampered by a moderate thermal resistance between the Peltier element and the gain membrane. The spectra reveal Fabry-Perot oscillations which cannot be resolved with the USB spectrometer that has been used. Additionally an envelope can be identified for higher powers that results from slightly different thicknesses of the heat spreaders. The performance of the IR MECSEL has been further improved by pumping at higher wavelength (808 nm) to maximize the quantum efficiency, by increasing the pump area using ~230 μm pump spot size on gain membrane and also using new mount design to improve heat removal.

To test IR MECSEL performance using 808 nm pumping, the setup shown on a Figure 38 has been used. Gain membrane was etched using wet chemical etching process described above, and placed in a linear concentric resonator formed by 1.45% output coupling mirror on one side and high reflector mirror on another side. In this case, after sandwiched membrane was placed into the brass mount, the whole mount then was glued to water cooled copper block as shown in Figure 44. In this case, 808 nm DILAS laser diode was used to pump the gain membrane.

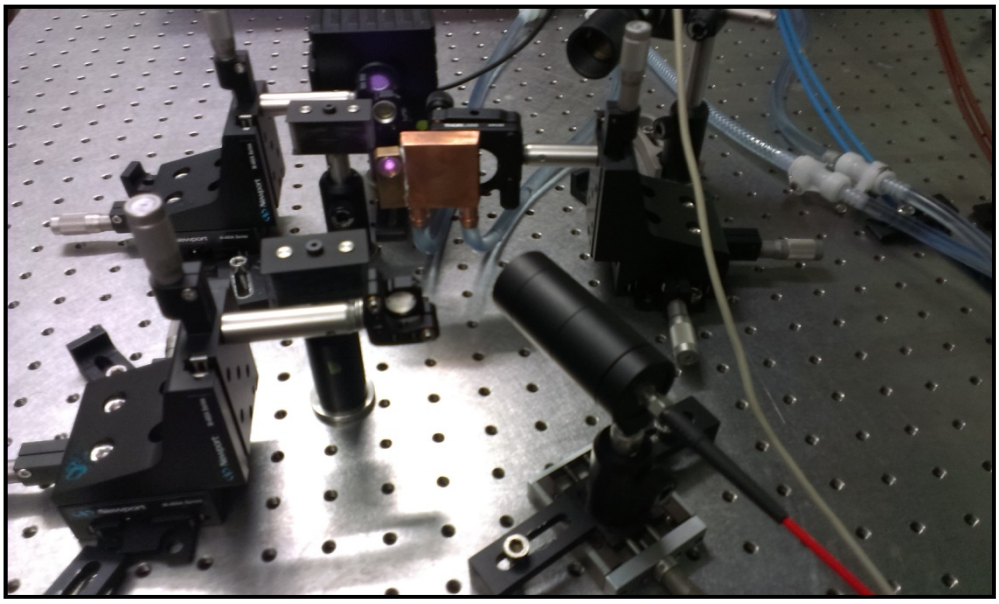

Fig. 44. Setup showing 808 nm pumped IR MECSEL gain membrane being sandwiched between two SiC heat spreaders and stuck to copper water cooling block using thermal paste.

To test laser characteristics, output power measurements were performed and laser spectrum was obtained. In this case, the pump spot size on a membrane was measured to be ~230 µm. Sample was pumped under an angle of 20° to the gain membrane surface. Heat sink temperature was 15° C. Measured pump power-output power curve is shown in Figure 45.

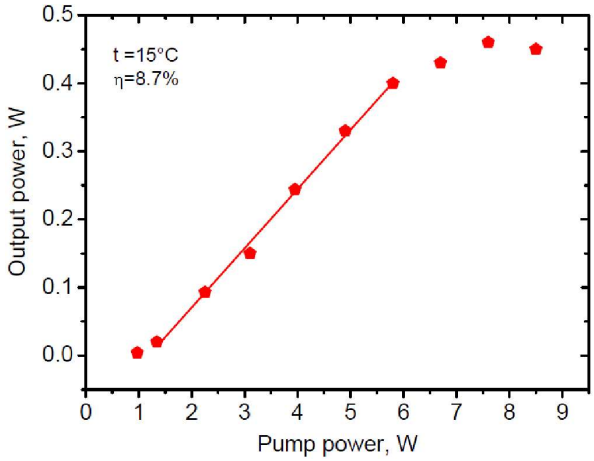

Fig. 45. Setup showing 808 nm pumped IR MECSEL gain membrane being sandwiched between two SiC heat spreaders and sticked to copper water cooling block using thermal paste.

Over the linear range, where there is no deviation from linear behavior due to the thermal roll over observed, the slope efficiency was ~8.7%. Maximum output power obtained was ~460 mW. The laser wavelength was measured to be ~1007 nm which could be seen from spectrum, taken at 2.25 W of pump power and shown on a Figure 46.

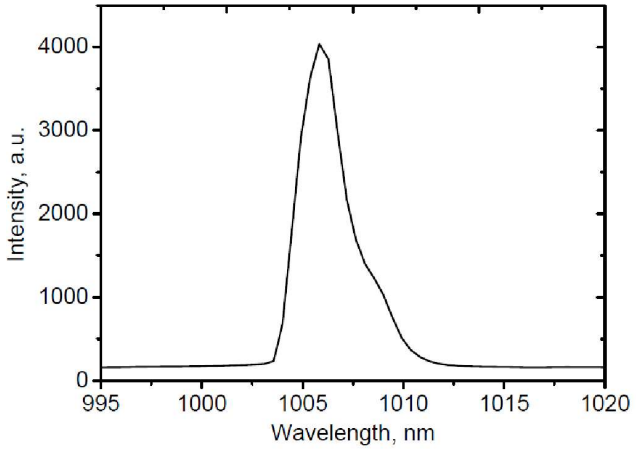

Fig. 46. Spectrum of 808 nm pumped operating IR MECSEL

Even for an excellent and uniform bonding between the heat spreaders and the membrane the contact between the heat spreaders and the brass mount is a bottleneck for the heat flow due to the small contact area. Moreover, the heat has to pass a screw thread that further reduces the heat flow. In order to overcome this problem, the new design of the mount was done and optimal output coupling efficiency for this laser was studied. The high power CW operation of IR MECSEL will be described in next chapter of this thesis.

3.2.4 High power CW MECSEL

To overcome thermal management problems described above, a new sample holder mount has been designed, allowing bonding the gain membrane to only one SiC heat spreader. The mount consists of two copper block parts with jaws allowing to fix SiC piece in and orifice to pass the pump beam through. Indium foil spacer was used between two parts of the sample holder to allow better heat contact between the copper blocks, and either silver or indium foil used for the both sides of the jaws where SiC with bonded membrane being placed. The schematics of the assembled sample holder with SiC heat spreader and gain membrane on it is shown on a Figure 47 together with a photo showing an actual sample holder being used. The copper mount was cooled using water-cooling system and the temperature of the water was controlled by the circulating chiller.

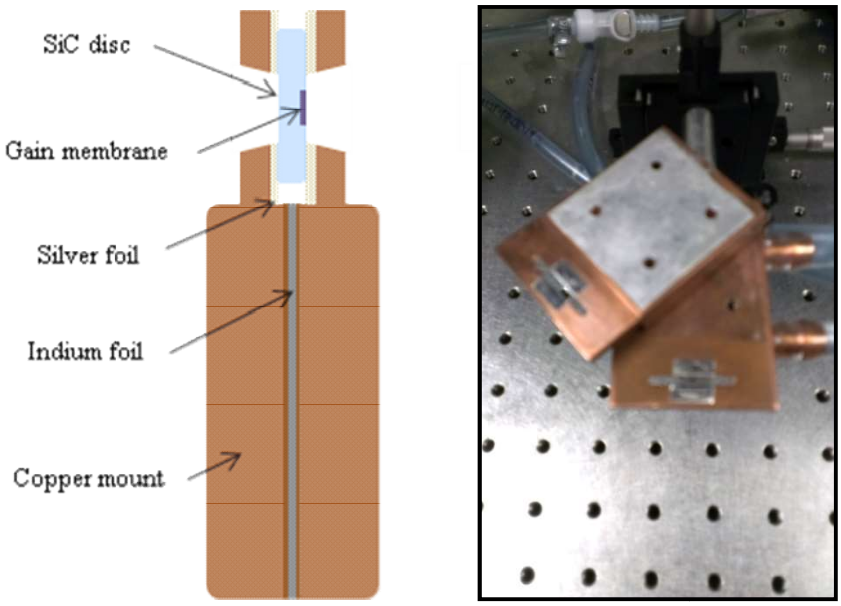

Fig. 47. A schematics of copper sample holder being used in experiments where membrane was bonded to one SiC heat spreader and a photo of an actual mount.

The single SiC heat spreader disc was used to fish the membrane piece from the acetone solution, and left for 15-30 minutes to dry in order to obtain uniform bonding of the gain membrane to the SiC surface. The quality of the bonding generally depends on the surface quality of the SiC and absence of any dirt on its surface, therefore SiC undergoes cleaning using acetone and propanol before proceeding to the actual bonding process. The attachment of the gain membrane to the surface also requires smooth

surface of the membrane and absence of significantly curved or cracked bits of the membrane. The etching process used was again two steps wet chemical etching with first etching step of NH_4OH (25%) and H_2O_2 (30%) solution in a ratio 1:2 for about 70 minutes followed by surface polishing step using same solution but with relative concentration of the etching agents of 1:20 for roughly 10 minutes. This etching protocol generally results in good surface quality of the final etched gain membrane. Surface quality of the etched gain membrane bonded with crystalbond to the silica piece, used as a mount for etching in rotating etching solution, was assessed using optical microscope at ×5 magnification. A microscope images of typical membrane surface quality obtained is shown in Figure 48.

Fig. 48 Optical microscope images (×5 magnification) of the typical etched IR MECSEL membrane surface. Both membrane area far from the edge (left) and edge of the membrane (right) are shown.

The overall size of the etched membrane, shown on Figure 48 was ~5×3 mm. While most of the membrane was good enough to allow good Van der Waals bonding, actual bonding as described also largely depends on particular bit of the membrane used and fished from acetone or isopropanol after crystal bond is dissolved in acetone, and silica piece removed from acetone to allow breaking of the released membrane into pieces using pipette with acetone. Most commonly, best performance achieved in this study was given by uniformly bonded square pieces of membrane of about 0.5×0.5 mm in size and with smooth membrane surface that allows use ~230 μm pump spot to pump areas of the membrane without significant defects as seen by optical microscope or focusing CCD camera on sample surface.

Also, membrane pieces with non-uniformly etched edges should be avoided by either cleaving the edges of the membrane or cracking them from the rest of the membrane while released membrane is floating in acetone.

Depending on the size and shape of the gain membrane pieces that been fished to SiC heat spreader, bonding may vary a lot. Representative images illustrating different quality of membrane bonding to SiC surface are shown on a Figure 49.

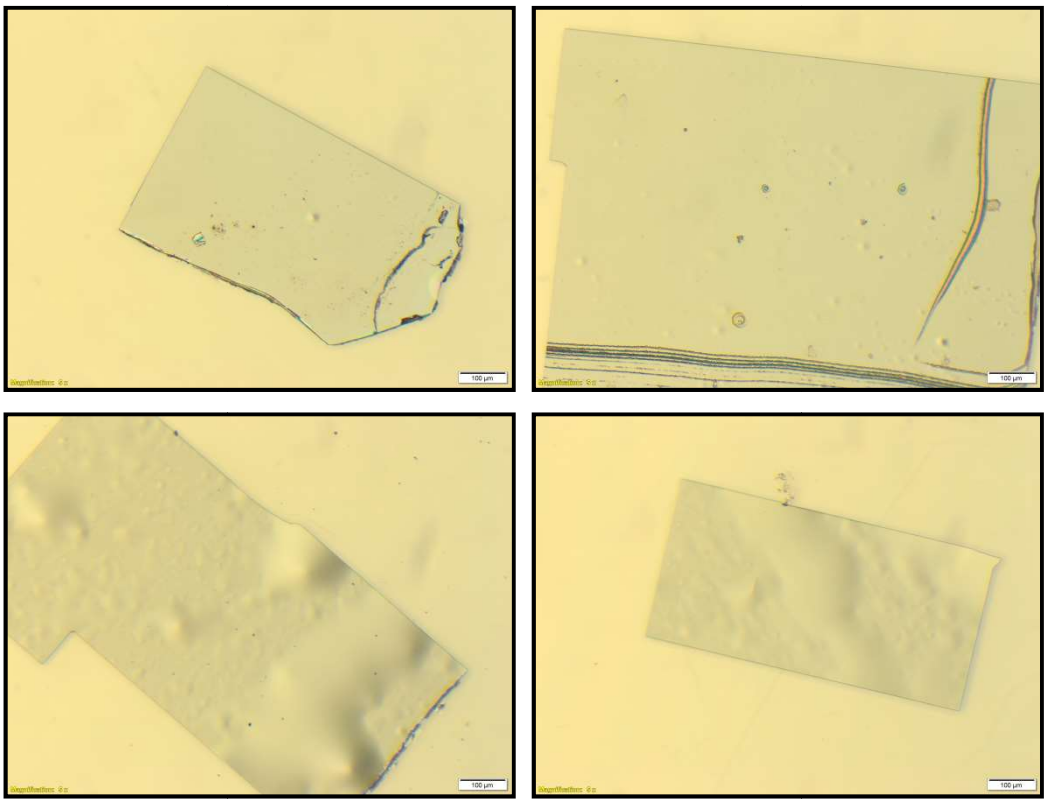

Fig. 49. Different bonding quality of gain membrane to one SiC heat spreader.

Top two images representing the bonding resulting at output power in a range of 3-6 W and high slope efficiency, whereas bonding similar to bottom two images generally giving either output power in a range 1-2 W, or resulting at thermal damage of the membrane at pump power levels of around 2-3 W.

Once membrane was bonded to SiC heat spreader, it was then placed into copper mount that afterwards was glued to a water-cooled copper block using thermal paste and some superglue. The whole mount then was placed in to a linear concentric resonator as shown on Figure 50 with resonator mirrors that can be adjusted, and the sample holder can be shifted and tilted in three axis. Total cavity length was ~150 mm.

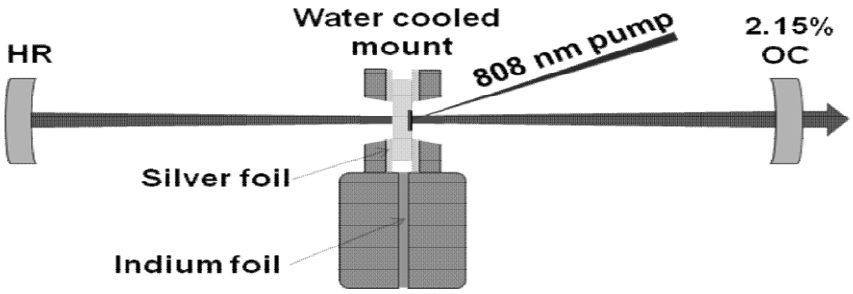

Fig. 50. Gain membrane mounted on sample holder that attached to copper water cooling block and placed into linear concentric resonator.

Both silver foil and indium foil of various thickness was tested on the jaws to allow better thermal contact of SiC heat spreader and water-cooled copper mount. In these studies, silver foil generally provides significantly better heat removal resulting in high output power and slope efficiency in comparison to indium foil. The studies aimed at comparing of indium and silver foil efficiency was done for the same membrane mounted on copper mount using both silver and indium foil on jaws of sample holder. Resulting output power curves are shown on a Figure 51.

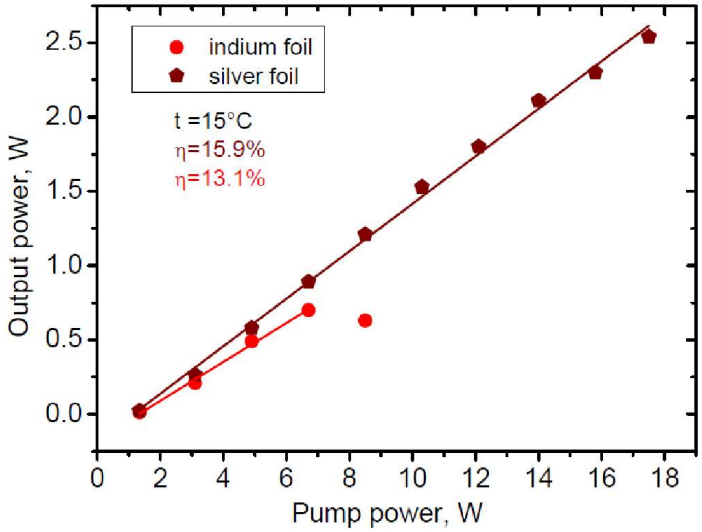

Fig. 51. Output power curves for IR MECSEL with gain membrane mounted using silver foil and indium foil as a spacer between copper mount jaws and SiC heat spreader.

For an average performance gain membrane, same membrane on SiC demonstrate slope efficiency of 15.9% with no sign of thermal rollover observed for pump power up to 18 W using silver foil spacer, whereas for indium foil spacer 13.1% slope efficiency was obtained with thermal rollover appearing from 7 W of pump power. As being mentioned previously, best performance of IR MECSEL obtained in this studies was

observed using silver foil spacer. However, the data demonstrated in Figure 43 could not be sufficient enough and only serve as an example since it is quite challenging to account for the squeezing of both silver and indium foil and amount of pressure applied each time during screwing both parts of copper mounts together. Also, silver and indium foil has different thickness. However, in both cases squeezing of the foils was achieved that was demonstrated by easy seen tracks from SiC heat spreader on the foil. Also, the jaws of the mount should be parallel with very high precision since any deviation from parallel arrangement of the jaws results on breaking SiC heat spreader or on non-uniform squeezing of the foil by SiC which limits thermal contact and results on worth performance of the laser.

To get the optimal output coupling efficiency for the IR MECSEL, a set of output couplers was studied. The data representing optimal output coupling efficiency is shown on a Figure 52.

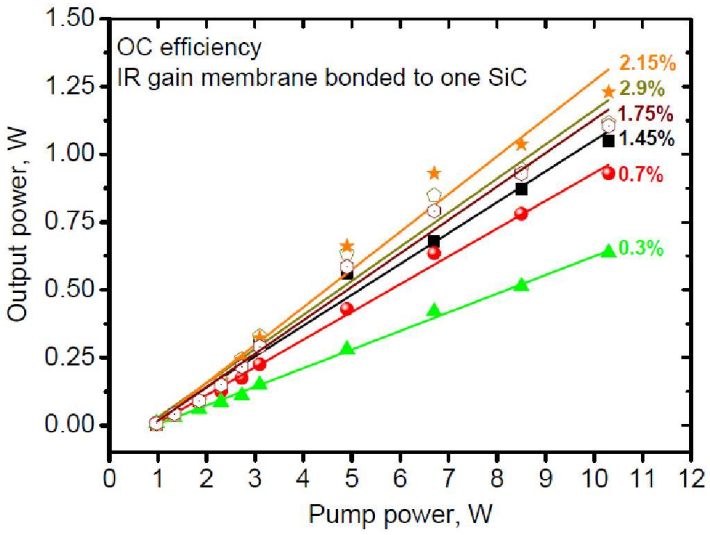

Fig. 52. Output coupling efficiency for IR MECSEL

For the range of output coupling mirrors used output coupling in a range 2.15% - 2.9% seem to be optimal for this particular laser. For further high output power experiments, a 2.15% output coupling was used. The good bonded-to-8mm SiC heat spreader-IR-gain-membrane was mounted to copper mount with indium spacer between the copper blocks and with ~5×4 mm silver foil pieces as spacer between jaws of copper mount and SiC heat spreader. Gain membrane was then pumped using 808 nm DILAS diode laser under an angle of 20° to membrane surface on linear concentric resonator

with total cavity length of ~150mm. The pump spot size on membrane surface measured to be ~230 µm.

Measurements were done while keeping heat sink temperature at 15 °C. The photo of IR MECSEL operating in described setup is shown in Figure 53.

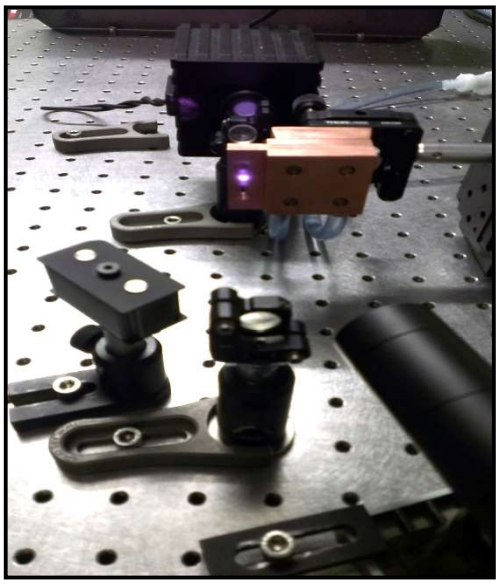

Fig. 53. IR MECSEL operating in linear concentric resonator pumped by 808 nm diode laser.

Transmitted and reflected light measurements while membrane being pumped at 808 nm with 3.1 W of pump power resulted at 0.156 W of power transmitted through the membrane bonded to one SiC heat spreader and 0.252 W of power being reflected. In this case as before, the SiC side containing bonded membrane being pumped.

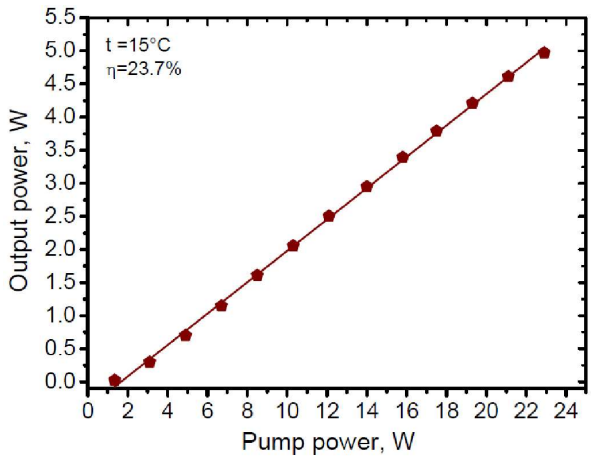

Fig. 54. Output power vs pump power curve for IR MECSEL. Membrane bonded to one SiC. Gain membrane size ~800x600µm. At 15 °C, maximum slope efficiency obtained for this structure in this study was 23.7%

For the gain membrane structure discussed in 3.2.1, maximum slope efficiency while the laser operating at 15 °C was 23.7% with maximum output power of ~5W. 2.15% output coupler was used and pump spot size on the membrane was ~230 µm. The resulting output power curve is shown on a Figure 54. Further output power curves were recorded at heat sink temperatures of 12 °C and -10 °C with incident pump power up to 40 W and are shown in Figure 55.

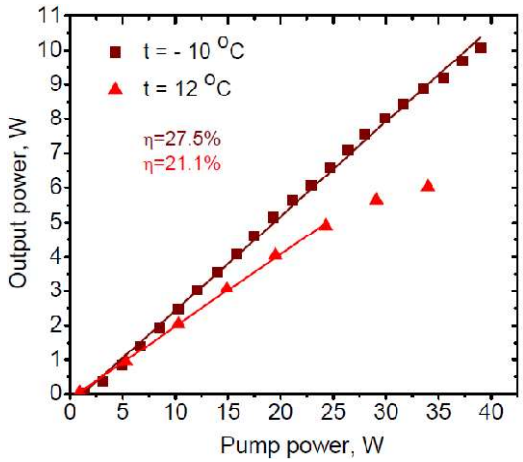

Fig. 55. Output power vs pump power curve for IR MECSEL. Membrane bonded to one SiC. Gain membrane size ~800x600µm. At -10 °C, maximum slope efficiency obtained for this structure in this study was 27.5%

At 12 °C heat sink temperature thermal roll-over of the output power can be seen and a maximum power of 6 W was achieved. When the heat sink temperature was reduced to -10 °C no evidence of thermal rollover was observed up to 10.1 W output power at 40 W pump power which represented the pump power limit for the diode used.

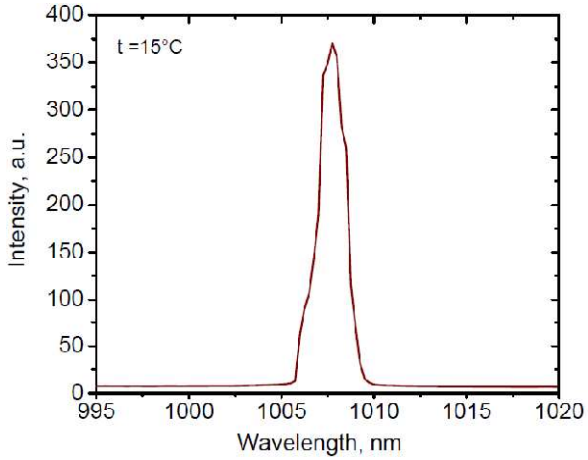

Fig. 56. Representative optical spectrum of DBR-free Semiconductor Disc Laser taken at 15°heat sink temperature and 5 W output power

The slope efficiency of the laser was 21.1% and 27.5% at heat sink temperatures of 12 °C and -10 °C respectively. A representative optical spectrum of the laser, taken at a heat sink temperature of 15° and 5 W output power is shown in Figure 56.

3.2.5 Wavelength tuning

Wavelength tuning experiments where done in linear concentric resonator with total cavity length of ~150 mm and output coupling of 1.45%. Membrane was pumped at an angle of 20° to membrane surface by 808 nm diode laser with pump spot size on a membrane of ~230µm. The laser wavelength was tuned by rotating an uncoated 500-µm-thick quartz birefringent filter which was introduced into laser cavity at Brewster's angle as shown in Figure 57.

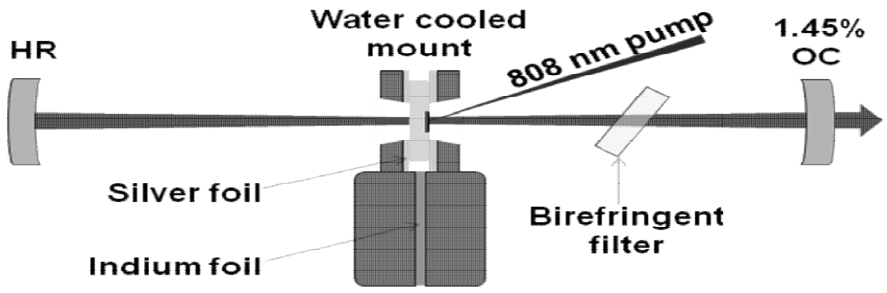

Fig. 57. IR MECSEL in a concentric linear resonator containing birefringent filter for wavelength tuning.

The wavelength tuning from 995 to 1020 nm was achieved, with a maximum power of 0.7 W under 3.1 W of pump power at a wavelength of 1007 nm and keeping heat sink temperature at 15°. The measured power and optical spectra for a range of operating wavelengths are shown in Figure 58.

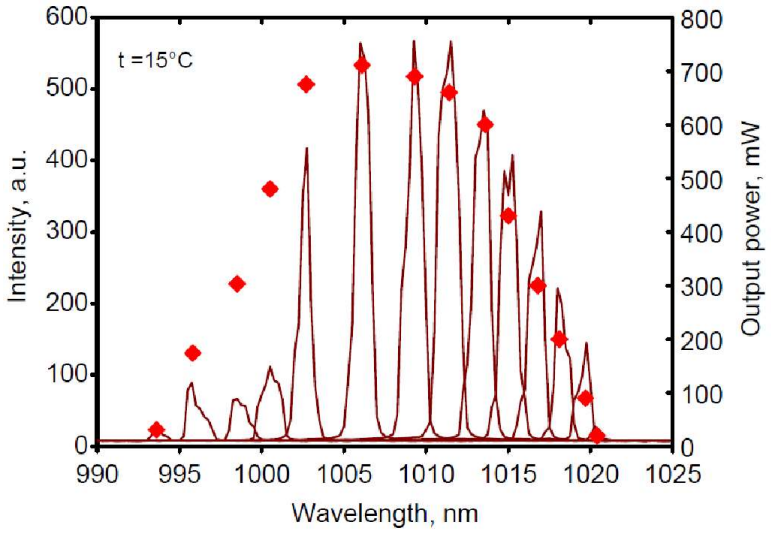

Fig. 58. IR MECSEL wavelength tuning using quartz birefringent.

3.2.6 Conclusions and Future prospects

A 10.1 W continuous wave output power from DBR-free SDL at 1007 nm at a heat sink temperature of -10 °C, with a 10 QW resonant periodic gain structure, van der Waals bonded to an 8 mm diameter, 300 μm thick SiC heat spreader was demonstrated. Laser slope efficiency of 21.1% and 27.5% at heat sink temperatures of 12 °C and -10 °C respectively were achieved. The laser wavelength of output laser beam could be tuned from 995 nm to 1020 nm by introducing 0.5 mm quartz birefringent filter into cavity. While SiC has a lower thermal conductivity than diamond, it is cheaper and more widely available, and its high surface quality allows for uniform and robust van der Waals bonding with low optical loss. The laser performance largely depends on heat removal from SiC and therefore on thermal contact of SiC and the jaws of copper heat spreader. Introducing the silver foil between SiC and copper heat sink improves heat contact but the reproducibility of the mounting of SiC to the copper mount is very low.

That could be improved by designing new copper heat sinks that allow cooling of SiC from both sides and highly-repeatable mounting process. To further improve IR MECSEL performance, wet chemical etching process can be improved to increase the surface quality and reproducibility. It can be done for example by introducing additional third etching step with low acid concentration or employing other etching solutions. Multiple heatspreaders, or «sandwiched» heatspreaders approach can further improve thermal management, provided that optical quality of SiC or diamond heatspreaders is high enough, and bonding is uniform. In-well multi-pass pumping can be another option for higher power MECSELs. In addition, to improve overall efficiency at higher power values, multiple-chip, multiple-heatspreader or slab configurations can be used.

4. Semiconductor saturable absorber membrane

4.1.1 Introduction to saturable absorbers

Mode-locking is the process of locking the phase between longitudinal modes of the laser to produce pulsed output. VECSELs could be made to operate in pulsed regime using active or passive mode-locking. Active mode-locking achieved by periodic modulation of the resonator losses or of the round-trip phase change using electro-optic and acousto-optic modulators. In active mode-locking, the modulator acts as periodic shutter that opens once per round-trip time of the pulse, providing predictable and controllable modulation. However, active mode-locking becomes ineffective for very short pulses - due to limited modulators response times, pulse durations that could be achieved using active mode-locking are in a range of nanoseconds. In contrast, passive mode-locking mechanism allows achieving significantly shorter pulses, where laser pulse itself used for switching of the modulator from high to low loss states, and loss modulation is automatically synchronized with the laser pulses. If response time of nonlinearity is fast enough, the modulation function gets faster as pulse gets shorter. Saturable absorber is effectively an optical absorbing medium where absorption decreases with intensity. Saturable absorbers could be divided on two types: fast and slow saturable absorbers. In fast saturable absorbers, recovery time is significantly shorter than the pulse duration. In slow saturable absorbers pulse duration is much shorter than the recovery time. Due to not instantaneous recovery of the real fast saturable absorber, the achieved pulse duration is formed as a result of the balance between total pulse shortering per round trip by absorber, and total broadening per round trip.

The analytical solutions for pulse duration and shape in case of fast saturable absorber, has been found by Haus [141], assuming parabolic frequency profile of the gain and absence of the dynamic gain saturation:

$$\frac{1}{\omega_L \tau_P} \approx \left(\frac{g_0}{1+\mathrm{q}} - 1\right) \frac{\mathrm{q}}{(1+\mathrm{q})} \frac{\mathrm{P_L}}{4\mathrm{P_A}} \omega_\mathrm{L} \mathrm{T_P} \qquad (19)$$

Where q is saturable absorber loss normalized to cavity loss, P_A and P_L are absorber and gain saturation powers, ω_L – laser bandwith, T_P – round trip time, and g_0 – small signal gain.

In case of slow saturable absorber, the pulse exceeds the gain. The pulse saturates an absorber upon arrival, and loss line drops below the gain resulting at pulse net amplification. Later gain starts to saturate and drops below the loss. Therefore, in this case gain saturation closes the window of net gain and allows formation of the stable pulse, and stable mode-locking could be achieved only provided that saturable absorber saturated faster than the gain. For the slow saturable absorber, it was shown [141] that net gain curve in energy domain could be approximated by parabola, and pulse duration could be calculated as:

$$\tau_P = \frac{f}{\Omega_g}\frac{1}{\sqrt{q}E_p} \qquad (20)$$

where E_P – pulse energy, and Ω_g – gain bandwith.

4.1.2 SESAM characterization

Mode-locking is the process of locking the phase between longitudinal modes of the laser, and could be realized actively or passively. Active mode-locking could be obtained by periodic modulation of the resonator losses or of the round-trip phase change using for example electro-optic and acousto-optic modulators. In active mode-locking, the modulator acts as periodic shutter that opens once per round-trip time of the pulse.

Passive mode-locking of VECSEL using SESAM has been for the first time demonstrated in 2000 [107], and since that time became key mode-locking technique used for VECSELs. SESAM in mode-locked VECSELs usually acts as external element, but could also be monolithically integrated into gain medium, resulting at Mode-locked Integrated External-Cavity Surface-Emitting Laser (MIXSEL) [142]. Typical SESAM formed by mirror structure and an integrated saturable absorber formed normally by either quantum wells or quantum dots. Semiconductors are well suited to act as saturable absorbers, allowing broad wavelength coverage and short recovery time. Design flexibility of SESAMs allows adjust the field propagation within the absorber section and optimize nonlinear macroscopic parameters. Key two macroscopic SESAM parameters are nonlinear optical reflectivity and saturable absorption temporal recovery. Semiconductor gain dynamic saturation combined with dynamic reflectivity change of SESAM is setting up a pulse formation in modelocked VECSEL. It could be illustrated on a Figure 59:

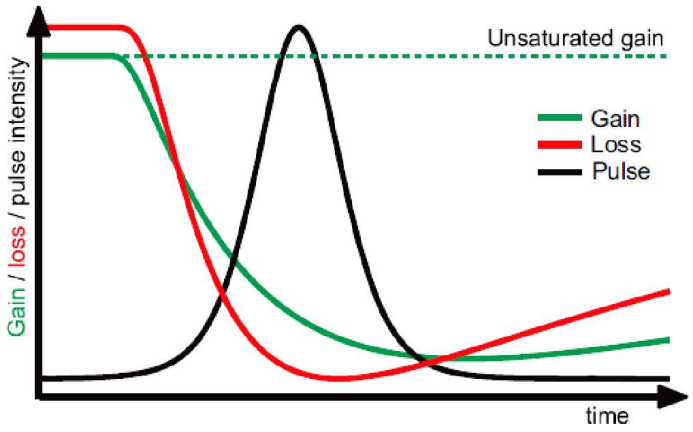

Fig. 59. An illustration of the basic pulse formation process in SESAM mode-locked VECSEL [from 85].

Losses in absorber (red curve) are reduced by incoming pulse (marked black), at lower energies in compare to saturation (green curve), which resulting at pulse amplification due to opening of the gain window. Following [134], the incident pulse fluence on the absorber could be written as:

$$F_p = \frac{E_p}{A_{abs}} \qquad (21)$$

Where F_p – incident pulse fluence, E_p – incident pulse energy, A_{abs} – $1/e^2$ intencity mode area of the Gaussian beam on the SESAM. Figure 60 illustrates the characteristic curve of the pulse fluence.

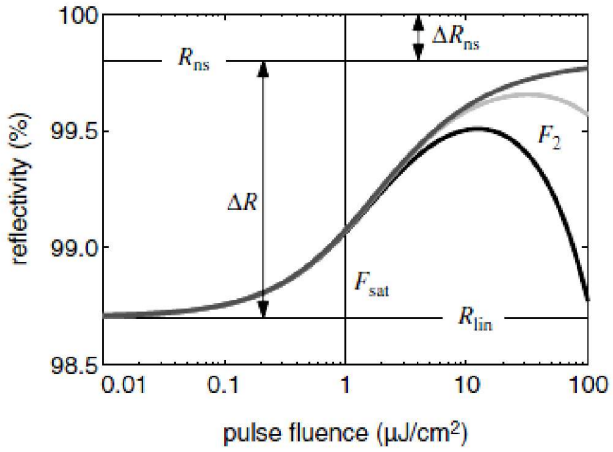

Fig. 60. Reflectivity as a function of the incident pulse fluence [134].

On the reflectivity curve, the difference in reflectivity of the completely saturated and not saturated SESAM is called saturation depth ΔR, nonsaturable losses caused by absorption or scattering are labeled ΔR_{ns} , and pulse fluence for which SESAM saturated is called saturation fluence F_{sat} . F_2 describes the induced absorption, which shows the fluence where due to the induced absorption reflectivity drops to 1/e. If nonsaturable loses and induced absorption at higher fluencies are taken into account, then nonlinear reflectivity could be written as:

$$R(f) = \frac{Ln[1 + R_{lin}/R_{ns}(e^{\frac{F}{F_{sat}}} - 1)]}{F/F_{sat}} e^{-\frac{F}{F_2}} \qquad (22)$$

Particularly, in case of two-photon absorption the induced absorption coefficient could be calculated as:

$$F_2 = \frac{\tau_p}{0.585 \int \beta_{TPA}(z) n^2(z) |\varepsilon(z)|^4 dz} \qquad (23)$$

Where β_{TPA} – two-photon absorption coefficient, τ_p – pulse length, n- refractive index and (z) describes the normalized electric field in the structure. Since the transverse mode profile of the pulses normally Gaussian, by integrating over beam profile, the reflectivity could be found as:

$$R^{Gauss}(F_p) = \frac{1}{2F_p} \int_0^{2F_p} R(F)\, dF \qquad (24)$$

Where $F_p = E_p/(\pi\omega^2)$. The equation (24) could be solved numerically, and agrees well with nonlinear reflectivity that has been observed experimentally. Another important parameter of the SESAM is temporal response that could be obtained from time-resolved differential reflectivity measurement. A representative time-resolved response curve for QW-based InGaAs SESAM designed for 1030 nm is shown on a Figure 61 [134].

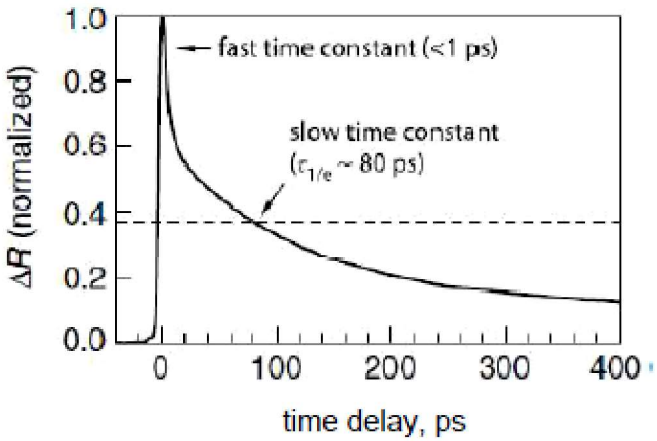

Fig. 61. Representative temporal impulse response for QW-based SESAM [134].

Most SESAMs demonstrate a bitemporal impulse response that could be written as:

$$\Delta R_{pp} = Ae^{-\tau/\tau_{slow}} + (1 - A)e^{-\tau/\tau_{fast}} \qquad (25)$$

with the amplitudes of slow τ_{slow} and fast τ_{fast} components equal to A and 1-A, respectively. In case of a QW-based SESAM, fast time constant determed by carrier-

carrier scattering processes, and slow time constant determed by interband trapping and recombination.

4.1.3 Design approaches for SESAMs

SESAM offers saturable absorber layers and field enhancement design flexibility, with macroscopic parameters that could be optimized over wide range for different lasers and wavelength. SESAM typically formed by semiconductor DBR, a quantum-well or quantum dots layer that acts as saturable absorber and top layers that allows control of dispersion and absorption. Growth of the SESAM structure could be performed employing MOVPE or MBE. Transfer-matrix algorithm allows calculate electric field inside and outside the SESAM structure. If I_{inc} is incident field intensity, n – refractive index, ε – normalized to 1 electric field, and $|\varepsilon(z)|^2$ is field enhancement, oscillating within values interval [0; 4] for a mirror with 100% reflectivity, then intensity inside the structure for a given position z could be written as [134]:

$$I(z) = n(z)|\varepsilon(z)|^2 I_{inc} \qquad (26)$$

with the field enhancement factor ξ_{abs} inside the absorber, and proportional to modulation depth ΔR denoted as:

$$\xi_{abs} = |\varepsilon(z_{abs})|^2 \qquad (27)$$

SESAM structure design could be resonant or antiresonant – both are shown on a Figure 61 for the structures based on AlAs / GaAs materials and wavelength of 960 nm [150].

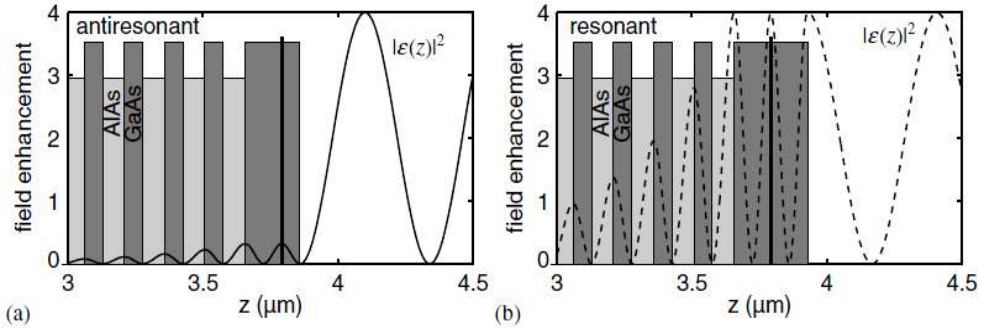

Fig. 62. Field enhancement and refractive index curve shown for resonant SESAM (a) and antiresonant SESAM (b)

The product of saturation fluence F_{sat} and modulation depth ΔR describes the energy required to saturate the SESAM completely.

Anti-resonant SESAM structure is useful since it has quite broad operation wavelength range, while keeping saturable absorber parameters almost constant, and relatively high saturation fluence. Therefore, antiresonant SESAM designs are beneficial for high-power lasers mode-locking and lasers with high intracavity pulse energies. Alternatively, strong wavelength sensitivity of the resonant SESAM structures could be beneficial in some cases since it allows to simultaneously tune operation wavelength and modulation depth, but operation wavelength range is largely limited and electrical field inside the structure is higher, that leads to more two-photon absorption. Mostly, SESAMs are designed in such a way that the pulse is many times saturating them, making sure they saturate much faster than gain, therefore mode waist on SESAM should be kept smaller than on gain. To achieve stable mode-locking, another important condition is that the recovery time of the SESAM should be fast. However, since saturable loses became higher with the recovery time getting shorter, that limits the design of the structures with very short recovery time due to low overall gain of VECSELs. A solution for that could be quantum wells that grown very close to top surface of the sample. In this case it was shown that surface recombination effects accelerating saturable absorber recovery due to presence of free bonds localizing the charge in the top layer of semiconductor. Another possibility for increasing the rate of recovery dynamics in SESAM is to employ a quantum dot-based SESAM. This allows to reduce simultaneously saturation fluence and modulation depth by reducing density of states.

4.1.4 Kerr lens mode-locking, optical Stark effect mode-locking, quasi-soliton mode-locking and colliding pulse mode-locking.

Kerr Lens Mode-locking (KLM) became successful mode-locking technique for solid-state lasers. KLM has been employed in Ti:Sapphire, with the first sub-100-fs pulses generation using KLM has been reported in 1991 [143] and sub-5-fs pulses reported in 1999 [144]. In KLM case, the effects of nonlinear focusing are combined with spatial apertures. On a Figure 63, laser cavity contain Kerr medium and gain medium. A pulse that builds up in this cavity undergoes self-phase modulation and self-focusing. Here, self-focusing is effectively nonlinear lensing of the laser beam induced by nonlinear refractive index of the Kerr medium.

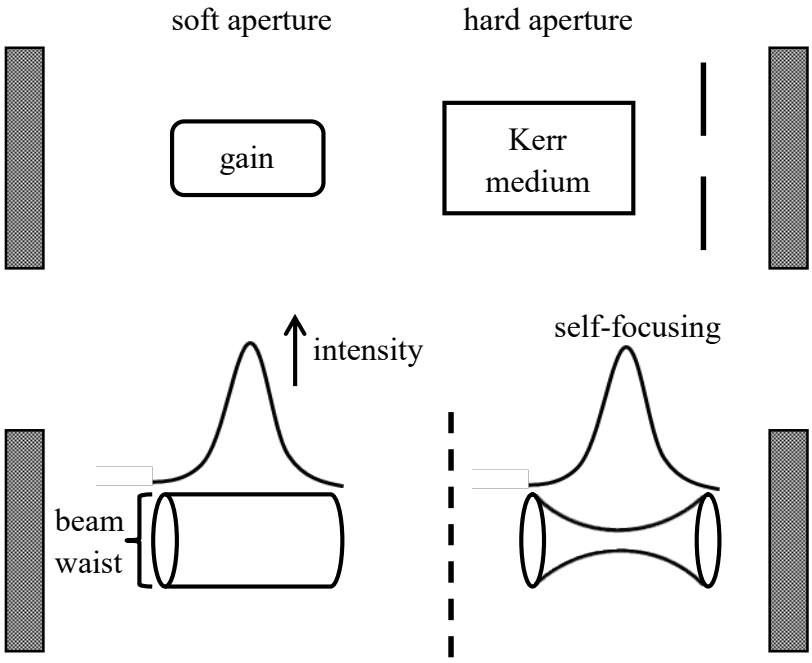

Fig. 63 A scheme of KLM in case of hard and soft aperture.

Since higher intensities undergo stronger focusing, a laser pulse that passes trough Kerr medium has time-dependent mode size. When a hard aperture is placed into a cavity, strongly self-focused light is passed through the aperture, and not self-focused light is passing through the aperture with some loss. KLM could also be achieved using soft aperture, avoiding placing an external aperture into a cavity. In soft aperture case, the laser beam self-focusing increases the overlap between signal in the gain medium and pump signal. It provides higher gain to the self-focused light than to non-self-focused light. That results in laser operating in pulsed mode. A general drawback of

KLM is that this process is not self starting and quite sensitive to external perturbations. KLM has also been reported in VECSELs [101, 102] where hard aperture is placed in front of high reflective mirror or output coupling mirror. However, these studies have opened a discussion whether or not reported lasers are actually clearly mode-locked.

Ultrafast optical Stark mode-locked VECSEL was demonstrated in 2008 [145], with 260 fs transform-limited pulses generated directly by an optical Stark passively mode-locked VECSEL at 1 GHz repetition rate being reported using surface recombination semiconductor saturable absorber mirror and a step-index gain structure. The optical Stark effect is the absorption resonance wavelength shift due to an external electric field of an optical pulse. If the absorber is designed in such a way that electric field of a laser pulse shifts the absorption peak away from the laser wavelength, then it will result in a decrease of the laser absorption. Therefore, the pulses with higher intensities will result at greater shift and more change in absorption, so optical Stark effect absorber gets more efficient with the pulses gets shorter. Figure 64 shows the absorption spectrum of an exciton resonance for a quantum well with no excitation, and also the Stark-shifted in the presence of an intense non-resonant pulse. The difference between two curves shows the modulation spectrum.

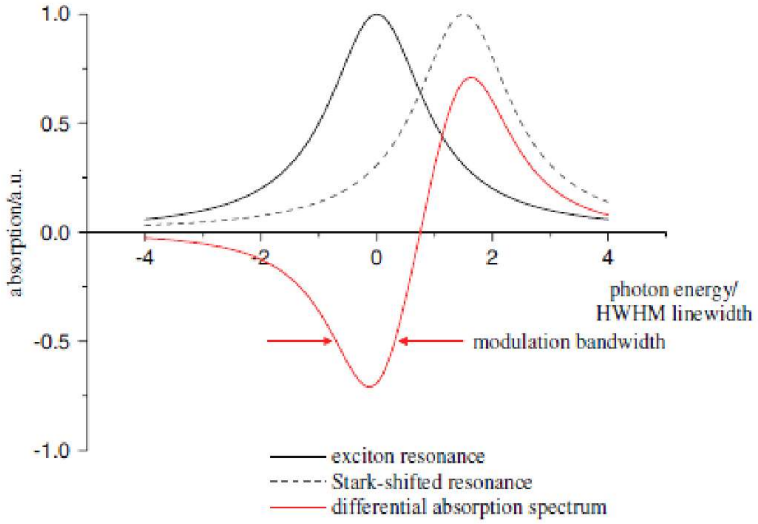

Fig. 64. Self absorption modulation induced by optical Stark effect (From [94]).

Studies aimed at Stark effect absorber modeling [146] demonstrated that pulses in this case could be shortened to a limit of twice the dephasing time of the medium.

Another mode-locking mechanism - quasi-soliton mode-locking, could be observed when GDD in cavity has opposite sign to second-order dispersion. In this case, pulse

spectral broadering due to intensity-dependent dispersion is followed by pulse duration compression to new minimal value due to fixed GDD action. Therefore, since the pulse shortening obtained without prevention of the noise amplification in cavity, quasi-soliton mode-locking also utilize saturable absorber for laser stabilization against CW lasing. This mode-locking principle was successfully used in Ti:sapphire and dye lasers. In VECSELs, Kerr nonlinearity effect is relatively weak, however light-induced changes of the carrier density can result at nonlinear phase changes, similar to those from the Kerr effect. In that case, quasi-soliton pulses can be obtained in the normal dispersion regime close to the Fourier transform limit [147].

The demonstration of the generation of sub-100-fs pulses using passively-mode-locked dye laser in a ring cavity, called colliding pulse mode-locked (CPM) ring dye laser, was reported in 1998 [148]. Original CPM dye laser contained an absorber dye jet within a ring cavity. In a such cavity geometry, two counter propagating optical pulses colliding in saturable absorber and produce a transient grating, leading to stabilization, synchronization and shortering the pulses. As a result, coherent interaction of the optical pulses decreases saturation energy and increase the effective cross section of the saturable absorber. Recently, CPM was reported in VECSELs [84]. In the reported studies, semiconductor gain medium and SESAM have been placed in a ring cavity to ensure stable colliding pulse operation. Using this geometry, 195fs pulses with an average power of 225 mW at a repetition rate of 2.2 GHz where demonstrated.

4.2 Concept and structure of SESAME

One of the important conditions for the stable VECSEL mode-locking using SESAM is a tight cavity mode focusing on a SESAM, in order to keep the saturation level constant. At a higher repetition rates operation, it leads to power being deposited to smaller spots, multiple SESAM bleaching per round trip and a higher temperature rise that could result at thermal damage of the SESAM. Efficient thermal management can address this problem. Heat removal from the SESAM could be obtained for example using various heat spreaders combined with substrate removal, or cooling the SESAM by liquid nitrogen flow. For mode-locking around 1μm, it is also possible to apply thin alumina layer on a SESAM surface, allowing two-dimentional heat removal.

An alternative approach could be the one similar to IR MECSEL, described earlier in this thesis. DBR in SESAM provides high reflectivity ensures E-field pinning and could be similar to those used in VECSEL gain samples or with a bit offset centre wavelength that sometimes could lead to better dispersion compensation. Spacing between the top of the DBR and the air interface sets the magnitude of the E-field at the position of the quantum well. SESAM structure excluding DBR could be MOVPE grown directly on a sacrificial layer that grown on GaAs substrate. As in case of MECSEL, SESAME (Semiconductor Saturable Absorber Membrane) benefit from extended range of potential materials systems choices and better heat management, due to the absence of multilayer DBR. SESAME in addition makes it possible to use more resonator configurations.

An unprocessed SESAME used further in this thesis for mode-locking experiments has been designed jointly with IHFG, University of Stuttgart and MOVPE grown at the University of Stuttgart in a 3×2” close coupled showerhead reactor on a GaAs substrate. The resulting SESAME structure, including a 200 nm AlAs sacrificial layer is shown on a Figure 65.

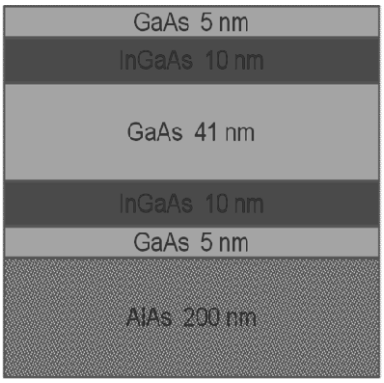

Fig. 65. Unprocessed SESAME structure (GaAs substrate layer not shown).

SESAME, shown on a Figure 65 has been designed for VECSEL mode-locking at ~1000nm. This is a quarter-wave thick gallium arsenide film containing two $In_{0.2}Ga_{0.8}As$ surface quantum wells 5 nm from both surfaces and with a 200 nm thick AlAs etch stop sacrificial layer, grown on GaAs substrate. The idea of using two quantum wells is to make a final design as flexible as possible. For example, in case SESAME mounted to dielectric mirror, it would have one of the QWs on a node, and the other on an anti-node. However, the idea was also to use same SESAME in transmission geometry, where there is a lot less pinning of the E-field. By using a quarter-wave thick design it is possible to force the laser to either work with a node on one well, and and anti-node on the other, with equal E-field on each QW, or some sort of intermediate case with the lowest overall insertion loss, but in can't avoid both QWs. The dispersion and spectral filtering in this design are minimized due to the quarter wavelength device thickness. After the growth, membrane SESAM wafer thickness has been checked using SEM (University of Stuttgart). The resulting SESAME thickness, shown on a Figure 66, was measured to be 71 nm, followed by 194 nm sacrificial AlAs layer.

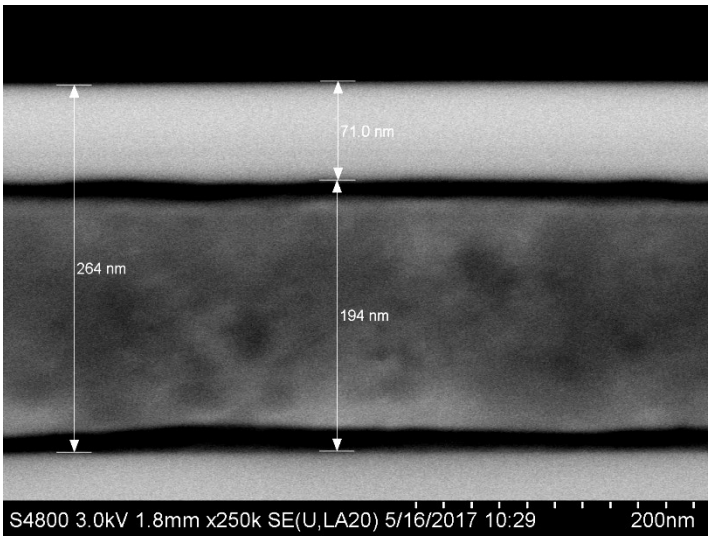

Fig. 66. SEM image, showing the thickness of the SESAME unprocessed wafer.

According to SEM, the thickness of the final structure matches with the designed structure.

4.2.1 Processing and mounting

First attempts for SESAME etching were done using wet chemical etching processes that include continually stirring the sample in an ammonium hydroxide solution $NH_4OH:H_2O_2$ in various ratios, including 1:2, 1:30, and 1:100. However, such a solution was not selective enough against the 5 nm GaAs layer, which followed after AlAs sacrificial layer. Therefore, in this case the etching approach known as lateral etching has been used [149, 150]. In this thesis, the above mentioned epitaxial lift-off process allows the separation of a thin layer of III-V material from the substrate by selective etching of an intermediate AlAs layer with 10% HF solution. The etching was performed in a 10% HF solution, under the following procedure:

1. Pieces of SESAME 6x4 mm in size were cleaved from the wafer and coated with 2.4 mg of Apiezon W wax using trichloroethylene (TCE) as a solvent. A drop of solvent was placed on a piece of a wafer then wax placed into a solvent drop and gently agitated to dissolve evenly. These steps resulted on an even ~50-100 microns thick layer of wax. Then cleaved and coated SESAME wafer piece was left to dry for about 12 hours.
2. The edges of the wafer were scraped gently using a scalpel blade to remove any wax that has gone over the edges and could prevent the acid to etch the AlAs layer.
3. The wax was annealed by placing the sample on a hot plate for 30 min at ~70 C.
4. The initial wafer piece was cleaved into ~2×2 mm pieces.
5. Three pieces where then placed into the pre-mixed 10% HF solution. Every ~30 minutes the dish with HF was gently stirred and the samples were gently moved around within HF solution using tweezers to check if the membranes have separated from the substrate.
6. After ~90 minutes the separation of the SESAME was observed. After the separation, SESAME was transferred into a pot of distilled water. Normally, the membrane was held on the surface by surface tension while the substrate is sunk.
7. To ensure complete washing of the acid off the SESAME, the membrane was transferred into a second pot of water.

8. The membrane was fished onto the heatspreader (SiC and diamond), removed from the water and left for ~12 hours to dry and ensure good contact bonding.
9. The wax was then washed off in one pot of TCE, followed by a rinse in a second pot of clean TCE.
10. The SESAME surface then was checked using optical microscope, placed into a sampleholder and used for experiments.

Two pieces of etched SESAME, about 2×2 mm in size each, were transferred to diamond and SiC. Surface quality of both samples has been afterwards characterized in optical microscope under ×5 times magnification. Figure 67 a) and b) representing SESAME mounted on diamond and SiC respectively.

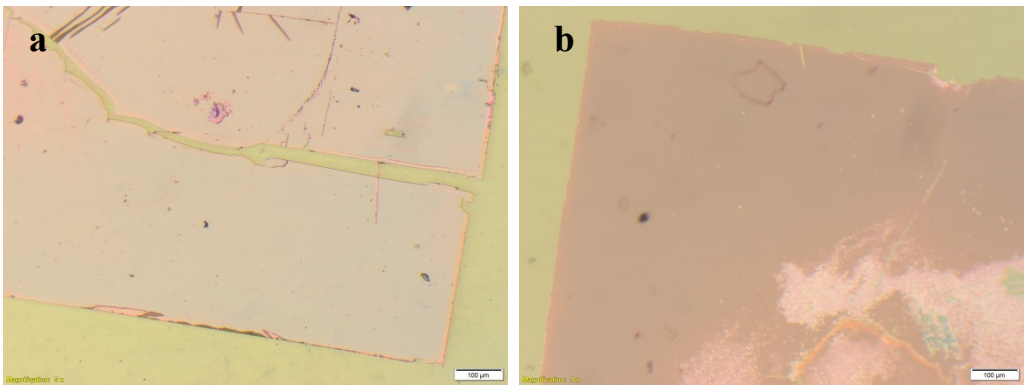

Fig 67. Processed SESAME mounted on diamond (a) and SiC (b) substrates.

It should be noticed that this process is suitable for fabrication of up to tens of samples in one go. However, only about 70% of SESAME samples etched where removed from the substrate successfully. The success rate in this case could be increased by adjusting HF concentration and more precise control of Apiezon wax quantity, as well as better etching time control. However, the necessity of scraping the wafer edges, requirement for a periodic sample stirring in solution to access substrate separation and certain limitations applied to sample size for better epitaxial lift-off makes this process not optimal for translation it to manufacturing.

4.2.2 Characterization and complexities for standard techniques

Etched SESAME pieces that mounted to SiC and diamond heat speaders was used for further experiments aimed at characterization of membrane SESAM in a few types of cavities. A 1015 nm antiresonant VECSEL gain sample was used. It has ×10 InGaAs QWs spaced one per antinode in an antiresonant active region on top of a GaAs/AlAs based DBR. Gain sample was thermally managed by substrate removal and indium soldering onto a thermal diamond. This gain sample was used in all characterization and mode-locking experiments that will be described further.

A CW straight cavity was used to test the gain chip performance and is described below. Straight cavity has a 100 mm 0.7% OC. 30 mm pump collimation lens and 75 mm focusing lens giving a pump spot diameter of ~260 µm. Calibration results are shown on a Figure 68.

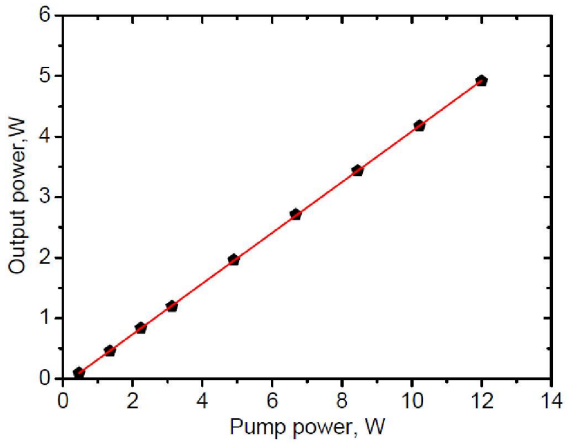

Fig 68. VECSEL output power as a function of pump power cavity.

To check the ways how SESAME could be introduced in laser cavity and its influence on threshold and output power, a cavity shown on a Figure 69 was used. A pump spot size was ~260 µm.

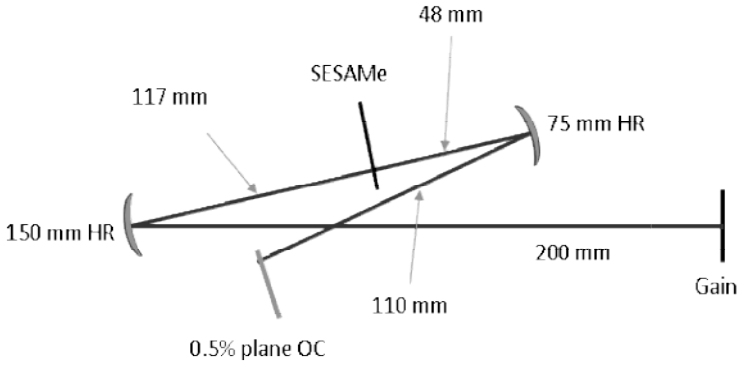

Fig 69. Cavity for SESAME initial characterization.

For the cavity above, output power curves were measured to test a SESAME loss. In this case, output power curves were measured for the laser alone, the laser on the SiC but missing the membrane, the diamond but missing the membrane, and the membrane on the SiC. Representative data are shown on a Figure 70.

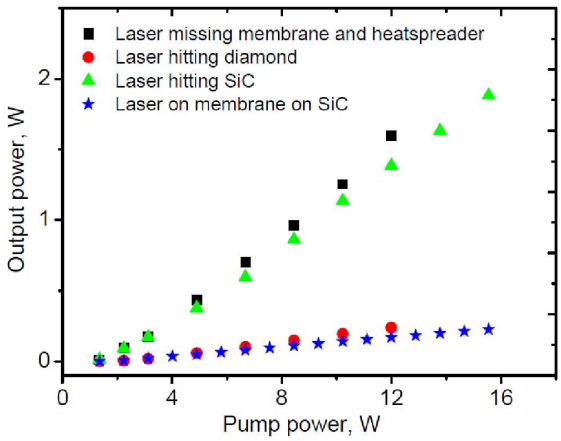

Fig 70.Outputpower vs pump current for different heatspreader and membrane positions.

As could be seen from the Figure 70, loss of the particular used diamond is very high also the laser did not actually lase when aligned on the membrane on the diamond. Therefore, only the SiC heatspreaders were used for further characterization and mode-locking experiments.

Mode-locking using SESAME has additional challenges in compare to conventional SESAM. For example, bonding of the SESAME membrane to SiC results at SiC optical properties influence on mode-locking and modulated spectrum corresponding to etalon modes that also could affect stable mode-locking. Another issue, in particular, with the cavity shown on a Figure 71 is that there will be Fresnel reflections from both the membrane surface and the SiC - air interface, meaning that this cavity is divided into three parts. In order to achieve harmonic mode-locking, all three sub cavities would have to be resonant with each other, and so mode-locking wasn't expected. In this case, a quick check using radio frequency spectrum analyzer (RFSA) did not show any sign of mode-locking.

To overcome the problem of the various sub cavities, the ring cavity shown on Figure 71 was built. The pump spot size was ~260 μm.

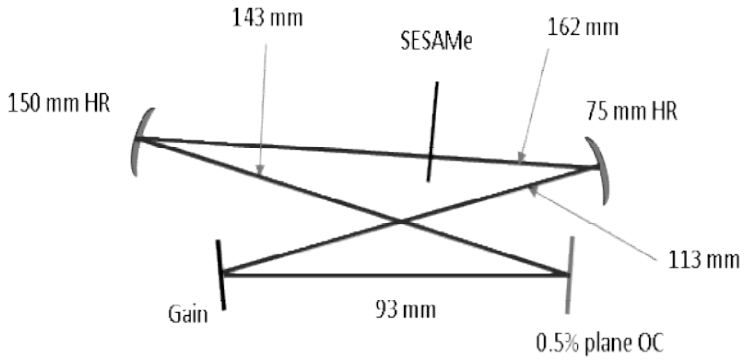

Fig 71. Ring cavity with SESAME mounted on SiC heatspreader.

Output power curves for this laser were taken in cases without the membrane or heatspreader, on the heatspreader, and on the membrane. Representative data are shown on a Figure 72 below.

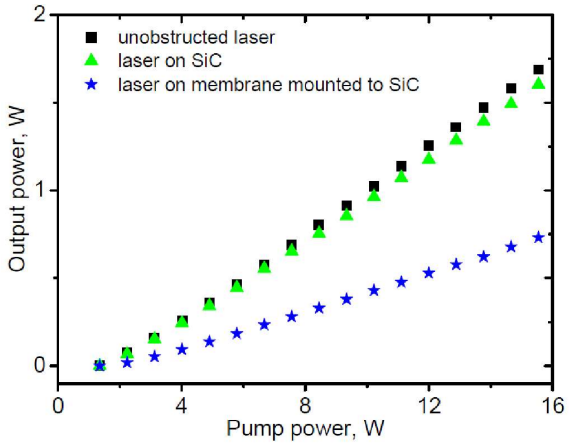

Fig 72. Output power curves for unobstructed laser, laser hitting SiC and membrane on a SiC in a ring cavity

RF spectra on Figure 73 show harmonics of similar height (some with sidebands, some without), but individual harmonics are not particularly clean, so it does not appear that this laser is mode-locked. This is supported by the observation that the RF spectra taken when missing the membrane looks very similar to when hitting the membrane.

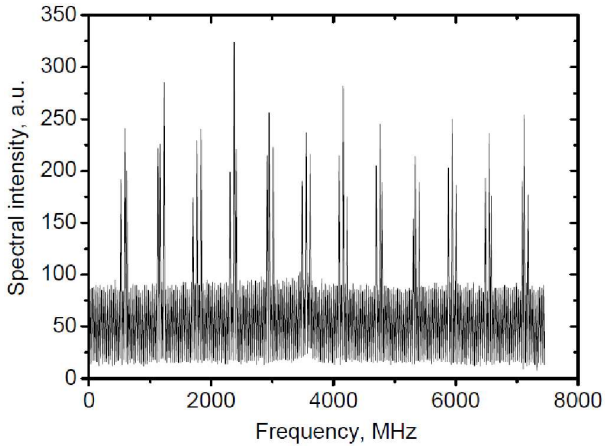

Fig 73. RF spectra of laser operating in ring cavity.

Optical spectra on Figure 74 generally have bandwidths of ~2-4 nm and show modulation from the SiC etalon. A set of the data was taken on the SiC but missing the membrane and demonstrated shift to a longer wavelength.

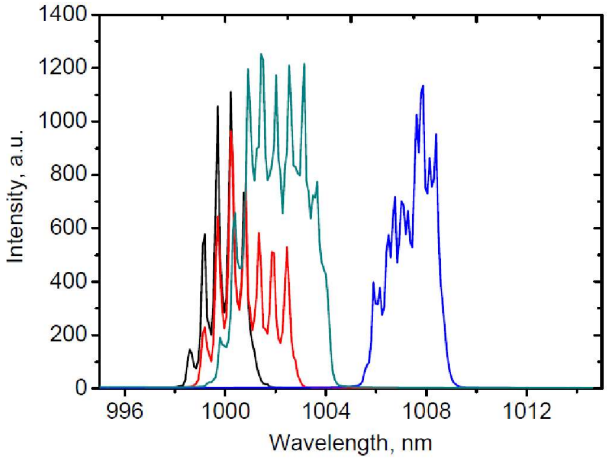

Fig 74. Optical spectra of ring cavity laser with SESAME bonded to SiC

Figure 75 shows a SESAME in operating ring cavity laser.

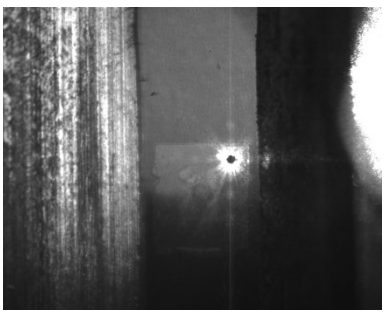

Fig 75. Operating ring cavity laser: laser spot on a SESAME

It was not entirely clear why the ring cavity above isn't mode-locking. One possibility that can be investigated is the spot size on the membrane. Building ring cavitites with different spot sizes is quite time consuming, so possible alternative is to use SESAMEs as end mirrors in V or Z cavities which are better suited to varying spot sizes. Another option is to produce and try another SESAME samples. This approach will be discussed in next chapter.

4.2.3 SESAME mode-locked VECSEL

To proceed further with experiments aimed at gain sample mode-locking using SESAME, three more samples were etched following the process described in chapter 4.2.1. Two samples detached from their substrates and were transferred in this case onto a plane dielectric HR mirror that has a reflectivity~99.95% but suffer from poor thermal conductivity. In contrast, alternatives like metallic mirrors for a given wavelength have better thermal conductivity however their reflectivity is lower. As lower reflectivity adds more loses into the cavity which affects laser operation, an HR mirror was used in this case. One of two membranes that located nearer the edge of the mirror had better surface quality, so this was the membrane that was used. The photo of the SESAME on HR mirror that was used further in experiments is shown on a Figure 76.

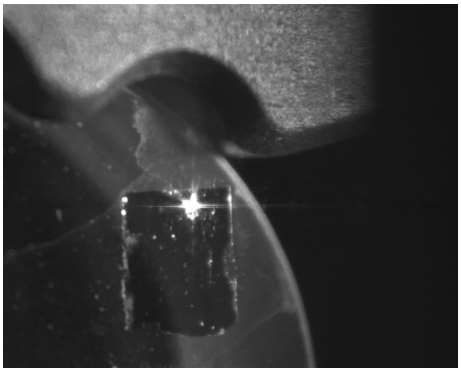

Fig. 76. Processed SESAME bonded to HR mirror

The SESAME sample bonded to HR mirror was tested in a z-cavity shown on a Figure 77.

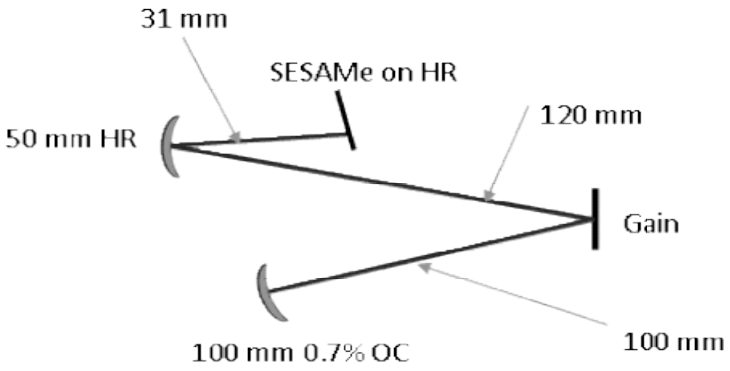

Fig. 77. Z-cavity containing gain sample and SESAME on HR mirror

The same pump spot size of ~260 µm was used and the spot size on the SESAME was ~23 µm. The threshold missing the SESAME was 1.34 W and was 2.3 W in the

SESAME. The power was limited very strongly by heating in the SESAME due to the poor thermal conductivity of the glass HR. Therefore, power was limited to ~2 mW at pump powers only fractionally above threshold.

Despite this low power, clean mode-locking was observed. Clean RF spectra demonstrating multiple harmonics shown on a Figure 78.

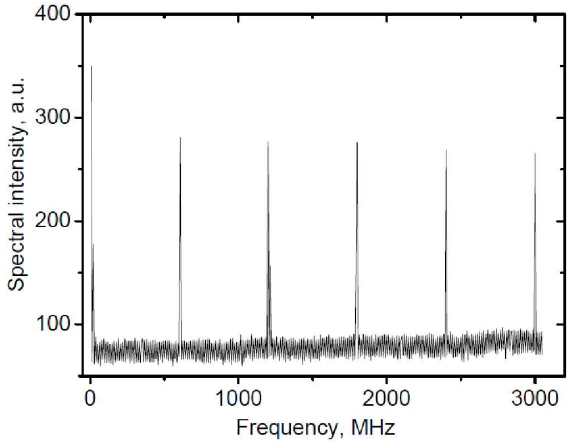

Fig. 78. RF spectra demonstrating multiple harmonics

However, the power was too low to get FROG traces. Optical spectra on a Figure 79 showed bandwidths of ~1 nm.

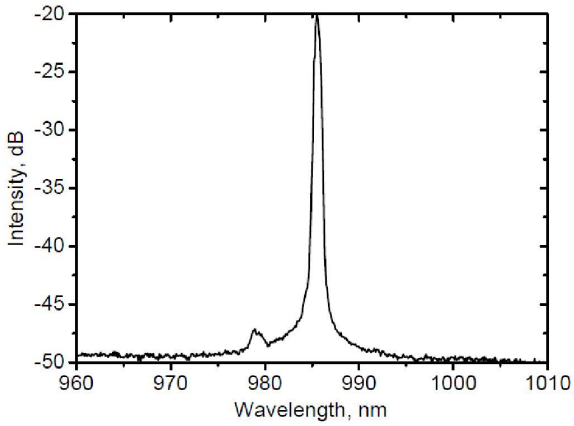

Fig. 79. Optical spectra of SESAME mode-locked VECSEL

To check whether a larger spot on the membrane would be better, the following cavity, shown on a Figure 80 has been built:

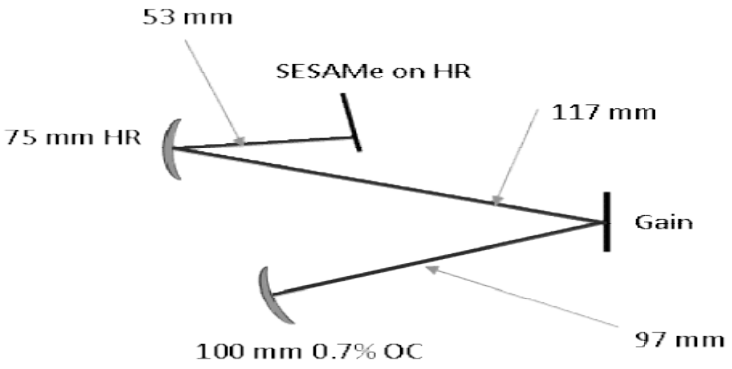

Fig. 80. Cavity for VECSEL mode-locking using SESAME mounted to HR mirror. The spot size on the SESAME is 38 microns.

In this case the spot size on the SESAME was ~38 microns. Slightly higher powers up to ~5 mW were possible but mod-locking was only stable at powers ~2 mW. The mode-locking was also slightly more stable than in the previous case. Otherwise mode-locking performance was similar. Data from RF spectra, fast scope traces and optical spectra are shown on the Figures 81-83. Fast scope traces of mode-locked VECSEL on a Figure 82 are inverted since an inverting amplifier was used to boost signal from fast photodiode to enable fast scope trace to be recorded.

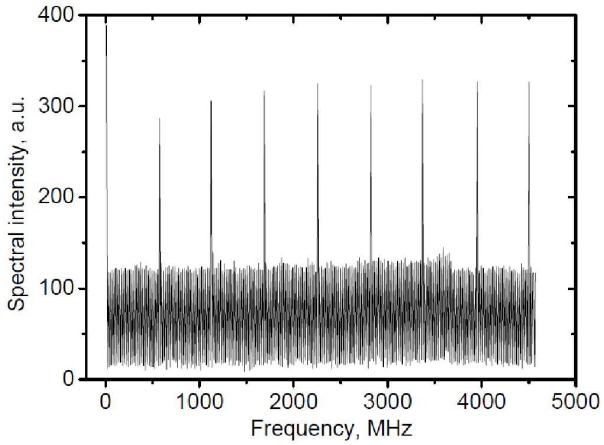

Fig. 81. RF spectra of mode-locked VECSEL for cavity from Figure 80.

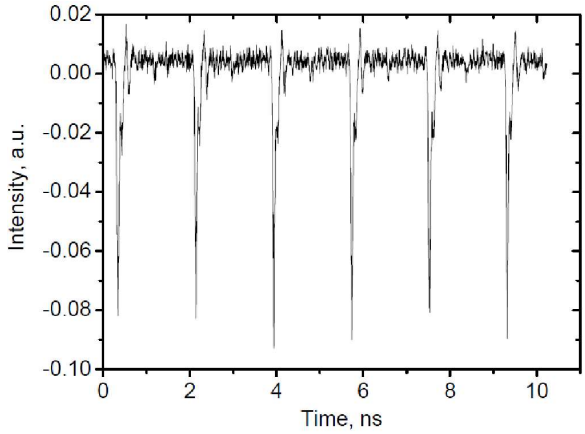

Fig. 82. Fast scope traces of mode-locked VECSEL for cavity from Figure 80.

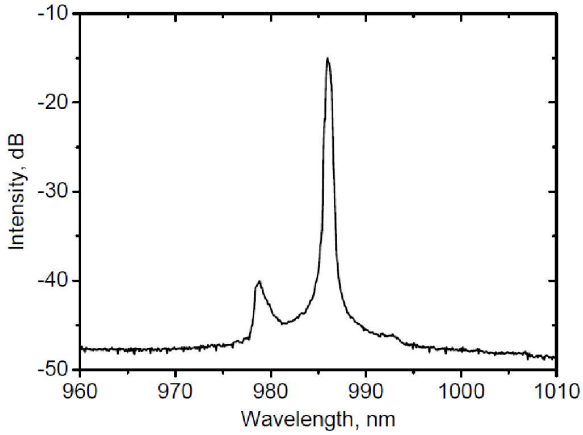

Fig. 83. Optical spectra of modelocked VECSEL for cavity from Figure 80.

To try a larger pump spot the 75 mm HR was replaced by a 100 mm HR giving a SESAMe spot of ~60 microns. Mode-locking was not seen in this case. The same cavity was tried with a 1.45% output coupler rather than a 0.7% OC. This allowed higher output powers (up to ~8 mW) and appeared to be marginally closer to mode-locking. Next attempt was made using the 1.45% output coupler and switching back to a 75 mm HR. Mode-locking was seen again, but with stability made worse by thermal problems. Mode-locking would be stable for a few seconds before switching off then back on a few seconds later. This presumably indicated heating of the SESAME when mode-locked, followed by cooling when the mode-locking switches itself off. This may well have been down to wavelength shifts and so might have been addressed by temperature tuning, but we did not investigate this in detail given such a low performance laser. Finally the 1.45% OC was tested with the 50 mm HR. This laser was also really quite unstable. RF spectra were not recorded because of this. When more hopeful RF spectra

were seen (Figure 84), they were linked to broader optical spectra which might hint that the SESAM could be capable of supporting fs pulses.

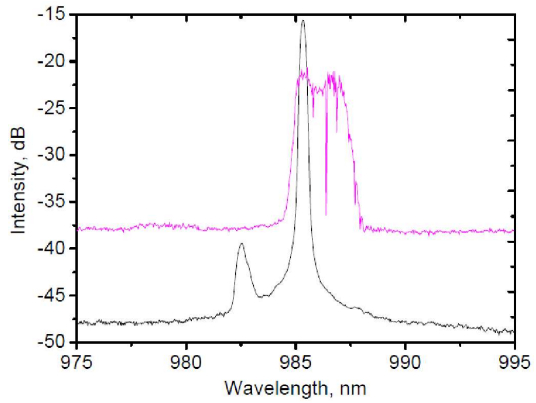

Fig. 84. Optical spectra of the laser using cavity geometry from Figure 80 with the 1.45% OC and the 50 mm HR.

In order to try to address the thermal problems while also using a z cavity for simplicity, the SESAME has been placed on SiC from earlier in front of a mirror. This obviously introduces an etalon into the cavity, so is not ideal. Spectra on a Figure 86 shows strong modulation from the etalon and quite broad bandwidths. This used the same z cavity from Figure 80, but with the 75 mm mirror replaced with a 50 mm mirror, reducing the spot size on the SESAME. Output power of up to 1 W was possible in this cavity configuration. Data on Figures 85-88 are illustrating modelocking of VECSEL gain chip using SESAME. Figure 85 shows harmonics with similar high with some sidebands due to SiC etalon. Figures 87 and 88 showing retrieved spectrum, spectral phase as well as temporal intensity profile and temporal phase respectively as measured by the FROG system.

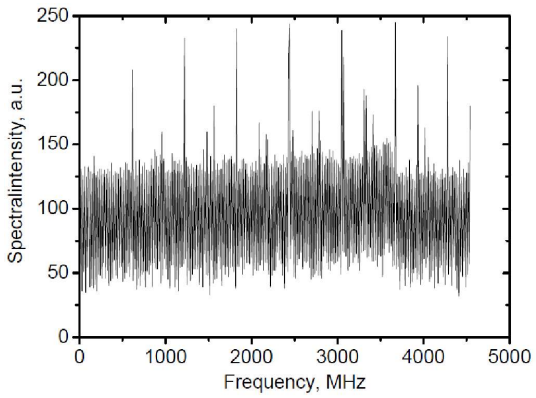

Fig. 85. RF spectra of SESAME mode-locked VECSEL. In this case, SESAME is bonded to SiC heatspreader.

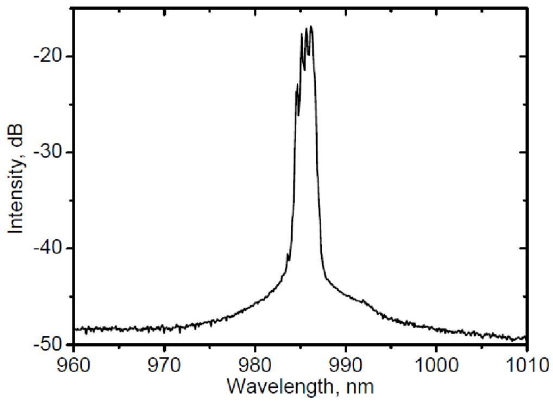

Fig. 86. Spectra of SESAME mode-locked VECSEL, demonstrating strong modulation from the SiC etalon.

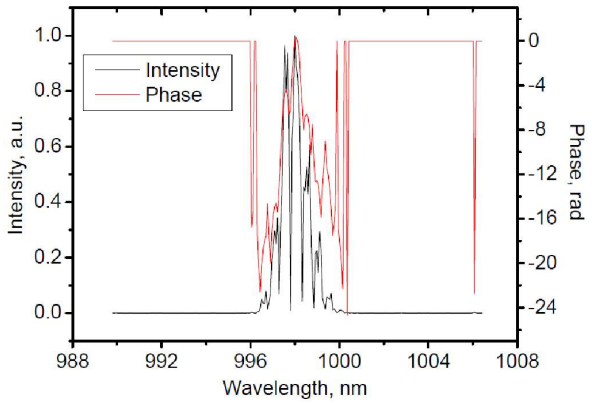

Fig. 87. Retrieved spectrum and spectral phase of the SESAME mode-locked VECSEL.

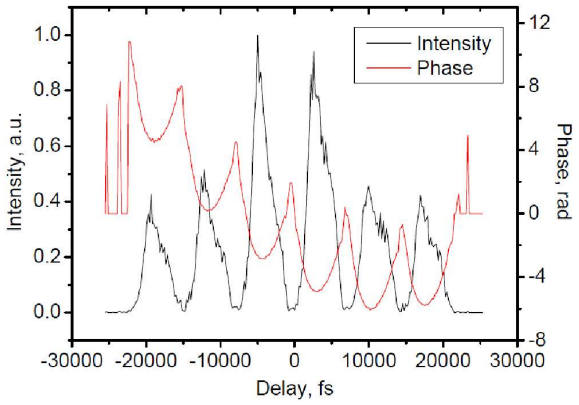

Fig. 88. Retrieved temporal intensity profile and temporal phase of SESAME mode-locked VECSEL.

The next step towards mode-locking using SESAME was to try a ring cavity. The cavity shown on a Figure 89 chosen as being having relatively easy configuration, and having a spot size similar to the z cavities used previously.

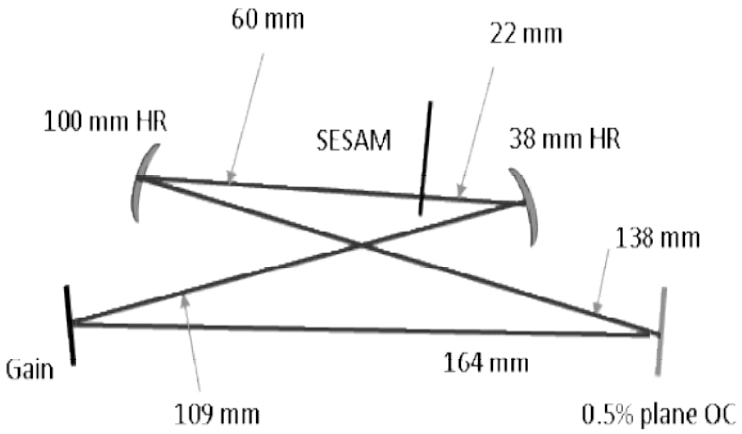

Fig. 89. Laser cavity being used for SESAME mode-locking having similar spot sizes in compare to z-cavities used in previous experiments.

Mode-locking in this case was demonstrated, but only if the cavity was slightly misaligned, and only close to threshold. Therefore, it wasn't possible to get FROG data. The RF spectra shown in Figure 90 confirming mode-locking, showing harmonics of similar high, and fast scope traces on a Figure 91 show that the laser appears to be single pulse. This is unexpected as the SiC etalon should force the laser to operate at a high repetition rate. This may explain the misalignment needed to get mode-locking – it is possible that the laser is only mode-locking when the laser is aligned at the very critical point where the etalon reflections are just lossy enough to suppress lasing, but where the laser can just still work.

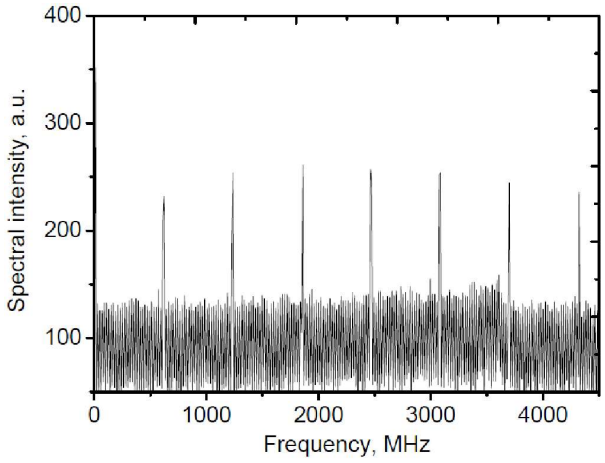

Fig 90. RF spectra of SESAME mode-locked VECSEL, operating in cavity shown on Figure 89.

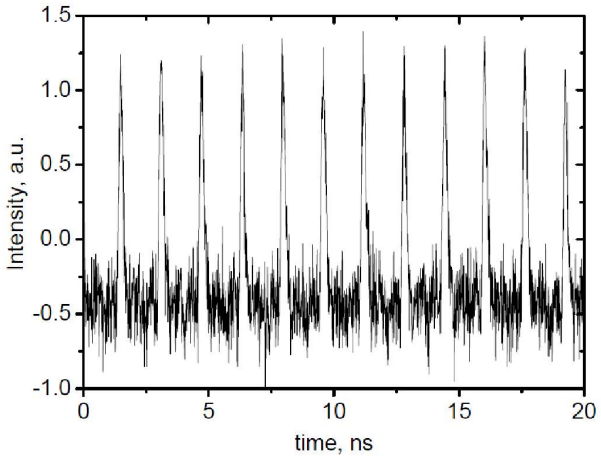

Fig. 91 Fast scope traces of SESAME mode-locked VECSEL, operating in cavity shown on Figure 89.

4.2.4 Conclusions and future work

For the first time, SESAME was grown and processed using HF lateral etching method. VECSEL mode-locking has for the first time been demonstrated using SESAME. The power was limited very strongly by heating in the SESAME due to the poor thermal conductivity of the glass HR, on which SESAME was bonded. That leads to output power being limited to ~2 mW at pump powers only fractionally above threshold. Despite this low power, clean mode-locking was observed. When the SESAME has been placed on SiC from earlier in front of a mirror, it introduces an etalon into the cavity. However, with z-cavity configuration in this case output power of up to 1 W was possible. Mode-locking was demonstrated also in a ring cavity with SESAME mounted to SiC heatspreader, but only when the cavity was slightly misaligned, and only close to threshold. Further work related to improving mode-locking of VECSELs and MECSELs using SESAMEs could include mastering of the etching protocols to achieve better surface quality and bonding, employing new types of gain structures and surface SESAM structures, better cooling mounts to allow effective heat extraction and employing high quality diamonds, also from both sides of the gain sample, to obtain higher heat extraction rates. Finally developing techniques which allow a SESAME to be used in transmission at Brewsters angle would be the most likely technique to suppress etalon effects which are a key limitation currently.

5. Overall Conclusions and Future Work

5.1 Conclusions

The widely-used FOM approach has been for the first time validated and tested over a large parameter space. It was observed that pulse duration has little effect on multiphoton signal provided that the average power can be adjusted to keep the figure of merit constant. It was shown that there is an optimal repetition rate for a given sample and average power, with excessively low repetition rates leading to lower than predicted signal levels due to bleaching and/or damage, and excessively high repetition rates leading to lower than expected signal levels due to incomplete recovery of the fluorophore between excitations. The ability to use longer pulses opens up the possibility of multi-photon microscope systems which use several low cost, fixed wavelength longer pulse duration laser sources.

Using wet chemical etching, a IR MECSEL was successfully processed and lasing at 1007 nm was demonstrated. A record to-date 10.1 W continuous wave output power from an IR MECSEL on SiC heat spreader at 1007 nm was demonstrated. Laser slope efficiency of 21.1% and 27.5% at heat sink temperatures of 12 °C and -10 °C respectively where achieved. It was shown, that the laser wavelength of output laser beam could be tuned from 995 nm to 1020 nm by introducing 0.5 mm quartz birefringent filter into cavity.

For the first time, a membrane semiconductor saturable absorber mirror (SESAME) was grown and processed using HF lateral etching method. VECSEL mode-locking has for the first time been demonstrated using a 1015 nm antiresonant VECSEL and SESAME in a ring and z shaped cavities. Improved thermal management possibility and wider materials chose of IR MECSEL in compare to VECSELs combined with wavelength flexibility makes SESAME mode-locked IR MECSELs promising candidate for MPI, where imaging systems employing several different fixed-wavelength mode-locked laser sources to reach a set of required wavelengths.

5.2 Future work

Further improvement should be made to employ for MPI a several low cost, fixed wavelength, sub-picosecond optically pumped MECSELs instead of single sources with high cost and complexity. This improvement will include work towards more efficient IR MECSEL structure designs, better and more reproducible etching procedures, allowing smother and more uniform surface quality. It will also entail using high quality diamond and SiC heat spreaders, development of effective cooling mounts.

The sandwich geometry could be employed further, provided that the cooling mount will allow effective and reproducible mounting of sandwiched membrane, avoiding membrane damage. Another options to improve overall IR MECSEL efficiency could be using multi-pass geometry to use reflected pump beam or using total internal reflection geometry. Further work related to improving mode-locking of VECSELs and MECSELs using SESAMEs could include mastering of the etching protocols to achieve better surface quality and bonding, employing new types of surface SESAM structures, better cooling mounts to allow effective heat extraction and employing high quality diamonds, also from both sides of the gain sample, to obtain higher heat extraction rates.

List of publications

1. Mirkhanov, S., Quarterman, H. A., Kahle, H., Bek, R., Pecoroni, R., Smyth, S. J. C., Vollmer, S., Swift., S., Michler., P., Jetter, M., Wilcox, K. G. DBR-free semiconductor disc laser on SiC heatspreader emitting 10.1 W at 1007 nm. Electronics Letters, 53 (23), 1537-1539, 2017.

2. Mirkhanov, S., Quarterman, A. H., Smyth, C. J. S. P, Praveen, B.B., Appleton, P., Thomson, C., Swift, S., Wilcox, K. G. Optimal repetition rate and pulse duration studies for two photon imaging. Proceedings of SPIE, 2017.

3. Mirkhanov, S., Quarterman, A.H., Swift, S., Praveen, B.B., Smyth, C. J. C., Wilcox, K.G. Multiphoton imaging with high peak power VECSELs. Proceedings of SPIE, 2016.

4. Quarterman, A. H., Mirkhanov, S., Smyth, C. J C., Wilcox, K.G. Measurements of nonlinear lensing in a semiconductor disk laser gain sample under optical pumping and using a resonant femtosecond probe laser. Applied Physics Letters, 109, 121113 (2016).

5. Smyth, C. J. C., Mirkhanov, S., Quarterman, A. H., Wilcox, K. G. Use of scattering cooling liquid in a solar Nd: YAG laser . Optics InfoBase Conference Papers, CLEO Europe, 2017.

6. Smyth, C.J.C., Mirkhanov, S., Quarterman, A.H., Wilcox, K.G. Thermal management of VECSELs by front surface direct liquid cooling. Proceedings of SPIE, 2016.

7. Quarterman, A. H., Smyth, C. J. C., Mirkhanov, S., Wilcox, K. G., Resonant measurements of nonlinear lensing in a VECSEL gain sample. Proceedings of SPIE, 2016.

References

[1] Denk W., Strickler J.H., Webb W.W. Two-photon laser scanning fluorescence microscopy. Science. 1990;248(4951):73-6.

[2] Potter, S.M., Vital imaging: two photons are better than one. Curr. Biology., 6, 1596-1598, 1996.

[3] Kawakami, R., et al., *In vivo* two-photon imaging of mouse hippocampal neurons in dentate gyrus using a light source based on a high-peak power gain-switched laser diode. Biomed. Opt. Express, 6 (3), 891-901, 2015.

[4] Bewersdorf, J., Hell, W., Picosecond pulsed two-photon imaging with repetition rates of 200 and 400 MHz. Journal of Microscopy, 191 (1), 28-38, 1998.

[5] F. Helmchen, W. Denk, Deep tissue two-photon microscopy. Nat Methods. 2(12):932-40, 2005.

[6] Sava Sakadić, Vertical integration of ultrafast semiconductor lasers . Appl. Phys. B, vol 88, pp 493, 2007.

[7] M. Kuznetsov ; F. Hakimi ; R. Sprague ; A. Mooradian. High-power (>0.5-W CW) diode-pumped vertical-external-cavity surface-emitting semiconductor lasers with circular TEM/sub 00/ beams. IEEE Photonics Technology Letters, pp. 1063-1065, Vol.9, Issue 8, 1997.

[8] D. Waldburger, S.M. Link, M. Mangold, C. G. E. Alfieri, E. Gini, M. Golling, B. W. Tilma, and U. Keller., High-power 100 fs semiconductor disk lasers. Optica, Vol. 3, Issue 8, pp. 844-852, 2016.

[9] K. G. Wilcox, A. C. Tropper, H. E. Beere, D. A. Ritchie, B. Kunert, B. Heinen, and W. Stolz, 4.35 kW peak power femtosecond pulse mode-locked VECSEL for supercontinuum generation. Optics Express, Vol. 21, Issue 2, pp. 1599-1605, 2013.

[10] S. Ranta, A. Härkönen, T. Leinonen, L. Orsila, J. Lyytikäinen, G. Steinmeyer, and M. Guina. Mode-locked VECSEL emitting 5 ps pulses at 675 nm. Optics Letters, Vol. 38, Issue 13, pp. 2289-2291, 2013.

[11] Moloney, J.V. et al., Nonequilibrium and thermal effects in mode-locked VECSELs. Optics Express, 22 (6), 6422-6427, 2014.

[12] Yang, Z., Albrecht, A. R., Cederberg, J. G., and Sheik-Bahae, M., Optically pumped DBR-free semiconductor disk lasers, Opt. Express, 2015, 23, (26), pp. 33164–33169.

[13] M. Göppert-Mayer, Elementary processes with two quantum transitions, 1930.

[14] W. Kaiser and C. G. B. Garrett, Two-Photon Excitation in CaF_2: Eu^{2+}, Phys. Rev. Lett. **7**, 229,1961.

[15] C. Xu and W.W. Webb., Measurement of two-photon excitation cross sections of molecular fluorophores with data from 690 to 1050 nm. Journal of the Optical Society of America B, Vol. 13, Issue 3, pp. 481-491, 1996.

[16] Monaghan, M.G., Kroll, S., Brucker, S.Y., Schenke-Layland, K., Enabling Multiphoton and Second Harmonic Generation Imaging in Paraffin-Embedded and Histologically Stained Sections. Tissue Eng Part C Methods., 22(6):517-23, 2016.

[17] White J.G., Squirrell, J.M., Eliceiri, K.W., Applying multiphoton imaging to the study of membrane dynamics in living cells., Traffic., 2(11):775-80., 2001.

[18] McIntosh, A.L, Gallegos, A.M., Atshaves, B.P., Storey, S.M., Kannoju, D., Schroeder, F., Fluorescence and multiphoton imaging resolve unique structural forms of sterol in membranes of living cells. J Biol Chem.; 278(8):6384-403., 2003.

[19] P. Theer, M. T. Hasan, and W. Denk., Two-photon imaging to a depth of 1000 μm in living brains by use of a Ti:Al_2O_3 regenerative amplifier., Optics Letters, Vol. 28, Issue 12, pp. 1022-1024, 2003.

[20] Kobat, D, Durst, M.E., Nishimura, N., Wong, A.W., Schaffer, C.B., Xu, C. Deep tissue multiphoton microscopy using longer wavelength excitation. Opt Express ;17(16):13354-64, 2009.

[21] Svoboda, K., Denk, W., Kleinfeld, D,, Tank, D.W., In vivo dendritic calcium dynamics in neocortical pyramidal neurons. Nature, 9;385(6612):161-5, 1997.

[22] Brakenhoff, G. J., Muller, M., and Ghauharali, R. I. Analysis of efficiency of twophoton versus single-photon absorption for fluorescence generation in biological objects. J. Microsc. 183, 140–144, 1996.

[23] Botcherby, E.J, Smith, C.W., Kohl, M.M., Débarre, D., Booth, M.J., Juškaitis, R., Paulsen, O., Wilson, T., Aberration-free three-dimensional multiphoton imaging of neuronal activity at kHz rates. Proc. Natl. Acad. Sci. U S A, 109(8):2919-24, 2012.

[24] El Madani H.A.,Tancrède-Bohin, E., Bensussan, A., Colonna, A., Dupuy, A., Bagot, M., Pena, A.M., In vivo multiphoton imaging of human skin: assessment of topical corticosteroid-induced epidermis atrophy and depigmentation. J Biomed Opt., 17(2):026009, 2012.

[25] Kobat, D., Horton, N.G., Xu., C. In vivo two-photon microscopy to 1.6-mm depth in mouse cortex. J Biomed Opt, 16(10):106014, 2011.

[26] Mertz, J., Xu, C., Webb, W.W. Single-molecule detection by two-photon-excited fluorescence. Opt Lett., 20(24):2532, 1995.

[27] Boulesteix, T., Pagès, N., Godeau, G., Sauviat, M.P., Beaurepaire, E., Schanne-Klein, M.C. Micrometer scale ex vivo multiphoton imaging of unstained arterial wall structure. Cytometry A., 69(1):20-6., 2006.

[28] Kleinhans, C., Kafitz., K. W., and Rose, C. R., Multi-photon Intracellular Sodium Imaging Combined with UV-mediated Focal Uncaging of Glutamate in CA1 Pyramidal Neurons. J Vis Exp.; (92): 52038, 2014.

[29] Teng, S.W., Tan, H.Y., Peng, J.L., Lin, H.H., Kim, K.H., Lo, W., Sun, Y., Lin, W.C., Lin, S.J., Jee, S.H., So, P.T., Dong, C.Y. Multiphoton autofluorescence and second-harmonic generation imaging of the ex vivo porcine eye. Invest Ophthalmol Vis Sci., 47(3):1216-24, 2006.

[30] Goodacre, A., Donley, D., Jai, J., Combining Second-Harmonic Generation with Multiphoton Imaging. Photonics.com., 2010.

[31] De Giorgi, V., Massi, D., Sestini, S., Cicchi, R., Pavone, F.S., Lotti, T., Combined non-linear laser imaging (two-photon excitation fluorescence microscopy, fluorescence lifetime imaging, multispectral multiphoton microscopy) in cutaneous tumors: First experiences. J Eur Acad Dermatol Venerol 23:314-316, 2009.

[32] Seidenari, S., Arginelli, F., Dunsby, C., French, P.M, König, K., Magnoni, C., Talbot, C., Ponti, G. Multiphoton laser tomography and fluorescence lifetime imaging of melanoma: morphologic features and quantitative data for sensitive and specific non-invasive diagnostics, PloS One, 8(7):e70682, 2013.

[33] Breunig, H.G., Bückle, R., Kellner-Höfer, M., Weinigel, M., Lademann, J., Sterry, W., König, K. Combined in vivo multiphoton and CARS imaging of healthy and disease-affected human skin. Microsc Res Tech., 75(4):492-8, 2012.

[34] Lee, Y. J. Determination of 3D Molecular Orientation by Concurrent Polarization Analysis of Multiple Raman Modes in Broadband CARS Spectroscopy. Opt. Express 23, 29279 (2015).

[35] Hell, S. W. and Stelzer, E. H. K. Fundamental improvement of resolution with a 4Pi-confocal fluorescence microscope using two-photon excitation. Opt. Commun. 93: 277-282, 1992.

[36] Mertz, J. Molecular photodynamics involved in multi-photon excitation fluorescence microscopy. Eur. Phys. J. D 3, 53-66 (1998).

[37] Strickler, J.H., Webb, W.W., Three-dimensional optical data storage in refractive media by two-photon point excitation. Optics Letters, Vol. 16, Issue 22, pp 1780-1782, 1991.

[38] Grotjohann, T., Testa, I., Leutenegger, M., Bock, H., Urban, N.T., Lavoie-Cardinal, F., Willig, K.I., Eggeling, C., Jakobs, S., Hell, S.W. Diffraction-unlimited all-optical imaging and writing with a photochromic GFP. Nature, 478(7368):204-8, 2011.

[39] Hoover, E.E., Squier, J.A., Advances in multiphoton microscopy technology. Nat. Photonics., 7(2): 93–101, 2013.

[40] A. L. Capodilupo et al., Design and synthesis of fluorenone-based dyes: two-photon excited fluorescent probes for imaging of lysosomes and mitochondria in living cells. J. Mater. Chem. B, 3, 3315-3323, 2015.

[41] Booth, M.J., Hell, S.W., Continuous wave excitation two-photon fluorescence microscopy exemplified with the 647-nm ArKr laser line. Journal of Microscopy, Vol 190, Pt 3, pp 298-304.

[42] Murari, K., Zhang, Y., Li, S., Chen, Y., Li, M-J., Li, X., Compensation-free, all-fiber-optic, two-photon endomicroscopy at 1.55 μm. Opt Lett. 2011 Apr 1; 36(7): 1299–1301.

[43] Taira, K., Hashimoto, T., Yokoyama, H., Two-photon fluorescence imaging with a pulse source based on a 980-nm gain-switched laser diode. Opt Express, 15(5):2454-8, 2007.

[44] Xu, C., Wise, F.W., Recent advances in fibre lasers for nonlinear microscopy. Nature Photon., **7**, 875–882, 2013.

[45] Aviles-Espinosa, R., et al., Compact ultrafast semiconductor disk laser: targeting GFP based nonlinear applications in living organisms. Biomed Opt Express, 2(4): 739–747, 2011.

[46] Voigt, F.F., et al., Multiphoton in vivo imaging with a femtosecond semiconductor disk laser. Biomed Opt Express, 8(7):3213-3231, 2017.

[47] Basov, N., Bogdankevich, O., Grasyuk, A., Semiconductor lasers with radiating mirrors. IEEE Journal of Quantum Electronics, 2, 594, 1966.

[48] Rahim, M., Felder F., Fill, M., and Zogg, H., Optically pumped 5 μm IV-VI VECSEL with Al-heat spreader Opt. Lett. 33, 2008.

[49] Debusmann, R., Dhidah, N., Hoffmann, V., Weixelbaum, L., Brauch, U., Graf, T., Weyers, M., and Kneissl, M., InGaN–GaN disk laser for blue-violet emission wavelengths IEEE Photonics Technol. Lett. 9 652–4, 2010.

[50] Rahim, M., Khiar, A., Felder, F., Fill, M., and Zogg, H., 5 μm vertical external-cavity surface-emitting laser (VECSEL) for spectroscopic applications Appl. Phys. B 100 261–4.

[51] Park S-H and Jeon H., Microchip-type InGaN vertical external-cavity Opt. Rev. 13 20–3, 2006.

[52] Park S-H, Kim J, Jeon H, Sakong T, Lee S-N, Chae S, Park Y, Jeong C-H, Yeom G-Y and Cho Y-H., Roomtemperature GaN vertical-cavity surface-emitting laser operation in an extended cavity scheme Appl. Phys. Lett., 83 2121–3, 2003.

[53] A. Smith , J. E. Hastie , H. D. Foreman , T. Leinonen , M. Guina , and M. D. Dawson, GaN diode-pumping of a red semiconductor disk laser, Electron. Lett . 44 ,1195–1196 (2008).

[54] M. I. Müller , C. Karnutsch , J. Luft , W. Schmid , K. Streubel , N. Linder , S. S. Beyertt , U. Brauch , A. Giesen , and G. H. Döhler , Optically pumped vertical external cavity semiconductor thin-disk laser with CW operation at 660nm, Inst. Phys. Conf. Ser. No 174 , 427–430 (2002).

[55] J. E. Hastie , S. Calvez , M. D. Dawson , T. Leinonen , A. Laakso , J. Lyytikäinen , and M. Pessa , High power CW red VECSEL with linearly polarized TEM 00 output beam, Opt. Express 13 , 77–81 (2005).

[56] S. Calvez , J. E. Hastie , M. Guina , O. Okhotnikov , and M. D. Dawson , Semiconductor disk lasers for the generation of visible and ultraviolet radiation, Laser Photonics Rev . 3 , 407–434 (2009).

[57] P. J. Schlosser , J. E. Hastie , S. Calvez , A. B. Krysa , and M. D. Dawson , InP/AlGaInP quantum dot semiconductor disk lasers for CW TEM00 emission at 716–755 nm, Opt. Express 17 , 21782–21787 (2009).

[58] J. E. Hastie , J. M. Hopkins , S. Calvez , C. W. Jeon , D. Burns , R. Abram , E. Riis , A. I. Ferguson , and M. D. Dawson , 0. 5-W single transverse-mode operation of an 850-nm diode-pumped surface-emitting semiconductor laser, IEEE Photon. Tech. Lett . 15 , 894–896 (2003).

[59] M. A. Holm , D. Burns , P. Cusumano , A. I. Ferguson , and M. D. Dawson , Highpower diode-pumped AlGaAs surface-emitting laser, Appl. Opt . 38 , 5781–5784 (1999).

[60] B. Cocquelin , D. Holleville , G. Lucas-Leclin , I. Sagnes , A. Garnache , M. Myara , and P. Georges , Tunable single-frequency operation of a diode-pumped vertical external-cavity laser at the cesium D2 line, Appl. Phys. B 95 , 315–321 (2009).

[61] S. Lutgen , T. Albrecht , P. Brick , W. Reill , J. Luft , and W. Späth , 8-W high efficiency continuous-wave semiconductor disk laser at 1000nm, Appl. Phys. Lett . 82 , 3620–3622 (2003).

[62] K. S. Kim , J. Yoo , G. Kim , S. Lee , S. Cho , J. Kim , T. Kim , and Y. Park , 920-nm vertical-external-cavity surface-emitting lasers with a slope effi ciency of 58% at room temperature, IEEE Photon. Tech. Lett . 19 , 1655–1657 (2007).

[63] L. Fan , C. Hessenius , M. Fallahi , J. Hader , H. Li , J. V. Moloney , W. Stolz , S. W. Koch , J. T. Murray , and R. Bedford , Highly strained InGaAs/ GaAs multiwatt vertical-external-cavity surface-emitting laser emitting around 1170 nm, Appl. Phys. Lett . 91 , 131114 (2007).

[64] J. M. Hopkins , S. A. Smith , C. W. Jeon , D. Burns , S. Calvez , M. D. Dawson , T. Jouhti , and M. Pessa , A 0.6W CW GaInNAs vertical external-cavity surfaceemitting laser operating at 1.32mm, Electron. Lett . 40 , 30–31 (2004).

[65] S. L. Vetter , J. E. Hastie , V.-M. Korpijarvi , J. Puustinen , M. Guina , O. Okhotnikov , S. Calvez , and M. D. Dawson , Short-wavelength GaInNAs/ GaAs semiconductor disk lasers, Electron. Lett . 44 , 1069–1070 (2008).

[66] V.-M. Korpijärvi , M. Guina , J. Puustinen , P. Tuomisto , J. Rautiainen , A. Härkönen , A. Tukiainen , O. Okhotnikov , and M. Pessa , MBE grown GaInNAsbased multi-Watt disk lasers, J. Cryst. Growth 311, 1868–1871 (2009).

[67] V.-M. Korpijärvi , T. Leinonen , J. Puustinen , A. Härkönen , and M. Guina , 11 W single gain-chip dilute nitride disk laser emitting around 1180 nm, Opt. Express 18 , 25633–25641 (2010).

[68] C. Symonds , I. Sagnes , A. Garnache , S. Hoogland , G. Saint-Girons , A. C. Tropper , and J.-L. Oudar , Continuous-wave operation of monolithically grown 1. 5-mm optically pumped vertical-external-cavity surface-emitting lasers, Appl. Opt .42 , 6678–6681 (2003).

[69] H. Lindberg , M. Strassner , E. Gerster , and A. Larsson , 0.8 W optically pumped vertical external cavity surface emitting laser operating CW at 1550 nm, Electron. Lett . 40 , 601–602
(2004).

[70] H. Lindberg , M. Strassner , E. Gerster , J. Bengtsson , and A. Larsson , Thermal management of optically pumped long-wavelength InP-based semiconductor disk lasers, IEEE J. Sel. Top. Quantum Electron . 11 , 1126–1 (2005).

[71] H. Lindberg , A. Larsson , and M. Strassner , Single-frequency operation of a high-power, long-wavelength semiconductor disk laser, Opt. Lett. 30 , 2260–2262 (2005).

[72] J. M. Hopkins , A. J. Maclean , D. Burns , E. Riis , N. Schulz , M. Rattunde , C. Manz , K. Köhler , and J. Wagner , Tunable, single-frequency, diode-pumped 2.3mm VECSEL, Opt. Express 15 , 8212–8217 (2007).

[73] N. Schulz , J.-M. Hopkins , M. Rattunde , D. Burns , and J. Wagner , High-brightness long-wavelength semiconductor disk lasers, Laser Photon. Rev . 2 , 160–181 (2008).

[74] B. Rösener , M. Rattunde , M. Moser , S. Kaspar , T. Töpper , C. Manz , K. Köhler , and J. Wagner , Continuous-wave room-temperature operation of a 2.8 mm GaSb-based semiconductor disk laser, Opt. Lett . 36 , 319–321 (2011).

[75] Rahim, M., Fill, M., Felder, F., Chappius, D., Corda, M., Zogg, H., Mid-Infrared PbTe vertical external cavity surface emitting laser on Si-substrate with above 1W output power. Appl. Phys. Lett., 95, 241107, 2009.

[76] Kuznetsov, M., Hakimi, F., Sprague, R., Design and characteristics of high-power (>0.5-W CW) diode-pumped vertical-external-cavity surface-emitting semiconductor lasers with circular TEM/sub 00/ beams. IEEE Journal of Selected Topics in Quantum Electronics, Vol. 5, Issue 3, 561-573, 1999.

[77] B. Rudin, V. J. Wittwer, D. J. H. C. Maas, M. Hoffmann, O. D. Sieber, Y. Barbarin, M. Golling,T.Südmeyer,U.Keller, Novel ultrafast semiconductor laser with 6.4 W average output power. Optics Express, vol. 18, pp. 27582-27588, 2010.

[78] J Paajaste, S Suomalainen, R Koskinen, A Härkönen, M Guina, M Pessa, Journal of Crystal Growth 311 (7), 1917-1919, 2009.

[79] H Kahle, R Bek, M Heldmaier, T Schwarzbäck, M Jetter, P Michler, High optical output power in the UVA range of a frequency-doubled, strain-compensated AlGaInP-VECSEL, Applied Physics Express 7 (9), 092705, 2014.

[80] Kantola, E., Leinonen, T., Penttinen, J.P., Korpijärvi, V.M., Guina, M., 615 nm GaInNAs VECSEL with output power above 10 W. Opt Express., 23(16):20280-7, 2015.

[81] Heinen, B., et al., 106 W continuous wave output power from a vertical-external-cavity surface-emitting laser (VECSEL), Electronics Letters 48 (9), 516, 2012.

[82] Quarterman, Adrian H.; Wilcox, Keith G.; Apostolopoulos, Vasilis; Mihoubi, Zakaria; Elsmere, Stephen P.; Farrer, Ian; Ritchie, David A.; Tropper, Anne. A passively mode-locked external-cavity semiconductor laser emitting 60-fs pulses. Nature Photonics, Vol. 3, No. 12, 12.2009, p. 729-731.

[83] P. Klopp, U. Griebner, M. Zorn, and M. Weyers, Pulse repetition rate up to 92 GHz or pulse duration shorter than 110 fs from a mode-locked semiconductor disk laser, Applied Physics Letters 98, 071103-071103 (2011).

[84] Laurain, A., et al., High power sub-200fs pulse generation from a colliding pulse modelocked VECSEL. SPIE Lase 2017.

[85] Tilma, B.W. et al., Recent advances in ultrafast semiconductor disc lasers. Light: Science & Applications 4 (7), e310, 2015.

[86] Hader, J., et al., Predictive Microscopic Modeling of VECSELs. IEEE Journal of Quantum Electronics, Vol.b46, Issue 5, 810-817, 2010.

[87] Koch, S.W., Hader, J., Moloney, J.V., Microscopic VECSEL modeling. SPIE LASE, Proceedings Volume 8966, 2014.Fully microscopic modeling of mode locking in microcavity lasers. Journal of the Optical Society of America B, Vol. 33, Issue 1, pp. 75-80, 2016.

[88] Hoffmann, M., et al., Femtosecond high-power quantum dot vertical external cavity surface emitting laser. Opt. Express, 19(9):8108-16, 2011.

[89] Nakdali, D., et al., High-Power Quantum-Dot Vertical-External-Cavity Surface-Emitting Laser Exceeding 8 W. IEEE Photonics Technology Letters, Vol. 26, issue 15, 1561-1564, 2014.

[90] Albrecht et al., Multi-watt 1.25 μm quantum dot VECSEL. Electronics Letters. Volume 46, Issue 12, p. 856 – 857, 2010.

[91] Fan, Li and Fallahi, M., Tunable high – power high – brightness lineary polarized vertical external cavity surface-emitting lasers. Appl. Phys. Lett., 88, 021105, 2006.

[92] Paajaste, J., et al., Power scalable 2.5 μm (AlGaIn) (AsSb) semiconductor disk laser grown by molecular beam epitaxy. Journal of Crystal Growth, Vol. 323, No. 1, p. 454-456, 2011.

[93] U. Keller et al., Solid-state low-loss intracavity saturable absorber for Nd:YLF lasers: an antiresonant semiconductor Fabry-Perot saturable absorber, Optics Lett., vol. 17, pp. 505-507, 1992.

[94] U.Keller and A.C.Tropper, Passively modelocked surface-emitting semiconductor lasers. Physics Reports, vol. 429, Nr. 2, pp. 67-120, 2006.

[95] Rautiainen, J. et al., Actively Mode-Locked Semiconductor Disk Laser Using Vertical Cavity Modulator. Conference: Conference: The European Conference on Lasers and Electro-Optics, CLEO, 2013, DOI: 10.1109/CLEOE-IQEC.2013.6800747.

[96] Hoogland et al., Passively mode-locked diode-pumped surface-emitting semiconductor laser. IEEE Photonics Technology Letters, Vol. 12, Issue 9, 1135-1137, 2000.

[97] Wittwer, V. J., et al., Timing jitter characterization of a quantum dot SESAM modelocked VECSEL. SPIE LASE 2011, Vol. 7919.

[98] Seger, K., et al., Carbon nanotube mode-locked optically-pumped semiconductor disk laser. Opt Express. ,21(15):17806-13, 2013.

[99] Zaugg, C.A., et al., Passively modelocked VECSEL using a single-layer graphene saturable absorber mirror. Lasers and Electro-Optics Europe (CLEO EUROPE/IQEC), 2013.

[100] Laurain et al., Colliding pulse mode locking of vertical-external-cavity surface-emitting laser. Optica, Vol. 3, Issue 7, pp. 781-784, 2016.

[101] Kornaszewski, L. et al., SESAM-free mode-locked semiconductor disk laser. Laser & Photonics Review, Volume6, Issue6, L20–L23. 2012.

[102] Gaafar, M., Self-mode-locked quantum-dot vertical-external-cavity surface-emitting laser. Opt. Lett. ,39(15):4623-6, 2014.

[103] D. J. H. C. Maas, A.-R. Bellancourt, B. Rudin, M. Golling, H. J. Unold, T. Südmeyer, U. Keller, Vertical integration of ultrafast semiconductor lasers. Appl. Phys. B, vol 88, pp 493, 2007.

[104] B. Rudin, V. J. Wittwer, D. J. H. C. Maas, M. Hoffmann, O. D. Sieber, Y. Barbarin, M. Golling, T.Südmeyer, U.Keller, Optics Express, vol. 18, pp. 27582-27588, 2010.

[105] V. J. Wittwer, M. Mangold, M. Hoffmann, O. D. Sieber, M. Golling, T. Südmeyer, U. Keller High-power integrated ultrafast semiconductor disk laser: multi-watt 10-GHz pulse generation. Electronics Lett., vol. 48, No. 18, pp. 1144, 2012.

[106] Mangold, M., et al., Femtosecond pulses from a modelocked integrated external-cavity surface emitting laser (MIXSEL).Opt Express, 21;21(21):24904-11, 2013.

[107] Mario Mangold, Christian A Zaugg, Sandro M Link, Matthias Golling, Bauke W Tilma, Ursula Keller, Pulse repetition rate scaling from 5 to 100 GHz with a high-power semiconductor disk laser. Vol. 22, Issue 5, 6099-6107, 2014.

[108] Link, S.M., Maas, D.J.H.C., Waldburger D., Keller, U., Dual-comb spectroscopy of water vapor with a free-running semiconductor disk laser. Science ,356(6343):1164-1168, 2017.

[109] Hastie, J.E. et al., Microchip vertical external cavity surface emitting lasers. Electron. Lett., 39,1324–1326. 2003.

[110] Hopkins, J.M. et al., 0.6 W CW GaInNAs vertical external-cavity surface emitting laser operating at 1.32 /spl mu/m. Electronics Letters, Vol. 40, Issue 1, 30-31, 2004.

[111] Perez, J. P., et al. Technologies for thermal management of mid-IR Sb-based surface emitting lasers. Semiconductor Science and Technology 25.4 (2010): 045021.

[112] Yang, Z., Albrecht, A. R., Cederberg, J. G., and Sheik-Bahae, M., 80 nm tunable DBR-free semiconductor disk laser, Appl. Phys. Lett., 2016, 109, (022101), pp. 1-4.

[113] Kahle, H., Mateo, C.M.N., Brauch, U., Tatar-Mathes, P., Bek, R., Jetter, M., Graf, T., and Michler, P., 'Semiconductor membrane external-cavity surface-emitting laser (MECSEL)', Optica, 2016, **3**, (12), pp. 1506-1512.

[114] V. Iakovlev, J. Walczak, M. Gębski, A. K. Sokół, M. Wasiak, P. Gallo, A. Sirbu, R. P. Sarzała, M. Dems, T. Czyszanowski, and E. Kapon, Doublediamond high-contrast-gratings vertical external cavity surface emitting laser, J. Phys. D 47, 065104 (2014).

[115] K.G. Wilcox, F. Rutz, R. Wilk, H.D. Foreman, J.S. Roberts, J. Sigmund, H. L. Hartnagel, M. Koch and A.C. Tropper, Terahertz imaging system based on LT-GaAsSb antenna driven by all-semiconductor femtosecond source, Electronics Letters 42, 1159-1160 (2006).

[116] Rey, J.M. et al., Broadly tunable mid-infrared VECSEL for multiple components hydrocarbon gas sensing. Applied Physics B., Vol. 117, Issue 3, pp 935-939, 2014.

[117] Head, C.R. et. al., Supercontinuum Generation with GHz Repetition Rate Femtosecond-Pulse Fiber-Amplified VECSELs. IEEE Photon. Tech. Lett., 2013.

[118] Hempler et al., Semiconductor disk laser pumped Cr^{2+}:ZnSe lasers. Vol. 17, issue 20, 18136, 2009.

[119] Quarterman, A.H., Wilcox, K.G., Design of a solar-pumped semiconductor laser. Optica, Vol. 2, issue 1, pp. 55-61, 2015.

[120] Liu TM, Chu SW, Sun CK, Lin BL, Cheng PC, Johnson I. Multiphoton confocal microscopy using a femtosecond Cr:forsterite laser. Scanning, 23(4):249-54, 2001.

[121] Boyd, R.W. Nonlinear Optics, 2003.

[122] Koester HJ1, Baur D, Uhl R, Hell SW. Ca2+ fluorescence imaging with pico- and femtosecond two-photon excitation: signal and photodamage. Biophys J. 77(4):2226-36, 1999.

[123] Resan, B., Aviles-Espinosa, R., Kurmulis, S., Licea-Rodriguez, J., Brunner, F., Rohrbacher, A., Artigas, D., Loza-Alvarez, P., and Weingarten, K.J., Two-photon fluorescence imaging with 30 fs laser system tunable around 1 micron. Optics Express, Vol. 22, Issue 13, pp. 16456-16461, 2014.

[124] So, P. T. C. et al., Two-Photon Excitation Fluorescence Microscopy. Annu. Rev. Biomed. Eng., 02 (399-429), 2000.

[125] König, K.Multiphoton microscopy in life sciences. J Microsc. (Pt 2):83-104. 2000.

[126] Robertson, T.A. et al., Fluorescein Derivatives in Intravital Fluorescence Imaging. Cells, 2 (3), 591-606, 2013.

[127] Becker, W. et al., Fluorescence Lifetime Imaging by Time-Correlated Single-Photon Counting. Microscopy Research and Technique 63:58 – 66 (2004).

[128] Turtaev, S., et al. Multimode fibres for micro-endoscopy. Optofluidics, Microfluidics and Nanofluidics. 2 (1), 31-35, 2015.

[129] Tomáš Čižmár and Kishan Dholakia. Exploiting multimode waveguides for pure fibre-based imaging. Nature Communications, volume 3, 2012.

[130] Morris, O. Cryogenic operation and room temperature application of an optically-pumped surface-emitting semiconductor laser, 2014.

[131] Sze, S.M., Lee, M-K., Semiconductor Devices: Physics and Technology, 2012.

[132] Ihn, T. Semiconductor Nanostructures. 2010.

[133] R. Tsu and L. Esaki, Tunneling in a finite superlattice. Applied Physics Letters *22*: 562, 1973.

[134] Okhotnokov, O. Semiconductor Disk Lasers: Physics and Technology. 2010.

[135] Calvez, S., et al., 1.3 mm GalnNAs optically pumped vertical cavity semiconductor optical amplifier. Electron. Lett., 39, 100–102, 2003.

[136] Quarterman, A.H. Femtosecond pulse generation in surface-emitting semiconductor lasers, 2009.

[137] Hessenius, C. et al., High-power tunable two-wavelength generation in a two chip co-linear T-cavity vertical external-cavity surface-emitting laser. Applied Physics Letters, 101 (12), 2012.

[138] Guina, M. et al., Semiconductor Disk Lasers: Recent Advances in Generation of Yellow-Orange and Mid-IR Radiation. Advances in Optical Technologies, Vol. 2012, (2012).

[139] Zhang, F. et al., A 23-watt single-frequency vertical-external-cavity surface-emitting laser Optics Express Vol. 22, Issue 11, pp. 12817-12822 (2014).

[140] Uenishi, Y., et al., Microstructure characterization of AlGaAs fabricated by AlGaAs/GaAs micromachining. IEEE Trans. Electron Devices 41,1778–1783, 1994.

[141] Haus, H. A. Theory of mode locking with a fast saturable absorber. Journal of Applied Physics, Vol. 46, No.7, 1975.

[142] D. J. H. C. Maas, A.-R. Bellancourt, B. Rudin, M. Golling, H. J. Unold, T. Südmeyer, U. Keller, Vertical integration of ultrafast semiconductor lasers Appl. Phys. B, vol 88, pp 493, 2007.

[143] D. E. Spence, P. N. Kean, W. Sibbett, 60-fsec pulse generation from a self-mode-locked Ti:sapphire laser, Opt. Lett. 16 (1), 42 (1991).

[144] D. H. Sutter et al., Semiconductor saturable-absorber mirror-assisted Kerr lens modelocked Ti:sapphire laser producing pulses in the two-cycle regime, Opt. Lett. 24 (9), 631 (1999).

[145] Wilcox, K.G. et al., Ultrafast Optical Stark mode-locked semiconductor Laser. Opt Lett., 33(23):2797-9, 2008.

[146] G. J. Daniell, Z. Mihoubi, K. G. Wilcox, and A. C. Tropper, Numerical model of the optical Stark effect as a mode-locking mechanism for femtosecond vertical-external-cavity surface-emitting semiconductor lasers, in Conference on Lasers and Electro-Optics/Quantum Electronics and Laser Science Conference and Photonics Applications Systems Technologies. OSA Technical Digest (CD)(Optical Society of America, 2008), paper CThF3.

[147] R. Paschotta et al., Soliton-like pulse shaping mechanism in passively mode-locked surface-emitting semiconductor lasers, Appl. Phys. B 75, 445 (2002).

[148] Fork, R.L., Greene, B.I., Shank, C.V., Generation of opticl pulses shorter than 0.1 psec by colliding pulse mode locking. Appl. Phys. Lett., 38, 671, 1998.

[149] Yablonovitch, E., et al. Extreme selectivity in the lift-off of epitaxial GaAs films. Appl. Phys. Lett. 51, 2222 (1988).

[150] Maeda, J. et al. High-Rate GaAs Epitaxial Lift-Off Technique for Optoelectronic Integrated Circuits. Japanese Journal of Applied Physics, Volume 36, Part 1, Number 3B.

[151] Baranov A., Tournié E. Semiconductor lasers: Fundamentals and applications. 2013.